



Development of optical trapping techniques for *in vivo* investigations

Andrew C. Richardson



Submitted in fulfilment of the
requirements for the degree of
Doctor of Philosophy

Supervisor: Lene Oddershede

Optical Tweezers Group
The Niels Bohr Institute
University of Copenhagen
Denmark

31st of December 2008

I hereby declare that the content of this thesis is entirely my own work and contains no material which has been accepted for the award of any other degree or diploma at any University. The thesis comprises a discussion and summary of the work I carried out between September 2005 and September 2008 at the Niels Bohr institute as part of my PhD studies. To the best of my knowledge and belief, this dissertation contains no material previously published or written by another person, except where due reference has been made.

—

The image on the front cover is of a 'Golden apple' which is one of three such apples that levitate from the fountain at Gammeltorv in the centre of Copenhagen, on occasions such as the Queens birthday and Denmark's constitutional day. Although the golden apples are not confined by optical forces like those used to trap gold nano-particles, it is a jovial and light hearted comparison to the microscopic equivalent.

Contents

Preface	ix
List of abbreviations	xiii
1 Optical Trapping	1
1.1 A brief history of optical trapping	1
1.1.1 Optical tweezing	2
1.2 Forces in optical trapping	3
1.2.1 Mie regime	3
1.2.2 Rayleigh regime	6
1.2.3 Absorption	7
1.2.4 Intermediate regime	8
1.3 Calibration	8
1.3.1 Optical tweezers setup	9
1.3.2 Calibration by power spectral analysis	10
1.3.3 Calibration by viscous drag force	12
1.3.4 Comparison of power spectral analysis and drag force calibration . .	12
1.4 Summary	13
2 An investigation of optical trapping potential by the suppression of spherical aberrations	15
2.1 Overview	15
2.1.1 Previous experimental work	16
2.1.2 Theoretical predictions	19
2.2 Characterising the optical trapping potential	20
2.2.1 Experimental setup	20
2.2.2 Compensation for spherical aberration	22
2.2.3 Experimental procedure	23
2.2.4 Image optimisation and image analysis using LABview	27
2.2.5 Pixel calibration	28

2.3	Results and discussion	30
2.3.1	Increased axial confinement	30
2.3.2	Force displacement profile	32
2.4	Size dependency	35
2.4.1	Role of the side lobes	35
2.5	Summary	36
3	Micro-injection of <i>S. pombe</i> yeast cells	39
3.1	Background	39
3.2	Overview	40
3.3	Why use <i>S. pombe</i>	41
3.4	Micro-injection of <i>S. pombe</i>	42
3.4.1	Preparation of yeast	42
3.4.2	Selection of a probe	44
3.4.3	Micro-injection	45
3.4.4	Regeneration	49
3.5	Alternative methods of probe transfer to <i>S.pombe</i>	50
3.5.1	Simple lipid assisted micro-injection (SLAM)	50
3.5.2	Vesicle fusion	50
3.6	Summary	52
4	Calibration of optical tweezers in complex viscoelastic media	53
4.1	Overview	53
4.2	Brief theoretical introduction	54
4.2.1	The Fluctuation dissipation theorem (FDT) calibration method	54
4.2.2	Selecting the appropriate amplitude and frequency of stage driving	56
4.3	Experimental procedure	57
4.3.1	Passive measurements	59
4.3.2	Active measurements	60
4.3.3	Determining the positional calibration factor or beta value	61
4.3.4	Pixel calibration	62
4.3.5	Calibration of the channel delay from the input/output (data acquisition) card	62
4.4	Data analysis	63
4.5	Results and discussion	63
4.5.1	Calibration in Water	63
4.5.2	Calibration in Entangled F-actin	65
4.6	Summary	67

5	Confocal-tweezers	69
5.1	Overview	69
5.2	Confocal microscopy	70
5.3	Previous research in confocal tweezing	71
5.4	Integration of the tweezers	73
5.4.1	2D scanning	73
5.4.2	Coupling the trapping laser into the optical path of the SP5 confocal system	74
5.5	Experimental method	75
5.6	Result and discussion	76
5.7	Future work	78
5.7.1	3D scanning	78
5.8	Summary	79
6	Three dimensional optical control of individual quantum dots	81
6.1	Overview	81
6.2	What are quantum dots?	82
6.3	Early experiments	84
6.3.1	Trapping quantum dots	84
6.3.2	Visualising quantum dots	85
6.4	Improvements to the experimental setup and procedure	87
6.4.1	The EMCCD alternative	87
6.4.2	Buffer optimisation	89
6.4.3	Reducing the axial movement of the quantum dot by compensating for spherical aberrations	89
6.5	Experimental procedure	89
6.5.1	Pressing a trapped quantum dot onto the lower glass surface of the sample, under high salt concentrations	89
6.5.2	Using Streptavidin coated quantum dots for specific binding to a biotin coated glass surface	91
6.6	Results	91
6.6.1	Trapping of individual quantum dots; a statistical argument	91
6.6.2	Trapping of individual quantum dots; visual verification by blinking	92
6.6.3	Optical trap stiffness, κ , of a trapped QD	93
6.6.4	The inferred properties of a quantum dot	95
6.7	Future experiments	99
6.8	Summary	100
	Conclusions & outlook	101

Bibliography

101

List of Publications

- A.C. Richardson, S.N.S. Reihani, and L.B. Oddershede. "Combining confocal microscopy with precise force-scope optical tweezers". *Proceedings of SPIE*, **6326**, pp 28.1-28.10, (2006).
- A.C. Richardson, S.N.S. Reihani, and L.B. Oddershede. "Extending the lateral trapping force of optical tweezers". *Proceedings of SPIE*, **6644**, pp 20.1-20.9, (2007).
- M. Fischer, A.C. Richardson, S.N.S. Reihani, L.B. Oddershede, and K. Berg-Sørensen. "Validation of FDT calibration method in complex media". *Proceeding of SPIE*, **7038**, pp 22.1-22.12, (2008).
- A.C. Richardson, S.N.S. Reihani, and L.B. Oddershede. "Non-harmonic potential of a single beam optical trap". *Optics Express*, **16**, pp 15709-15717, (2008).
- L. Jauffred, A.C. Richardson, and L.B. Oddershede. "Three-dimensional optical control of individual quantum dots". *Nano Letters*, **8**, pp 3376-3380, (2008).
- A.C. Richardson, M. Fischer, S.N.S. Reihani, K. Berg-Sørensen, and L.B. Oddershede. "How to calibrate optical tweezers in viscoelastic media". (*Submitted*).
- A.C. Richardson, P.M. Hansen, and L.B. Oddershede. "Micro-injection of *S.pombe* yeast cells". (*in progress*).

Preface

From as early as Egyptian times, mankind has endeavoured to understand the things around it; the changing of the seasons and the phases of the moon are to name but a few of the early wanderings of our curious ancestors minds. Physics has played a dominant role in describing the physical laws and mechanisms by which our universe is governed. However, understanding mankind and the processes ongoing within our own bodies had, until relatively recently, been left to biologists.

The evolution of the field of biophysics has been rapid in recent years, largely because there was a need for it. Biophysicists approach biological problems from a very different perspective to that of biologists and this change in thinking has led to new insights into the mechanisms and processes occurring within cells [1]. There is no shortage of areas where long standing questions of biological function exist; cell rheology, cell motility, and cell mechanics are just a few of the areas where numerous questions remain unanswered, making biophysics an exciting area of research to work in.

The interdisciplinary nature of biophysics brings together the experimental techniques of two quite different disciplines albeit often bound together by the same common tool, the microscope. Optical tweezers are one of the tools used to explore this new cellular environment and can be incorporated into a microscope with relative ease. Optical tweezers are a powerful tool with which to investigate single molecule interactions; the motion of molecular motors, the interaction of proteins and the dynamics of DNA are all areas where optical tweezers have made a significant contribution towards understanding how these biologically relevant molecules function.

An interesting topic for biologists is cell mechanics. The polymerisation and de-polymerisation of microtubules, as well as the role of actin in cell motility, have largely been investigated *in vitro*. However, it is widely hypothesised that there will be, in some cases, considerable differences between the function of molecules *in vivo* when compared to their function *in vitro*, e.g. the polymerisation of microtubules *in vitro* is thought to be less efficient than the *in vivo* case where microtubule associated proteins are present [2]. Furthermore, it is believed that the mechanics of the cell are influenced by diseases such as cancer and it would be interesting to quantitatively observe the significance of this *in vivo*.

Motivation

The motivation for this thesis was to introduce small nano-sized colloids into yeast cells of type *Schizosaccharomyces pombe*, to act as handles for the optical tweezers, and then to use these colloids to manipulate organelles within the cell and to quantitatively monitor ongoing intracellular processes *in vivo*. The goal was to investigate the nano-mechanics of cell division using optical tweezers and confocal microscopy. However, on route to this goal, a number of other interesting and related projects evolved which were subsequently pursued. For example, calibrating optical tweezers in viscoelastic media, trapping quantum dots and exploring the lateral optical trapping potential.

Some of the forces involved in cell division are quite large with respect to the measurement range of optical tweezers ($> 100 pN$). It is possible to increase the measurable force range by increasing the laser power but this has an adverse heating effect. Thus, by quantifying the extent of the linear region of an optical trap and investigating the trapping behaviour beyond, it was hypothesised that one could take advantage of the more extreme regions of the trapping potential to apply larger forces without increasing laser power. This was the basic idea behind the study of the optical trapping potential in Chapter 2.

Investigating the mechanics of cell division requires that a probe of a known size and composition be trapped inside the cytoplasm without the probe itself causing any disruption to the intracellular network. One such probe would be a gold nano-particle. Chapter 3, therefore, deals with the development of a micro-injection technique and other techniques for the insertion of such probes into the biological system of interest, *S. pombe* yeast cells.

In order to investigate the mechanics of cell division, one must be able to accurately and reliably quantify *in vivo* forces in the cytoplasm. Existing calibration techniques are based upon trapping in purely viscous media and are not sufficient for calibration in the complex viscoelastic environment of the cytoplasm. Therefore, one of the projects relating to the main goal of investigating cell mechanics was to experimentally test a method proposed for *in situ* calibration within the cytoplasm [3]. The experiments made to verify the authenticity of the proposed method are the subject of Chapter 4.

Another important step towards making experiments that would harvest information about intracellular processes was to integrate optical tweezers with confocal microscopy and thereby, allow confocal images to be simultaneously obtained together with quantitative force data. This would permit, for example, determination of the *in vivo* persistence length of a microtubule. The integration of optical tweezers with confocal microscopy is discussed in Chapter 5.

As well as developing ones understanding of cell division by making *in vivo* force measurements, extensive information can be gathered about a biological system by confocal microscopy and novel labelling of chromosomes etc. Quantum dots are a revolutionary method of labelling and tracking within a cell because they do not suffer from the same

structural changes that cause fluorophores to bleach under extended periods of illumination by an excitation source. Chapter 6 deals with the novel idea of trapping quantum dots so that quantitative force measurements and visualisation of organelles, or single particle tracking to investigate diffusive processes, could be achieved with the same probe particles.

Thesis outline

The thesis is divided into 6 chapters.

Chapter 1 introduces optical tweezers and discusses calibration in some detail.

Chapter 2 reveals the extent of the linear region of an optical trap and discusses the validity of assuming a single harmonic potential in biophysical measurements such as in the pulling of DNA.

Chapter 3 considers the insertion of nano-handles into *S. pombe* for the purpose of investigating cell rheology. The two main methods considered for insertion are micro-injection and vesicle fusion.

Chapter 4 builds on the previous chapter and handles the issue of calibration in a complex viscoelastic environment such as the cytosol, in which the properties are largely unknown and vary from cell to cell.

Chapter 5 deals with simultaneously making quantitative force measurements with optical tweezers while visualising the intercellular components of the cell by confocal microscopy.

Chapter 6 discusses trapping individual quantum dots and the opportunities this brings for extensive new research when used in connection with the findings of chapter 5 (confocal-tweezers).

Acknowledgements

There are several people whose contributions I would like to acknowledge, a few of which I could never have made it this far without. Firstly, thanks to my supervisor Lene Oddershede for her guidance and continuous support both day to day and through our regular progress meetings. By no means less influential, I would like to acknowledge the contribution of my temporary supervisor and close friend Nader Reihani. He was my supervisor during Lene's maternity leave and has been an excellent source of advice and encouragement ever since, despite having started his own group in Iran.

I have had the pleasure of working closely with Poul Martin Hansen and Liselotte Jauffred Pedersen on the micro-injection of yeast and the optical trapping of quantum dots, respectively. Thanks go to them for their efforts and general enthusiasm in the lab. Thanks

CONTENTS

also go to Kirstine Berg-Sørensen and Mario Fischer for their significant contributions in the collaborative project to experimentally validate their newly proposed calibration method.

In general, I would like to thank all members of the optical tweezers group and the biocomplexity group as a whole, they made the institute a fun and relaxed place in which to carry out research. I am also indebted to the Marie Curie foundation early stage training network for supporting me financially during my research and also to Dejan Trpceviski who provided me with a Latex thesis template and answered all my ridiculous questions. Last but not least, thanks go to my family and friends who constantly supported me and asked how the dissertation was coming along - it was wonderful motivation when I needed it!

List of abbreviations

AFM - Atomic force microscopy
AOM - Acousto-optic modulation
AOBS - Acousto-optic beam splitter
AOTF - Acousto-optic tuneable filter
APD - Avalanche photodiode
BSA - Bovine serum albumin
CCD - Charge coupled device
DNA - Deoxyribonucleic acid
EMCCD - Electron multiplying charge coupled device
FDT - Fluctuation dissipation theorem
GFP - Green fluorescent protein
GUVs - Giant unilamellar vesicles
ITO - Indium tin oxide
MEMS - Micro electromechanical systems
MTs - Microtubules
NA - Numerical aperture
NBI - Niels Bohr Institute
OIM - Optimised immersion medium
PEG - Polyethylene glycol
PSA - Power spectral analysis
PSD - Power spectral density
PSF - Point spread function
QDs - Quantum dots
QPD - Quadrant photodiode
S. pombe - *Schizosaccharomyces pombe*
SIM - Standard immersion medium
SLAM - Simple lipid assisted micro-injection
SNR - Signal to noise ratio
SPT - Single particle tracking
SQDT - Single quantum dot tracking

CONTENTS

- TEM* - Transverse electromagnetic
- TEM - Transmission electron microscopy
- TFE - Trifluoroethanol
- UV - Ultraviolet
- YPD - Yeast peptide dextrose

CHAPTER 1

Optical Trapping

This chapter introduces the experimental technique of optical trapping. The research described in the following chapters either employed optical tweezers or was in some way strongly connected to the use of optical tweezers. For example, the micro-injection of *S. pombe* yeast cells with *nano-handles* for future optical tweezers experiments. Therefore, after an introduction to the history of optical trapping and trapping theory, this chapter makes a detailed explanation of the calibration procedure including position detection of a trapped particle and the subsequent force measurement.

1.1 A brief history of optical trapping

There are many ways to argue that light carries momentum even though the mass of a photon is zero; at the start of the seventeenth century Johannes Kepler observed that comet tails always pointed away from the sun because of the effect of *solar breeze*, and in the early twentieth century Arthur Compton showed that momentum could be imparted from x rays to an electron by observing both a shift in the photon wavelength, (*Compton scattering*), as well as the recoil of the impacted electron. However, the most striking modern day demonstration that light does, in deed, carry momentum came from the observations of Arthur Ashkin in the early seventies [4]. By focussing the Gaussian output from an Argon ion laser (514 nm) into a sample of latex spheres suspended in water, Ashkin discovered that the momentum carried by such a light beam could significantly displace these spheres in the beam propagation direction and that the spheres were also drawn toward the focus of the laser in the lateral plane, prior to being pushed forward in the beam propagation direction.

Figures 1.1 and 1.2 reveal the experimental blueprints of Ashkin's first ever demonstration of optical trapping. A discussion of the forces involved and their origin follows in section 1.2. However, it is important to stress that the forces applicable by light are extremely small, in the range of a few tens of femto Newtons (fN) to hundreds of pico

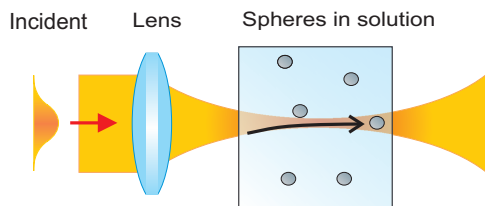


Figure 1.1: A representation of Ashkin's classic experiment where beads are attracted toward the beam axis in the direction orthogonal to beam propagation (momentum transfer) and are pushed away from the focus in the propagation direction (*radiation pressure*). The spheres were only stably trapped in the lateral direction but by use of the rightmost boundary of the sample to oppose further movement by *radiation pressure* they could also be confined in the axial direction. Figure courtesy of Dejan Trpceviski.

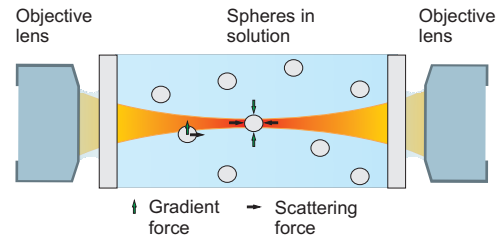


Figure 1.2: The sketch shows how stable optical trapping could be achieved in all three dimensions; using two counter propagating beams to balance the effects of *radiation pressure* from both beams, the point of equilibrium can be arbitrarily chosen for any axial position in the sample by simply increasing or decreasing the powers of the opposing beams with respect to one another.

Newtons (pN), such that in everyday life we do not observe that light is able to displace macroscopic objects. Albeit, for the considered environment in which latex spheres are suspended in water, the tiny forces applicable by momentum transfer of a focussed laser beam become relevant and can overcome the competing random thermal noise (*Brownian Motion*), thereby confining the particle.

1.1.1 Optical tweezing

In 1986, Ashkin and coworkers reported an important development in optical trapping by confining dielectric particles in a new and exciting way [5]. They demonstrated for the first time that particles could be trapped by a single Gaussian laser beam in the beam propagation direction by means of an *axial gradient force*, rather than by balancing the *radiation pressure* of the trapping beam with some external force. For example, without using the beads gravitational force [6] or the *radiation pressure* from a second opposing laser beam.

This single beam trapping geometry became commonly known as 'optical tweezers' because one can simply grab and manipulate microscopic objects with high precision, rather like a pair of regular tweezers can on the macroscopic scale. However, optical tweezers have a significant advantage over regular tweezers in that they provide a non-contact and non-invasive way of manipulating cells and bio-molecules, provided that the correct wavelength of light is chosen, which is highly desirable when trying to avoid contamination of samples during their processing and handling. The effects of optical manipulation on biological

samples are discussed in more detail in section 1.2.3.

Furthermore, tweezers have the additional advantage of an altogether simpler trapping geometry, making it significantly easier to incorporate optical trapping into a standard inverted microscope and with a further benefit that just one objective lens can be used to both trap and image within the sample.

1.2 Forces in optical trapping

There are a couple of methods of explaining why one can trap *microscopic objects* using highly focussed laser light depending upon whether one chooses to consider light as *a ray of photons* or as an *electromagnetic wave*. The term *microscopic objects* encompasses a large variety of particles of different shapes, sizes and compositions and is purposefully used here, instead of the term dielectric spheres, in order to emphasise that almost anything can be trapped, given the correct trapping conditions¹. However, dielectric spheres are the most commonly trapped objects and are frequently used as *handles* with which to manipulate molecules that cannot be directly trapped, e.g. motor proteins. Furthermore, the theory of trapping is most developed for spherical particles and as such, only they are considered in this section.

1.2.1 Mie regime

The simpler of the two methods is to consider light in the classical form of a ray and then to use Snell's law of refraction together with conservation of momentum to explain why a particle is maintained at the beam's focus. This method is called the ray optics approach and is only valid when the diameter of the trapped particle is much larger than the trapping wavelength, ($d \gg \lambda$), known as the Mie regime².

For a laser beam with a *Gaussian intensity profile*, the centre of the beam represents the point of highest intensity. Intensity rapidly decreases as one moves towards the periphery of the focussed spot, in all three dimensions. Optical tweezing relies on an intensity gradient to achieve stable trapping and a Gaussian intensity profile meets this requirement. For the ray optics approach, the most intense part of the beam can be thought of as carrying the most photons and thus is capable of imparting the largest momentum transfer.

The basic principle is that a ray of light impinging on a dielectric sphere is bent because of refraction. Its momentum is, therefore, modified by its passage through the sphere and because light carries momentum, an equal and opposite change in momentum must apply to the sphere. This is better demonstrated visually by considering Figure 1.3 in which Snell's

¹Conditions such as the wavelength of light and the beam profile can drastically change the *trapability* of an object. This is discussed later in section 1.2.2.

²It is generally accepted that spheres with diameters of around 5 times the wavelength of the trapping light can be considered as in the Mie regime.

Chapter 1: Optical Trapping

law of refraction and momentum conservation are used to explain optical confinement of a particle in a Gaussian beam, for the simplified case where the effects of *radiation pressure* and reflection are neglected. A more complicated version of the ray optics approach that does consider reflection and absorption has been presented [7] but even it neglects further complications such as spherical aberrations.

Figure 1.3 depicts a dielectric sphere with radius d and refractive index n_o , suspended in a medium of lower index of refraction n_s .

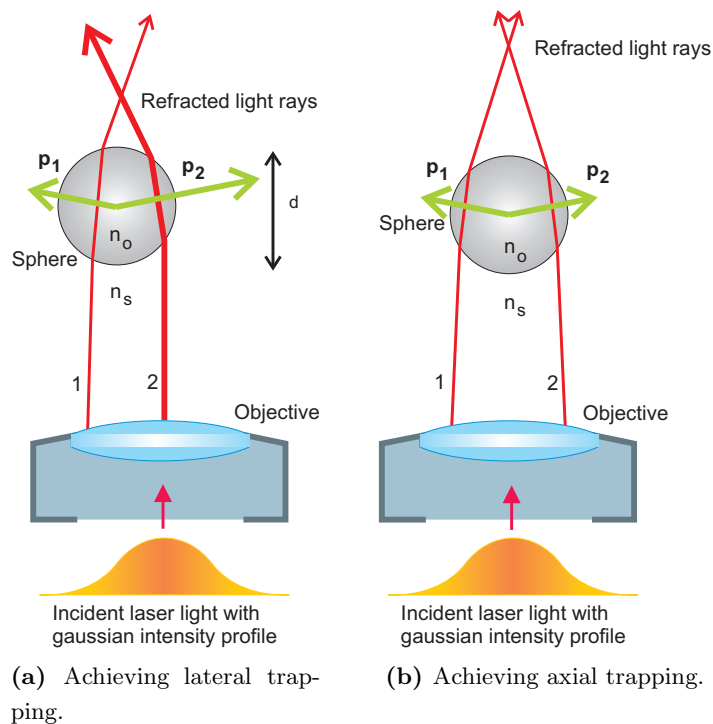


Figure 1.3: The red lines indicate the light paths for two independent rays where line thickness is proportional to the intensity of the light ray. Green arrows show the corresponding momentums $\mathbf{p}_1, \mathbf{p}_2$ that are transferred to the sphere and have lengths proportional to the magnitude of the momentum. Figure borrowed from the Masters thesis of Dejan Trpcevski entitled 'Optical stretching of DNA as a diagnostic tool in nanotoxicology', NBI 2006.

Consider the paths of the two light rays in Figure 1.3a. The first ray (1) is from the periphery of the Gaussian and carries less momentum than ray (2) but is nonetheless refracted by the sphere and imparts some momentum, \mathbf{p}_1 , to the sphere. The second ray (2) originates from the centre of the Gaussian and possesses a considerably larger momentum which is also transferred to the sphere upon refraction, \mathbf{p}_2 . The net momentum ($\mathbf{p}_1 + \mathbf{p}_2$) is thus towards the centre of the beam where the beam is most intense. A light ray will always bend towards the normal when travelling from a low index medium into a high index medium and conversely will bend away from the normal when exiting from a high index

medium into a medium of lower refractive index, according to Snell's law. Therefore, for a beam with a Gaussian intensity profile, the net change in momentum of the refracted light rays is always in the direction away from the most intense region, resulting in a net momentum transfer to the sphere that is always in the direction of the focus. This restoring force is commonly known as the *gradient force*, the reason for which becomes apparent in section 1.2.2.

The opposite is true of the reverse situation, where a sphere of low refractive index is surrounded by a higher index medium. The sphere will be repelled rather than attracted to areas of high intensity since the refracted rays will always point in the direction of highest intensity, transferring momentum to the sphere which pushes it away from the focus. i.e. there exists a *negative gradient force* for such spheres. There are anyhow other methods to trap low index spheres which use intensity profiles with zero intensity at the centre. i.e. *Laguerre Gaussian* beams [8].

In the case of axial trapping, Figure 1.3b shows the paths of two rays, with equal intensities, impinging on a sphere located slightly below the focal point. Again the light rays are refracted by the sphere and a net momentum, $\mathbf{p}_1 + \mathbf{p}_2$, is transferred to the sphere that pushes it towards the point of highest intensity. i.e. the motion is directed towards the focus in the axial direction. A sphere positioned an equivalent distance above the focus will experience the same attractive force as that below the focus, neglecting the destabilising effect of *radiation pressure*. *Radiation pressure* is the general term used to describe optical forces that oppose trapping. i.e. the combination of reflection, absorption and scatter. The effect of the *scattering force* is always to push the bead in the direction of beam propagation. Hence, it aides the bead into the trap when the bead is situated beneath the focus but more importantly, it hinders stable trapping at and beyond the focus. In reality, the bead's equilibrium position is axially shifted slightly beyond the focus because of the *scattering force*; the exact position of the bead depends highly on bead diameter because the scattering force is diameter dependent. The mathematical relation for calculating the *scattering force* is given in section 1.2.2.

The ray optics approach is a completely valid method of giving qualitative information on the optical trapping of beads in the Mie regime. However, as useful a point of reference as ray optics calculations are, physical calibration of the trap is still essential and neither ray optics nor the dipole method, discussed in section 1.2.2, are competent enough to replace *in situ* calibration.

1.2.2 Rayleigh regime

Rayleigh particles are defined as spheres with diameters significantly smaller than the wavelength of light used to trap them³, ($d \ll \lambda$). While light can be conveniently formulated as a ray of photons when considering Mie particles, it is much more appropriate to interpret light as an electromagnetic wave when working with Rayleigh particles.

If a Rayleigh particle is present in an inhomogeneous electromagnetic field, the difference in electric field across its diameter leads to a separation of charges and thus dipoles are created within the particle. However, as per definition, the diameter of a Rayleigh particle is small compared to the electromagnetic field it finds itself in and an approximation of the sphere as a single point dipole can be made.

The force on a dipole in an electromagnetic field can be calculated from the Lorentz force equation and is more commonly known as the *gradient force* in the optical trapping community.

$$\mathbf{F}_{\text{grad}} = \frac{\alpha}{2} \nabla \langle E^2 \rangle, \quad (1.1)$$

where α is the polarisability of the particle and $\langle E^2 \rangle$ is the square of the absolute value of electric field i.e. intensity of the beam. The polarisability of the particle is denoted α :

$$\alpha = n_m^2 r^3 \left(\frac{m^2 - 1}{m^2 + 2} \right). \quad (1.2)$$

where m is the relative refractive index between the trapped particle, n_p , and the surrounding medium, n_m , defined as $m \equiv \frac{n_p}{n_m}$. r is the radius of the trapped particle.

The *gradient force* is so called because the force on the dipole is linearly dependent on the gradient of intensity within the focussed laser beam. Both in the lateral and axial directions, the particle is attracted towards the point of highest intensity. However, in the axial direction the effect of the competing *scattering force* means that the particle does not sit exactly at the point of highest intensity but rather it sits slightly beyond the focus, down beam.

Trapping is more problematic in the axial direction than in the lateral directions for a couple of reasons; the *gradient force* is always fundamentally weaker in the axial direction compared to the two lateral directions, and *Rayleigh scattering* is almost only in the forward axial direction for dense media like a dielectric bead. The reduced *gradient force* in the axial direction is discussed in greater detail in section 2.2.2 but it suffices to mention here that the nature in which an objective lens focusses light and the presence of spherical aberrations both play important roles.

³Rayleigh particles are generally accepted as those with diameters less than 15 times the wavelength of light.

In the case of *Rayleigh scattering*, light can momentarily drive molecules into excited vibrational states after which the light is either re-radiated⁴ (*elastically scattered*) in all directions, or absorbed (*inelastically scattered*). Whether or not light is scattered or absorbed depends upon the wavelength of propagating light and the vibrational states available in the molecule i.e. a material can be transparent to some wavelengths and opaque to others.

For the case of *Rayleigh scattering* in a gas, the molecules have very little correlation to one another and scattered light can only be transmitted by constructive interference in the forward propagating direction. In all other directions, light has no correlation and the molecules behave as independent scatterers. Rayleigh found that the intensity of scattered light was inversely proportional to the fourth power of the wavelength. Therefore, the intensity of scattered light for shorter wavelengths is significantly larger than that for longer wavelengths. The sky appears blue because short wavelength (blue) light is scattered more, by molecules of the atmosphere, than longer wavelengths of the visible region (red).

However, if one considers dense materials, where the molecules are ordered and closely packed, then the re-radiated light is also taken up by the next molecule and scattered again. The waves of scattered light interfere constructively in the forward scattering direction because the path difference between scattering events is very small. However, unlike gases, dense materials like trapped dielectric spheres have a high degree of correlation in the lateral directions and the resulting interference is destructive, to the extent that little to no light is scattered laterally. Subsequently, the *scattering force* is not problematic in achieving stable lateral trapping but only in achieving stable axial trapping and is defined by Equation 1.3.

$$\mathbf{F}_{\text{scatter}} = n_m \frac{\sigma \langle P \rangle}{c}, \quad (1.3)$$

where c is the speed of light in a vacuum, n_m is the refractive index of the surrounding medium, and $\langle P \rangle$ is the time averaged Poynting vector.

The effects of wavelength, λ , and bead radius, r , on the *scattering force*, discussed earlier in section 1.2.1, are incorporated via the scattering cross section, σ , given by

$$\sigma = \frac{8}{3} \pi (kr)^4 r^2 \left(\frac{m^2 - 1}{m^2 + 2} \right)^2. \quad (1.4)$$

where k is the wave-number, $k \equiv \frac{2\pi n_m}{\lambda}$.

1.2.3 Absorption

Absorption, like scattering, is detrimental to achieving stable optical trapping because light that would have contributed to the *gradient force* instead becomes a source of heating. The effects of absorption can be devastating for biological material which is why it is important

⁴The delay between the uptake of a photon and the re-emission of a photon is what defines the refractive index, n , of a material.

to choose a wavelength that has little to no absorption in both the bead and the sample. Investigations of how optical tweezers affect biological material have been made [9, 10] while the heating of the probe particle is in most cases not an issue. However, for the special case where metallic nano-particles are used as probe particles, a theoretical study showed that the heating would be significant [11] but as of yet no experimental verification of this has been made.

1.2.4 Intermediate regime

The intermediate regime, where the bead size is comparable to the trapping wavelength ($d \sim \lambda$), is the regime where most biophysical experiments take place but it is also the most mathematically complex to model. The ray optics approach allows one to neglect the effects of absorption and reflection and the dipole method permits the approximation of the particle as a single point dipole, simplifying things considerably while maintaining a good qualitative agreement with experimental data. Unfortunately, no such approximations can be made for the intermediate regime and calculations of the complete electromagnetic theory must be made [12].

Indirect trapping is essential in biophysical experiments since most often the molecule under investigation cannot be directly trapped. Polystyrene beads that are two to three microns in diameter are regularly used because they are easy to manipulate and can be clearly seen by microscopy. Almost all experiments investigating biological systems use particles with diameters in the intermediate regime as *handles*. This necessitates careful calibration of the optical trap since the theory is complex and incomplete.

1.3 Calibration

There are many methods with which to calibrate optical tweezers but the same basic principle is used by all of them; a known force is applied to a trapped particle and a comparison with the optical restoring force is made. Chapter 2 discusses the use of Stoke's viscous drag as a known external force with which to investigate the extended trapping potential, whereas this chapter concentrates on the standard calibration method employed in most optical tweezers groups. i.e. the thermal noise of the particle in the trap is utilised as the force with which to determine the value of the optical restoring force. This is sometimes known as the power spectral density (PSD) method or power spectral analysis (PSA).

A particle suspended in a fluid is bombarded by the surrounding molecules of the fluid which cause the particle to *wiggle* around with random motion. This motion is a central part of the calibration of optical tweezers because it is the stochastic force from *Brownian motion* that drives the particle to explore the trapping potential and can be compared with the optical force by means of the *equipartition theorem*. A mathematical explanation follows in Section 1.3.2

1.3.1 Optical tweezers setup

The experimental set up is based on an inverted microscope (Leica DMIRBE or Leica DMI6000 SP5) into which 1064 nm light from a Nd:YVO₄ laser (Spectra-Physics Millennia) is coupled. The beam is first expanded (Casix 20×) to the extent where it overfills the back aperture of the objective (oil NA = 1.32 or 1.4, water NA = 1.2) and is steered into the microscope by two antireflection coated mirrors. The beam (with TEM_{00} profile) is then tightly focused to a diffraction limited spot ($d = \frac{\lambda}{2}$) in order to create an optical trap with a three dimensional intensity gradient. Axial positioning of the trap can be altered by translating the second lens in the telescope to focus at a new depth in the sample. The sample is mounted on a piezoelectric stage (Physik Instrumente, P-731.20 or P-517.3CL) with capacitive feedback facilitating translation with a precision of a few nanometres. Forward scattered light from the trapped particle is collected by the condenser lens and focussed onto a quadrant photodiode (QPD) (Hamamatsu S5981) situated at the back focal plane of the condenser. A charge coupled device (CCD) camera (Sony XC-ES50, 25 Hz) provides an additional form of detection but at a considerably reduced sampling frequency compared to that of a QPD (MHz range).

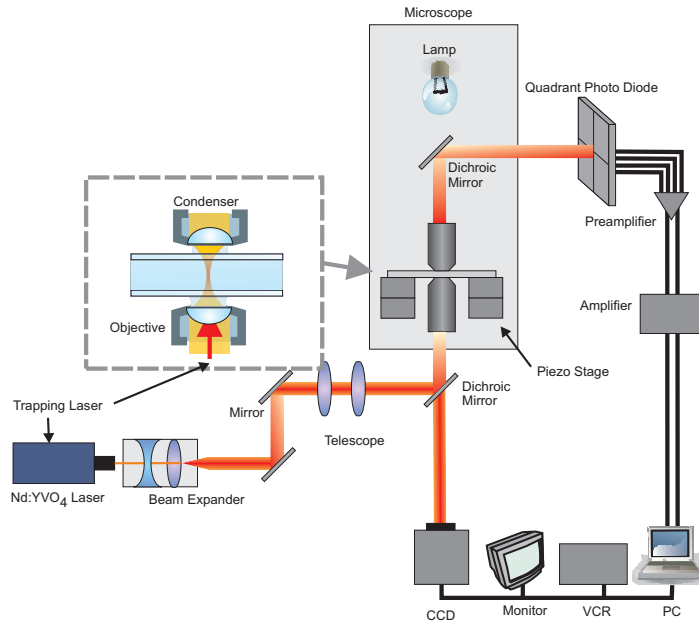


Figure 1.4: A standard optical tweezers setup like the one employed during the course of this research. Schematic courtesy of Dejan Trpcevski.

Figure 1.4 shows the standard optical trapping setup used in most optical tweezers experiments described in this thesis. During the course of this dissertation variations of this setup with small modifications specific to the experiment under discussion are presented but all are built on the same principle of integrating a laser into a microscope imaging

system.

Langevin equation

The 3D trapping potential created when laser light is focussed down is, to a good approximation, harmonic and independent in the three directions. Typically, the spring constant, κ , describing the direction along the propagating laser beam is significantly smaller than the spring constants describing the trapping efficiency in directions orthogonal to the propagating laser light. The restoring force, F , exerted in one dimension by the optical trap obeys Hooke's law:

$$F = -\kappa x \quad (1.5)$$

where x is the spatial deviation of the bead from its equilibrium position (trap centre).

As already stated, one way to find κ and hence perform a calibration of the optical trap is to utilise the *Brownian motion* of the bead in the optical trap. If a bead is held in an optical trap, its motion in one dimension, x , is well described by the *Langevin* equation:

$$m\ddot{x} = -\kappa x - \gamma\dot{x} + F(T, t) \quad (1.6)$$

in which γ is the friction coefficient of the bead and $F(T, t)$ is the stochastic force resulting from the *Brownian motion* at temperature T and time t .

For fluids with low *Reynolds* numbers, $\mathbf{R} \ll 1$, viscous forces dominate and the inertial forces can be neglected. Thus, the left side of Equation 1.6 can be set to zero. When far from any surfaces⁵, the motion of the bead in the fluid can be considered as a simple Stokes flow of viscous drag.

$$\gamma = 6\pi\eta r \quad (1.7)$$

Where r is the radius of the bead and η is the viscosity of the fluid.

1.3.2 Calibration by power spectral analysis

From Fourier analysis of equation 1.6, the power spectrum of the position x is found to be Lorentzian:

$$P_x(f) = \frac{k_B T}{\gamma\pi^2(f^2 + f_c^2)} \quad (1.8)$$

with a corner frequency $f_c = \kappa/2\pi\gamma$ from which κ can be found. In practice, however, a modified version of Equation 1.8 is used, this version taking into account the filtering effect of the quadrant photodiode, other electronic filters, aliasing and hydrodynamic effects [13].

⁵Faxen's correction which includes the effect of a surface must be included if the trapped bead is less than 5 radii from the surface

The distribution of positions visited by the bead, x , measured in Volts by the quadrant photodiode, is found to be Gaussian and from this the variance σ_V can be found in Volts. Furthermore, from the equipartition function we can find the standard deviation in meters, σ_m :

$$\sigma_m = \sqrt{\frac{k_B T}{\kappa}} \quad (1.9)$$

The ratio $\frac{\sigma_V}{\sigma_m}$ gives the conversion factor, β between Volts and meters. Knowing κ and x at all times, it is possible to find the force exerted by the optical trap, F .

Position detection

Finding the force exerted by optical tweezers requires accurate position detection; the position of a trapped particle, x , relative to the trap centre, can be found from the output voltages of a QPD. Unscattered light from the trapping laser as well as light scattered by the trapped particle is gathered by the condenser and directed onto a QPD, with some intensity distribution. The QPD converts intensity distributions into four voltage signals which can then be used to determine the position of a trapped particle in 3 dimensions.

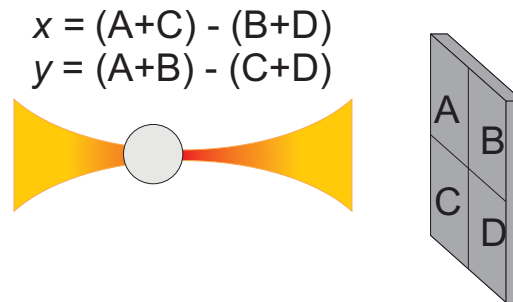


Figure 1.5: A rough representation of position detection by QPD is shown. Each quadrant creates a voltage signal that is a function of the incident light intensity. The x position is found by the sum of the voltage signals from the quadrants on the left, minus the sum of those on the right. y is similarly defined as the sum of the two upper quadrants minus the sum of the two lower quadrants.

Figure 1.5 shows how the position of the particle with respect to trap centre can be found for the two lateral directions. The location of the trapped particle in the axial direction can also be determined, its position is linearly dependent on the total intensity incident on the all four quadrants of the QPD and can be found by the sum of all the measured voltages. The extent to which the voltage signal produced by the QPD remains linear with incident intensity/particle position is discussed in Section 2.2.1 and shown in Figure 2.4 but it is safe to assume that the for *Brownian motion* of a trapped particle, the voltage signal is linear with the position of the trapped particle.

1.3.3 Calibration by viscous drag force

Drag force calibration experiments involve the application of an external force by accurately controlling the flow of liquid surrounding a trapped particle and observing the resulting voltage signals on a QPD. The external force applied can be very accurately determined using Stoke's law, if the velocity of the liquid is well known:

$$F_{\text{drag}} = 6\pi\eta av_{\text{liquid}}. \quad (1.10)$$

Where a is the radius of the bead and η is the viscosity of the surrounding liquid. The motion of the bead can be considered as a simple Stokes flow if the bead is far from any surfaces and thus the viscous drag force is simply proportional to the velocity of the surrounding liquid v_{liquid} .

Movement of the surrounding liquid can be achieved by constructing a flow chamber and gradually increasing the velocity of the surrounding liquid until the particle escapes, or more simply by moving the piezoelectric stage upon which the sample is held so that the surrounding liquid moves in unison with the stage. The later assumes that for a closed sample the surrounding medium and the stage move as one. The velocity of the stage is very accurately known and can be simply entered into Equation 1.10 to calculate the drag force on the trapped particle.

Comparison of the signals recorded by the QPD with the applied drag force gives a calibration of the force in terms of a measured voltage, i.e., the product of the conversion factor, β , and the spring constant, κ , is found.

Both PSA and calibration by viscous drag force are employed in the experiments described in Chapter 2. However, by employing CCD detection as well as a QPD in calibration experiments involving the viscous drag force, calibration factors β and κ can be separately determined by image analysis (Section 2.2.4).

1.3.4 Comparison of power spectral analysis and drag force calibration

Calibration by power spectral analysis is fast, automated, simple and can readily highlight the presence of errors over an entire frequency range. Furthermore, since the *Brownian motion* of the particle is itself utilised in the calibration process, no external movement of the stage or surrounding liquid is necessary. It does on the other hand, have a limited range over which its response is linear with particle position.

Calibration using the viscous drag force and CCD detection is more time consuming and has considerably lower temporal (25 Hz) and spatial (6 nm) responses. However, for some specific applications, the larger *linear detection region* offered by CCD detection and the considerably larger forces applicable by viscous drag as opposed to *Brownian motion* make this a valuable experimental calibration choice. This is evident in the investigation of trapping potential presented in Chapter 2.

1.4 Summary

The theory behind optical trapping and the basic experimental setup of optical tweezers have been introduced as well as a couple of calibration methods that allow optical tweezers to be used as a force transducer. However, finding the spring constant, κ , inside a living cell requires an alternative calibration method because the cytoplasm of a cell cannot be treated as a simple viscous fluid and its properties are largely unknown. The complexity of the cytoplasm makes *in vivo* calibration all the more challenging, it is addressed in Chapter 4. Chapter 2 employs the two described calibration methods to investigate the range over which the trapping force remains linear with particle displacement from the trap centre.

CHAPTER 2

An investigation of optical trapping potential by the suppression of spherical aberrations

It is well known that by tightly focussing a beam with a *Gaussian intensity profile*, the optical trapping potential created is, to a good approximation, harmonic in all three directions. Albeit, slightly ellipsoidal because of the reduced potential in the axial direction. However, it is not clear to which extent this approximation holds or up to what point the *linear region* persists, i.e., how far from the trap centre the force can be considered as linearly dependent upon particle position. This chapter discusses an experimental investigation wherein the boundaries of the *linear region* of the optical trapping potential are determined, through the employment of a simple but effective technique to compensate for spherical aberrations [14].

2.1 Overview

Quantifying the extent of the lateral trapping potential's *linear region* is interesting and relevant with respect to the primary goal of investigating the nano-mechanics of cell division, particularly for beads in the 2-3 μm size range. The handle size in many DNA pulling experiments is within this range and it is not uncommon for these handles to be used to apply forces in excess of 100 pN, for example, when investigating how intercalaters affect DNA molecules [15]. Therefore, it is more than likely that the handle visits very extreme points of the potential in the course of generating these forces; this, of course, raises the question as to whether the measured forces can be trusted or not because they are based on an assumption that the lateral spring constant measured close to the trap centre continues with indefinite linearity until axial equilibrium is lost.

This chapter begins by discussing the findings of two other research groups who have made investigations relating to the escape trajectories of beads held in single-beam gradient optical traps [16, 17]. In particular, their examination of the maximum transverse trapping force and the disagreement between the measured value and the value predicted by theory are considered. Thereafter, I describe how a known method of reducing spherical aberrations [14] was used within a modified version of the experimental procedure employed by Marena *et al.*, to give an experimental value of the maximum lateral trapping force which is more agreeable with theoretical predictions.

Furthermore, the modified experimental method also allowed the *linear region* of the lateral trapping potential to be determined and revealed a stiffening of the potential at extreme positions. Lastly, the implications of the observed stiffening, with respect to DNA pulling experiments, and a possible explanation as to the source of the stiffening are proposed.

2.1.1 Previous experimental work

The optical restoring force was first shown to be linearly dependent upon the displacement of a trapped bead, displaced laterally in the trap, some 15 years ago [18]. It was shown that, for a $0.55\ \mu\text{m}$ bead, the force displacement profile remained linear approximately 100 nm either side of the trap centre which supported theoretical predictions made by Ashkin the year before [7]. Since then, it has been assumed that, provided the displacement of the bead is small, the potential is harmonic and the lateral trapping force depends linearly upon displacement.

However, it is well known that the axial equilibrium position of a trapped particle is slightly down beam from the laser focus because of the large scattering force acting in the axial direction [7, 19], and is even further down beam in the presence of spherical aberrations [20, 21]. A bead at the axial equilibrium position can hence also find itself somewhat shifted from the point of highest lateral trap stiffness [22], depending on how far the axial equilibrium position is from the true laser focus. By use of a DNA tether connecting the surface of a sample chamber to a bead in the trap, Wang *et al.* [23] were able to step the bead through the laser focus in increments of 20 nm and, thereby, measure the lateral trap stiffness for various axial positions. They reported a significant difference in the lateral trap stiffness measured at the axial equilibrium position compared to that measured at the true focus of the laser, a substantial factor of 1.5. It is thus evident that if the bead moves axially from the focus then the lateral stiffness is reduced.

Perhaps more interestingly, one could consider the case where the axial position of the bead is maintained and the bead is stepped only in the lateral direction; this is, in fact, the assumption upon which almost all theories pertaining to the calculation of the maximum transverse trapping force are based [21, 24].

Some recent experiments investigated the axial position of the bead as a function of its lateral position in the trap [16, 17]. They showed that when the bead is displaced in the transverse direction by an external force, the viscous drag force caused by the movement of the surrounding fluid in the direction orthogonal to beam propagation, there is also a significant movement of the bead in the axial direction. Therefore, the maximum value of lateral trapping force is overestimated if axial equilibrium is neglected [16]. Theoretical predictions overestimate the maximum transverse force because of their implicit assumption that the bead remains in the plane orthogonal to beam propagation [16].

In actual fact, the bead follows a trajectory of axial equilibrium and was progressively shifted further from the beam focus in the axial direction as the viscous drag force was increased. Of key importance is the observation that the bead escapes the trap when the first equilibrium is broken, in either of the directions [16]. More correctly, the bead is always observed to escape in the axial direction because axial equilibrium is broken first. i.e. before the maximum lateral trapping force can be reached [16, 17]. Marendra *et al.* reported that the bead escaped the trap at a lateral position of $0.59 a$ from the beam axis, where a is the radius of the trapped bead, and similarly the proceeding work of Gong *et al.* found that the bead escaped at a lateral position of $0.55 a$. Figure 2.1 shows the axial displacement of a bead in the optical trap as a function of its lateral position in the trap, as reported by Gong *et al.*

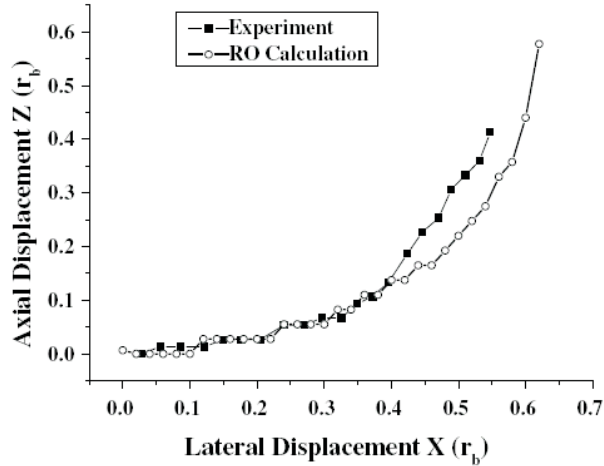


Figure 2.1: The axial position of a trapped bead is plotted as a function of its lateral position in the trap for both experiment, filled squares, and that theoretically predicted by ray optics calculation, open circles. The displacements of the bead from trap centre are plotted as a fraction of the bead radius for a $3 \mu\text{m}$ bead. The bead escaped at around half the radius of the trapped bead which agrees well with the ray optics calculation that accounts for spherical aberrations. Figure reproduced from Gong *et al.*

Chapter 2: An investigation of optical trapping potential by the suppression of spherical aberrations

However, neither study observed that beads could reach the kind of lateral positions for which the maximum lateral trapping force is predicted to occur ($0.83 a$ [16]) based on calculations neglecting axial equilibrium. Moreover, considering the track of axial equilibrium leads to a predicted lateral escape position ($0.6 a$ [17]) that is in good agreement with the reported experimental values [16, 17]. It also infers that, under standard trapping conditions, the predicted stiffening [7] cannot possibly be observed because there exists no axial equilibrium for lateral positions where the stiffening becomes visible.

When Gong *et al.* modelled the lateral trapping force with and without the inclusion of axial equilibrium considerations, the comparison revealed less than a 2 percent difference in the lateral trapping force for the two cases, provided the lateral displacement was less than $0.5 a$. Ray optics calculations do not predict a linear relation between lateral trapping force and lateral position, but below $0.5 a$ a linear approximation is valid. Above $0.6 a$, the two cases are predicted to diverge significantly (10 percent difference) from each other but because the bead escapes in the intervening region, an experimental observation of the stiffening is impossible as was previously inferred. The predictions of Gong *et al.* are presented in Figure 2.2.

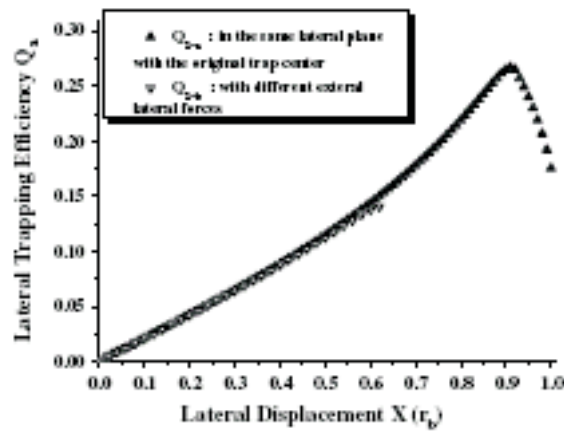


Figure 2.2: The lateral trapping efficiency is shown versus lateral displacement for two theoretical cases: where the trajectory of the trapped particle is assumed to be in the same orthogonal plane as trap centre i.e. no axial movement (filled triangles), and where the trapped particle moves along its axial equilibrium trajectory (open triangles). Lateral displacement is shown as a fraction of the bead radius and trapping efficiency is dimensionless. This figure is the work of Gong *et al.*

If it were possible to reduce the axial shift of the bead experimentally, maintaining the axial equilibrium position close to the plane orthogonal to the beam axis, a better estimate of the maximum lateral trapping force could be found and perhaps the predicted stiffening of the potential would be observable.

2.1.2 Theoretical predictions

Theoretical predictions have been thrown around and compared to experimental data without explanation in Section 2.1.1. Rigorous explanations of the various models will not be made but it is important that the relevant assumptions of each model are considered so that the validity of their comparison to experimental values may be evaluated.

Ashkin was the first to make calculations of the forces exerted by optical tweezers and in 1992 he made detailed ray optics calculations of the gradient, scattering and total force on the bead as a function of both the axial and lateral positions of the bead in the trapping beam [7]. Equations 2.1 and 2.2 are the basis for these calculations.

$$F_z = F_{scat} = \frac{n_1 \mathbf{P}}{c} \left\{ 1 + R \cos 2\theta - \frac{T^2 [\cos(2\theta - 2r) + R \cos 2\theta]}{1 + R^2 + 2R \cos 2r} \right\} \quad (2.1)$$

$$F_y = F_{grad} = \frac{n_1 \mathbf{P}}{c} \left\{ R \sin 2\theta - \frac{T^2 [\sin(2\theta - 2r) + R \sin 2\theta]}{1 + R^2 + 2R \cos 2r} \right\} \quad (2.2)$$

where θ and r are the incident and refraction angles, R and T are the Fresnel coefficients of reflection and transmission, c is the speed of light in a vacuum, \mathbf{P} is the laser power and n is the refractive index of the surrounding medium.

The theoretical calculations of Gong *et al.* [17], shown in Figure 2.2, were based upon these formulas but included the additional effects of spherical aberrations as developed by Fällman *et al.* [20]. It is reasonable that they decided to employ the ray optics approach (valid for $d \gg \lambda$) because the trapping laser has a free space wavelength of 632 nm, 475 nm in water, and is used to trap beads with diameters of $3 \mu\text{m}$. The lateral trapping efficiency, Q_x , was calculated as a function of lateral position for the equilibrium track and compared to that of a bead moving only in the transverse plane.

Marenda *et al.* decided to make use of two different theoretical approaches and to compare their experimental data with the predictions of both models [16]. They also computed the forces on the bead for the equilibrium trajectory and for a pure transverse displacement of the bead in the focal plane. Firstly, they used a hybrid mathematical model combining simple ray optics with the complexity of a complete electromagnetic field approach. The advantage gained for this additional complexity is that spherical aberrations from the coverslip/water interface are considered and the particle size with respect to the size of the focus is included. Secondly, they use the simple ray optics approach which does not include the effects of spherical aberrations.

2.2 Characterising the optical trapping potential

2.2.1 Experimental setup

The experimental setup used was the same as that portrayed in Figure 1.4 and further described in Section 1.3.1, with the exception of an additional lens ($f = 50$ mm) placed in front of the CCD camera. The lens acts to increase the size of the image incident on the CCD so that the diameter of the bead is half the width of the CCD's active detection region. This serves to enhance the spatial resolution of the bead's movement above the 1:1 image exiting the microscope but also results in a slightly de-focussed image. However, the de-focussing posed no significant disadvantage to this investigation. The experimental setup used for the investigation of optical trapping potential is shown in Figure 2.3.

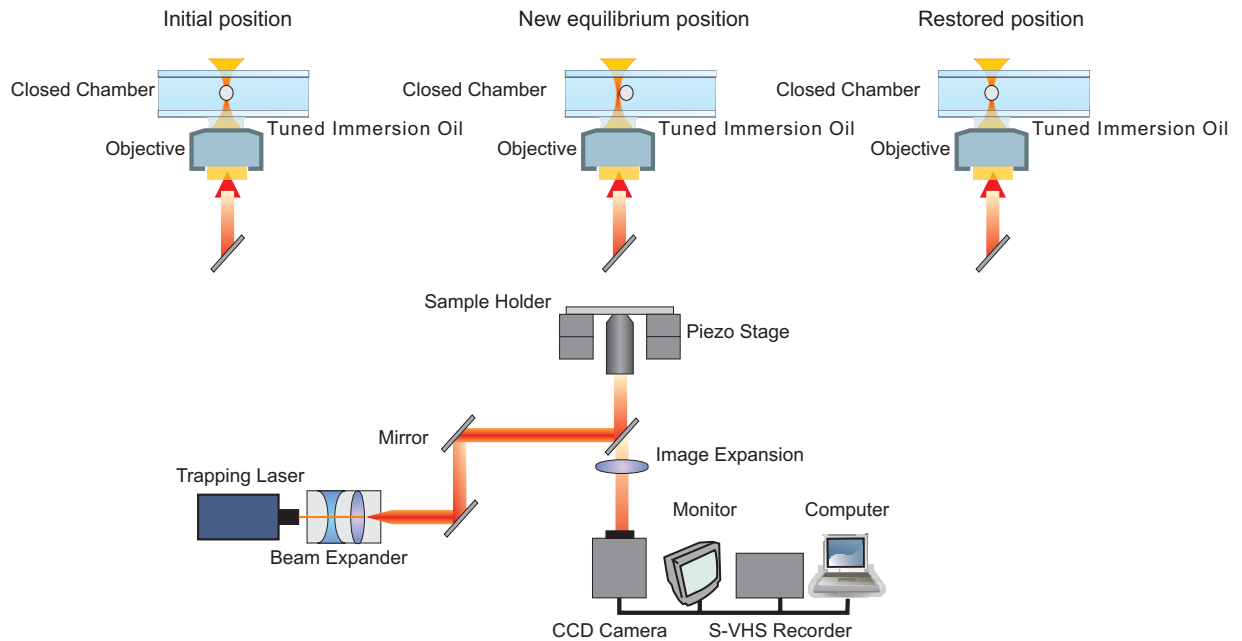


Figure 2.3: The modified experimental setup used to investigate optical trapping potential, including a close up of the modified CCD position detection. The schematic is a modified version of that by Dejan Trpceviski.

As Figure 2.3 implies, optical tweezers are created identically to those described in Section 1.3.1. There is, however, a difference in experimental approach. The CCD camera is used as the primary method of position detection, to calibrate the optical trap by means of the drag force method, instead of employing power spectral analysis (PSA), calibrating using a quadrant photodiode (QPD) and *Brownian motion* of the bead. There are two very good reasons why PSA could not be used here and why a QPD was not suitable as the primary method of detection for this investigation.

Firstly, *Brownian motion* typically explores the trapping potential close to the trap centre. That is to say, the movement of a trapped particle under *Brownian motion* remains within the *linear region* of the optical trapping potential. Therefore, determining the shape of the trapping potential at extreme positions, outwith the *linear region* explored by *Brownian motion*, necessitates the use of an external force to drag the particle to the edges of the trapping potential and thereby force the particle to explore these rarely visited points of the potential. The viscous drag force is ideally suited to such an investigation because the applied force is both well known, (Eq. 1.10), and can be easily modified by means of the stage velocity. However, PSA is used as a secondary method to confirm that the value of the measured trap stiffness (for the *linear region*) is in good agreement for both detection methods.

Secondly, the range over which the voltage output of a QPD remains linear with bead position (*linear detection region*) is small in comparison to the range of bead movement for which the number of pixels transcended by the bead remains linear on a CCD camera. i.e. the response of the CCD camera is linear over a larger range of bead movements than the response of the QPD. If one is to investigate the extent of the *linear region* of the trapping potential, it is essential that the detector has a response that is linear for larger displacements than those necessary to determine the boundary of the *linear region*. In other words, the *linear detection region* of the QPD, see Figure 2.4, ends before the *linear region* of the potential can be ascertained. Therefore, the CCD camera is preferable in determining the outer limit of the *linear region* of the trapping potential. Figure 2.4 shows positional calibration of the QPD. A $1\mu\text{m}$ diameter bead, stuck to the coverslip, is moved through the trap focus in the lateral direction using a piezoelectric stage while the output signal of the QPD is recorded.

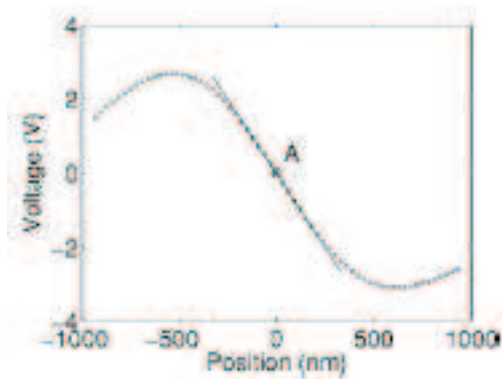


Figure 2.4: The quadrant photodiode response is shown versus the position of the piezoelectric stage used to move a stuck $1\mu\text{m}$ diameter particle laterally through the focus of the laser. The linear detection region extends approximately half the radius of the trapped particle, either side of trap centre.

Figure 2.4 was taken from a manual describing the basics of optical tweezing for undergraduate students [25].

So as to avoid confusion, it should be stressed that the range over which the optical restoring force remains linearly proportional to bead displacement is termed the *linear region*, and is not the same as the *linear detection region* of the QPD. A similar experimental determination of the linear region in the axial direction can be made by moving a stuck bead axially through the focus of the trap.

2.2.2 Compensation for spherical aberration

Optical tweezers (single beam optical traps) have an inherently weaker trap stiffness in the direction along the propagating laser beam, κ_z (axial direction), compared to that of the directions orthogonal to laser propagation, κ_x, κ_y (lateral directions) [26]¹. The difference in trap stiffness between the axial and lateral directions is due, in part, to the increased *focusability* of the objective in the lateral directions. Put differently, the intensity gradient is steeper in the lateral directions because of the nature in which light is focussed by an objective lens. Albeit, the most significant factor contributing to the reduced axial trap stiffness in infra-red, laser based, optical tweezers is the degradation of the focussed beam by spherical aberration [20]. This is especially problematic for oil immersion objectives, where the aberration is highly dependent on the axial point of focus in the sample.

Spherical aberration is the most significant of the third order aberrations, otherwise known as *Seidel aberrations*. As such, great care is taken in the design of optical elements so that spherical aberration is eliminated. An example of a system containing multiple optical elements, for which extensive optical design is carried out, is an objective lens. An oil immersion objective lens is designed for observing a sample on a glass surface, where the refractive index of the oil is index matched to both the objective lens and the glass cover slip. However, when using an objective lens out of context, one can incur significant aberrations.

For example, optical tweezers are often focussed inside an aqueous medium containing biological samples which may not necessarily be located close to the surface. Spherical aberration enters because of the refractive index mismatch between the glass cover slip and the water based sample and becomes progressively larger as the beam is focussed further from the interface, according to Equation 2.3 [14].

$$SA_{\text{total}} = SA_{\text{tube}} + SA_{\text{obj}} + SA_{\text{im/cov}} + SA_{\text{cov/sample}}, \quad (2.3)$$

where SA_{tube} is the contribution toward the total spherical aberration in the system arising from the tube length, SA_{obj} from the lenses making up the objective lens and the last

¹It is worth mentioning that the two lateral directions are generally observed to have very similar values of trap strength, for a well aligned system.

two components contributing spherical aberrations, $SA_{\text{im/cov}}$ and $SA_{\text{cov/sample}}$ come from the refractive index mismatches between immersion media - coverslip and coverslip-sample, respectively.

Furthermore, standard microscope objective lenses are optimised to minimise *Seidel aberrations* in the visible region of the electromagnetic spectrum (400 - 700 nm), not for the infra-red laser light (1064 nm) commonly used in the creation of optical tweezers for biophysical measurements. Therefore, there will also be some *Chromatic aberration* because of the wavelength dependent refractive index of the objective lens. There are oil immersion objectives available that have been optimised for use with both visible and infra-red light but they tend to be very expensive.

A cheap but effective method of eliminating spherical aberrations, reported by Reihani and Oddershede [14], is to use an immersion medium with a refractive index that is incorrectly matched to that of the coverslip. Thereby, one can introduce spherical aberrations which cancel those originally present in the system. The depth at which the cancellation of aberrations takes place can be controlled by carefully selecting the refractive index of the immersion oil. It was reported that the ratio between lateral and axial trap stiffness can be reduced from a factor of 10 to a factor of 2 - 3, while also increasing the lateral trap stiffness [14], i.e., it is a biased rate of increase of the axial trap stiffness compared to the increase in lateral trap stiffness that reduces the ratio and not a decrease in the lateral direction which enhances the ratio.

Reihani postulated that by using his previously reported technique of suppressing spherical aberration [14], one could achieve greater axial confinement of the trapped particle and in turn obtain a better estimate of the maximum lateral trapping force. i.e. the bead should remain in the trap at larger lateral displacements if the axial confinement can be increased. Furthermore, this would allow the application of larger optical forces for the same laser power.

This simple yet effective method of increasing the axial trap strength is utilised to explore the extended lateral trapping potential. Hereafter, the technique in which the refractive index of the immersion media is optimised, to minimise spherical aberration, will be referred to as the method of optimised immersion medium (*OIM*). For the *OIM* method, the optimal immersion medium for trapping at a depth of $5 \mu\text{m}$ had a refractive index, n , of 1.54. The same experimental procedure as is described in Section 2.2.3 was used to investigate the trapping potentials in both the *OIM* case and the case where the standard immersion medium, *SIM*, was used.

2.2.3 Experimental procedure

The *SIM* recommended for use with Leica oil immersion objectives (refractive index, n , equal to 1.518) was used to reproduce the work of Marendra *et al.* [16]. Marendra *et*

al. observed that the movement of a trapped bead as it is forced laterally out from the trap centre is not constant in the axial direction, but instead follows a trajectory of axial equilibrium, see Section 2.1.1.

The sample was a simple perfusion chamber containing polystyrene beads of diameter $2.1 \mu\text{m}$ with a standard deviation of $0.05 \mu\text{m}$ (Spherotech) or $2.01 \mu\text{m}$ with a standard deviation of $0.17 \mu\text{m}$ (Bangs). Laser light is focussed to a diffraction limited spot, approximately $1 \mu\text{m}$ in diameter, at a depth of $5 \mu\text{m}$ inside the sample. The accuracy of the focus position in the axial direction is subject to an error of approximately half a micron either side of set depth.

Diverging momentarily, this is of very little significance in the experiments where the *OIM* method was employed because the trap stiffness has been shown to be very resilient to small variations in depth around the optimal depth for the chosen immersion medium [14]. For example, Figure 2.5 shows that the spring constant is highly dependent on the trapping depth away from the optimal trapping depth, but at the peak the dependency is quite flat. In particular, the immersion medium used in the *OIM* method shows similar values of spring constants 1 micron either side of the optimal trapping depth of $5 \mu\text{m}$. Consider the data series represented by hollow diamonds in Figure 2.5, this represents the same experimental conditions for *OIM* as were used in this investigation. The figure is reproduced from a recent article outlining the novel compensation method [14].

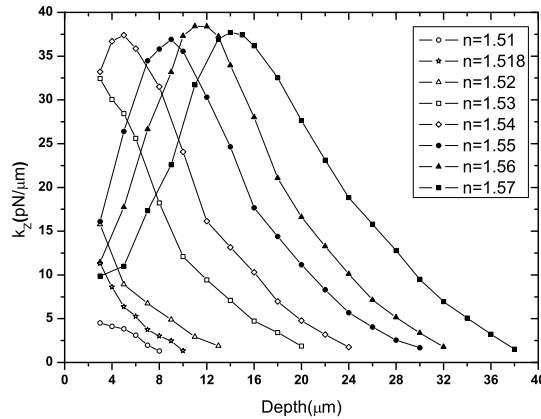


Figure 2.5: The graph shows how the axial spring constant changes with trapping depth for immersion media with different refractive indices. The immersion medium used by the *OIM* technique (hollow diamonds) shows similar values of spring constant for depths of 4, 5 and $6 \mu\text{m}$.

On the other hand, experiments made using the *SIM* face fairly substantial variations in the axial spring constant, κ_z , for relatively small errors in setting the trapping the depth. See Figure 2.5 (open stars).

Returning to the sample, a bead was held at the focus of the trap and the Piezoelectric stage, upon which the sample was mounted, was moved. This gave rise to a viscous drag

force in the transverse direction, as described in Section 1.3.3, that pushed the bead laterally out from the trap centre. The concentration of beads in the sample was extremely low so that the probability of a second bead entering the trap was small and the likelihood of measuring on the same bead twice was negligible. In addition, the millipore water used for dilution was further cleansed of debris by means of a porous filter (200 nm pore size, Eppendorf), reducing the frequency at which pieces of dirt found their way into the trap. In many cases, the presence of even a small piece of dirt had the effect of artificially increasing the value of the escape velocity. The entire data series was neglected for experiments where this occurred, either immediately upon entry of the dirt into the trap, or after data analysis later revealed that this had happened. Data analysis of the beads axial and lateral positions were made retrospectively by image analysis of the experiment, recorded by VHS. The finer details of the analysis process are discussed in Section 2.2.4.

In order to obtain data for both sides of the potential, the stage was first driven in the positive x direction (defined as a standard coordinate system would be when facing the setup), held stationary for 5 seconds, then driven in the negative x direction at an identical velocity to that used for the positive direction. The stage was controlled using a fully automated LABview program, `escapetrajectory2.vi`, written by S. Nader. S. Reihani. The described driving was repeated ten times for each velocity, progressively increasing the velocity in increments of $15 \mu\text{m/s}$ up until the final velocity where the bead escaped. The advantage of this method is that the depth of focus of the laser remained constant for the entire experiment (particularly important in the *SIM* method, see Figure 2.5), which is not the case if making ten individual experiments up until the bead escapes because the bead would have had to have been recaptured and the focus reset nine separate times. However, the disadvantage of this methodology is that the final escape velocity, or maximum lateral force applicable, for which the bead remains in the trap is only obtained once for each bead. This was overcome by making a large number of separate experiments, to find the mean escape velocity and standard deviation, without making time consuming video analysis of the images.

One should also clarify that the escape velocity was defined as the last velocity at which the bead remained in the trap and not the velocity that caused the bead to escape. In the event that these two velocities were of the same value, i.e. the bead remained in the trap once at a specific velocity and then escaped on the next attempt under the same velocity, it was still defined as the escape velocity.

The stage was always moved a fixed distance of $30 \mu\text{m}$ but with velocities ranging from $10 \mu\text{m/s}$ - $400 \mu\text{m/s}$, depending on whether the *SIM* (with aberrations) or the *OIM* (without aberrations) was applied to the objective. Escape velocities tended to be a little over $200 \mu\text{m/s}$ for the *SIM* and just below $400 \mu\text{m/s}$ for the *OIM*, which were far enough away from the upper limit of the stage movement ($1000 \mu\text{m/s}$) that the movement of the stage could be trusted. A distance of thirty microns movement was selected because it gave

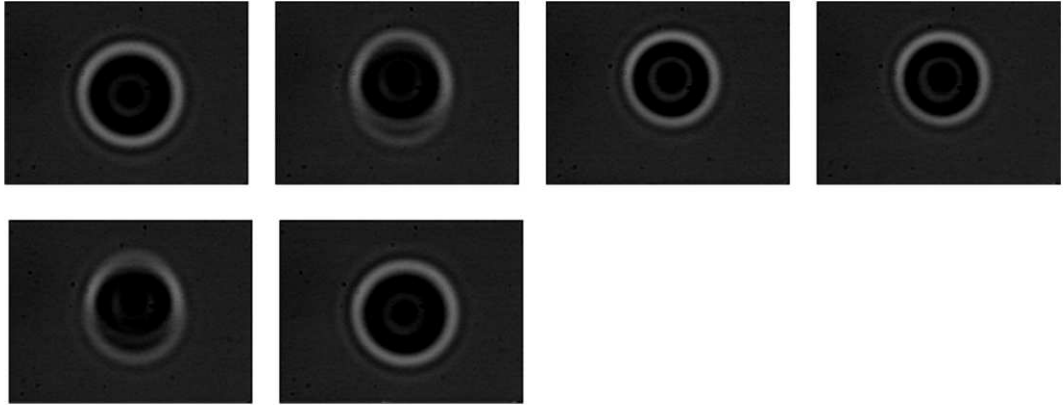


Figure 2.6: The movement of the bead can clearly be seen by the blurring of the image at the edges. The equilibrium point should always have at least one very sharp image. The image furthest to the left on the upper line is the starting position and immediately to its right is a single image showing the movement of the bead towards the equilibrium position (blurred). The last two images on the top line show the bead at the equilibrium position (stationary). The bead is shifted upwards in comparison to the image of the starting position and also appears smaller in diameter, showing lateral and axial displacement respectively. Finally, the first image on the bottom line confirms the movement of the bead back to its original position (blurred) and the last image, final position, should be identical to that of the starting position.

at least one stationary image of the bead at the new equilibrium position, a fact which is still valid for the fastest velocity under conditions of *OIM*. This can be observed in Figure 2.6. Frames in which blurring occurred represented periods of stage motion and subsequent bead movement. The CCD was deliberately set to its slowest possible shutter speed, 10 ms, so that the maximum amount of light could be collected and so that frames sandwiched between blurred frames could definitely be associated with the new equilibrium position.

The laser power at the focus was measured to be 15 mW, using two identical objective lenses and a power meter while also assuming that both objectives have the same transmission. The acquisition rate of the video recorder was 25Hz. These values were important factors in selecting an appropriate distance to move the stage because: (a) the escape velocities of both methods had to occur before the upper limit of the stage movement was reached; (b) the time spent at the equilibrium position had to be larger than equivalent to one frame of normal video rate acquisition, 40 ms. For the largest of the velocities used, the minimum duration of stage motion was 78 ms. This is large in comparison to the characteristic equilibrium time of the bead in the trap, 17 ms, given by the inverse of the average

measured corner frequency, $f_c = 60$ Hz. Therefore, the bead most certainly reached the new equilibrium position for each stage velocity. Likewise, a five seconds pause before driving the stage in the negative x direction was most certainly sufficient enough to allow the bead to return to the trap centre, the original point of equilibrium.

2.2.4 Image optimisation and image analysis using LABview

The white outer ring seen in the bright field images of the bead, Figure 2.6, provides a simple method of determining the lateral and axial displacements, by image analysis. Lateral displacement was easily monitored by tracking the centre of this ring and counting the number of pixels displaced for each movement of the bead.

As previously stated, the stage was moved ten times at the same velocity before proceeding to the next velocity in the sequence. Therefore, an average of the ten displacements was made for each velocity and this was done for five individual beads from the same sample. Lower stage velocities had several images of the bead at the new equilibrium point, point of maximum lateral displacement, whereas at the fastest stage velocity there was only one or sometimes two images because of the frame rate of the CCD camera. Nonetheless, only the image which showed the largest lateral displacement for each stage movement was used to obtain the average displacement for each velocity. *Brownian motion* was, of course, influencing the movement of the bead while at the new equilibrium point but the protocol of always using the largest lateral position reached by the centre of the bead was followed throughout so that the error introduced would be a systematic one. The same was true at the other end of the measurement; the starting position of the bead, before the stage was moved, was recorded as being the furthest position the centre of the bead reached in the direction opposite to that in which the stage moved.

Tracking the position of the bead was done using an automated LABview program, displacement&radiusfinder6.vi, written by S.Nader. S.Reihani. All image analysis was also carried out by him. Figure 2.7 shows the way the bead was converted from a bright field image into a binary image of black and white pixels. The decision level for defining a pixel as being black or white was kept constant for the entire analysis of each data set, i.e., one bead from starting velocity until escape velocity but not necessarily for different beads on the same day.

Thereafter, a box was drawn around the white outer ring and the centre of the box marked with a red cross hair to represent the centre of the bead.

There are many sophisticated techniques available with which to the quality of an image can be improved after it has been taken but in all cases it is better to optimise the image quality beforehand. With this in mind, the microscope was placed into Köhler illumination and the intensity of the bright field light source optimised in order to achieve the maximum contrast of the white outer ring. This was done, *in situ*, using another small LABview

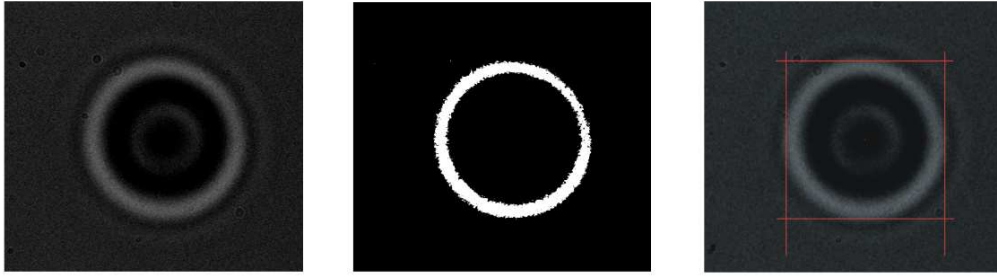


Figure 2.7: The original image is shown on the left hand side, the binary image produced to enable tracking of the bead is shown centrally and the image as it appears when using the analysis program is displayed to the right hand side.

program, `imagequalitytest.vi`, written by the same author as before.

After experiments were made the lateral displacement of the bead in the trap was found by counting the number of pixels displaced laterally by the bead, between its starting position at trap centre and its new equilibrium position under the applied external force. The axial displacement was found by recording the change in diameter of the white ring in the image of the bead during the same time period.

2.2.5 Pixel calibration

Various methods of retrieving the absolute axial position from an image have been demonstrated, fluorescent [27] or otherwise [28]. The first technique is very similar to the method employed in this investigation except that they utilised the point spread function (PSF) of a small fluorescent bead. They found that the PSF was linearly dependent upon axial position and with a standard deviation of 0.9 nm. Another method [28], which is less accurate (sd. = 5 nm) but has the advantage that it is applicable to bright field images of micron sized beads, involves fitting to complex functions of the bead's area. A quick and simple method of obtaining the relative axial position of the bead was instead used here, albeit with a greater uncertainty than Hansen *et al.* achieved.

A bead stuck to the coverslip was stepped in axial increments of 50 nm for a total of 2 μm movement. The diameter of the white outer ring, the width of the red box in Figure 2.7, was found to depend linearly on the axial position of the stuck bead as it was stepped down through the focus of the objective. It was assumed that the same dependency held for a bead moving axially within the trap because it moves axially with respect to the focus of the objective, too. The calibration curve is shown in Figure 2.8.

The relative axial displacement of the bead can be resolved by comparing the width of the red box in the image, diameter of the white outer ring, at the starting position and that at the new equilibrium position. A change of one pixel in the diameter of the white

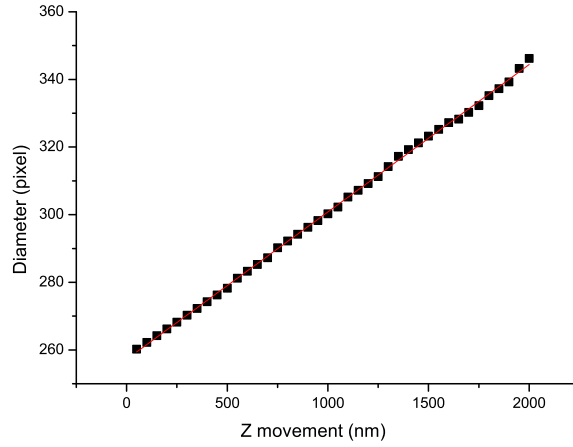


Figure 2.8: The diameter of the white outer ring from the bright field image of a $2.1\ \mu\text{m}$ bead, as a function of axial position (height).

outer ring corresponds to an axial shift of the bead by approximately 20 nm. This was found by fitting the data points in Figure 2.8 to the equation of a straight line, where the inverse of the gradient of the fitted line was 19.8 nm and is the equivalent of pixel size. The disadvantage of this simple and effective technique was that it was slightly susceptible to fluctuations in light intensity because the diameter of the white outer ring, as well as being linearly dependent on depth, was also effected by the background light intensity. However, maintaining the bright field light source at a constant level and also covering the condenser arm with black cloth helped maintain the light intensity for much longer than the experiment duration of thirty minutes.

Similar calibration curves were made for the $2.1\ \mu\text{m}$ beads (Spherotech) as were made for the $2.01\ \mu\text{m}$ beads (Bangs), using both the *SIM* and the *OIM*; the curves were so similar that, thereafter, calibrations were only made one time for each day where experiments were performed and only for the $2.1\ \mu\text{m}$, *SIM* case. A comparison of calibration curves for a $2.1\ \mu\text{m}$ bead using both methods is shown in Figure 2.9.

Lateral pixel calibration was equally as simple and followed the well established procedure of moving a stuck bead in many well defined steps and averaging the number of pixels between movements. The piezoelectric stage can be moved in very precise increments and was moved in numerous 100 nm steps so that the average number of pixels per step could be measured by image analysis. The lateral pixel size was thus calculated as 11.3 nm from the fitted lines of Figure 2.10.

Axial pixel calibration was shown to be independent of the type of immersion medium used and a similar check was made for the lateral pixel calibration. The pixel sizes obtained from each method were 11.38 nm and 11.21 nm for the *SIM* and the *OIM*, respectively. The

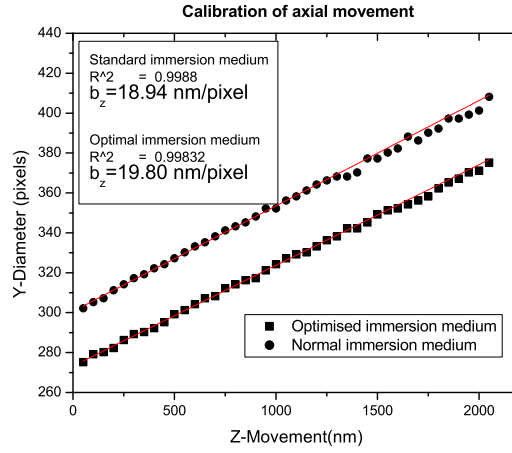


Figure 2.9: Axial pixel calibrations made by *SIM*, dots, and *OIM*, squares, are shown. The difference in pixel size was less than 1 nm, approximately 5 percent, and was neglected.

difference is within the measurement uncertainty of one method and so was neglected. Pixel calibration was again only made once per day of experiments using the *SIM*.

2.3 Results and discussion

Reducing spherical aberration resulted in an increased axial confinement of the trapped particle which in turn facilitated an extended mapping of the optical trapping potential to points outwith the *linear region*.

2.3.1 Increased axial confinement

It was visibly evident that as the velocity of the stage was increased, forcing the bead to larger lateral displacements, the axial movement of the bead in the trap was reduced for the *OIM* when compared with the *SIM*. This can be seen qualitatively from Figure 2.11.

This primitive analysis clearly indicates that the bead remained close to the plane orthogonal to beam axis, in the *OIM* case, because the diameter of the white outer ring in the image of the bead appeared constant over the entire velocity range up until the point of escape. This is in stark contrast to the significant change in diameter observed for the experiments that made use of the *SIM*.

Movement of the bead was also analysed quantitatively, using the image analysis techniques described in Section 2.2.5. Only then, could more valuable comparisons to previous investigations of escape trajectory, discussed in Section 2.1.1, be made. The quantitative result of image analysis is shown in Figure 2.12

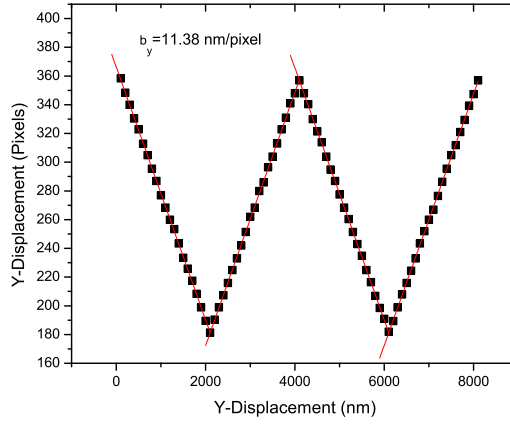


Figure 2.10: Lateral pixel size calibration. The stuck bead is moved forwards and backwards in accurate steps of 100 nm to determine the average pixel size.

Even for the situation where spherical aberrations were eliminated *OIM*, the $2.01 \mu\text{m}$ bead still moved an average distance of $118 \pm 46 \text{ nm}$ in the axial direction which was impossible to see by eye in Figure 2.11. This can, however, be roughly approximated as moving in the horizontal plane, passing trap centre, when compared to the huge axial movement seen in the aberrated case; Wherein, an average axial movement of $572 \pm 112 \text{ nm}$ was observed before the bead escaped. However, it is also possible that spherical aberrations were just reduced and not completely eliminated, which may explain the axial movement seen for the bead when the *OIM* was applied.

Corresponding lateral positions reached at the point of escape were $566 \pm 19 \text{ nm}$ and $615 \pm 17 \text{ nm}$ for the *SIM* and the *OIM*, respectively. This represents an increase of just under 10 percent in the maximum lateral displacement reached while still in the trap. The purpose of this part of the investigation was merely to show that the hypothesis of Reihani was correct in so much as the elimination of spherical aberrations did result in a greater axial confinement of the bead which in turn facilitated the exploration of extended lateral positions. The maximum lateral forces corresponding to these lateral displacements were $4.5 \pm 0.2 \text{ pN}$ and $6.6 \pm 0.2 \text{ pN}$ for the *SIM* and the *OIM*, respectively.

Already one can see that for the relatively small increase in lateral displacement, there was a large increase in the maximum lateral force. This is in agreement with behaviour predicted by theory, where the force is expected to depart substantially from linearity at large lateral displacements [17]. Specifically, the departure begins to have significance after $0.55 a$, where a is the radius of the bead, corresponding to a lateral position of 553 nm for the bead size used. Therefore, a bead trapped using the *SIM* would only begin to show a departure from the linear force/displacement relationship exactly at or after it reached

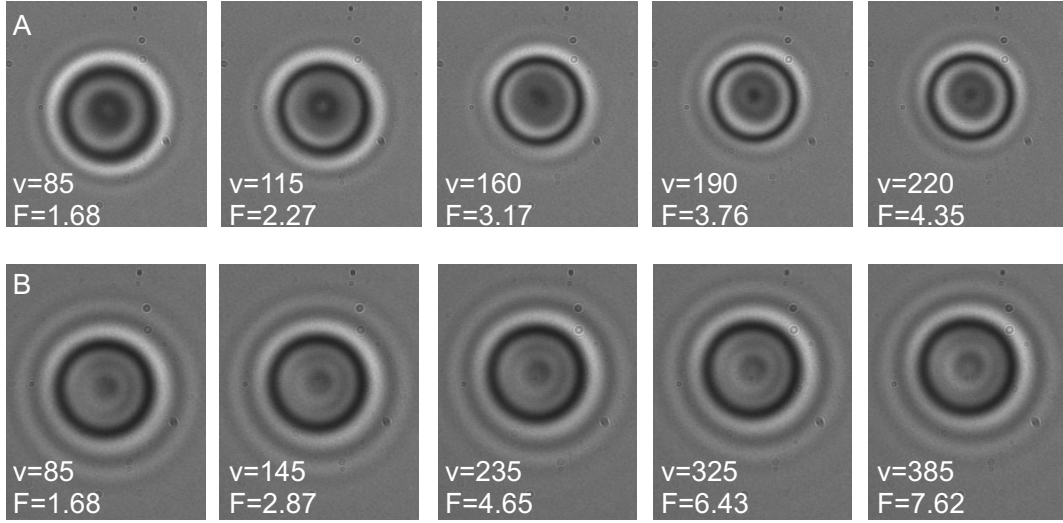


Figure 2.11: CCD camera images of equilibrium bead positions as the drag force, F , is increased; v_{stage} and F are given in units of $\mu\text{m}/\text{second}$ and pN, respectively. Panel A: Standard setup using *SIM*, image diameter decreases with increasing lateral distance. Panel B: improved setup using *OIM*, image diameter remains constant with increasing lateral distance. Both panels show the images of a $2.1 \mu\text{m}$ bead in the trap

the point of escape. In other words, only the *linear region* can be observed when using the *SIM*. This is in total agreement with the findings of both Gong *et al.* and Marendra *et al.* who report, respectively, that the drag force method is completely valid as a method of calibration since the *linear region* is never exceeded but that, because of the assumption that the bead moves in the lateral plane, theory overestimates the maximum lateral force.

A better estimation of the maximum lateral trapping force as well as the relationship between force and displacement after the *linear region* was achieved using the *OIM* because the reduced axial movement of the bead in the trap meant that the bead could be roughly approximated as moving in the lateral plane, creating experimental conditions more like those which the theories were based upon.

A more detailed study was carried out on the lateral trapping force as a function of lateral bead displacement but the $2.1 \mu\text{m}$ beads were chosen instead because of they had a lower standard deviation in their diameter.

2.3.2 Force displacement profile

Figure 2.13 shows the lateral trapping force² as a function of lateral bead displacement. The bead could be moved to a lateral position in the trap that corresponds to $0.74 a$. This was a

²The lateral trapping force was accurately calculated using Equation 1.10 with the input parameters $\eta=0.001 \text{ Pa}\cdot\text{s}$, $a=1.05 \mu\text{m}$ and v_{stage} as the velocity of the stage in $\mu\text{m}/\text{s}$.

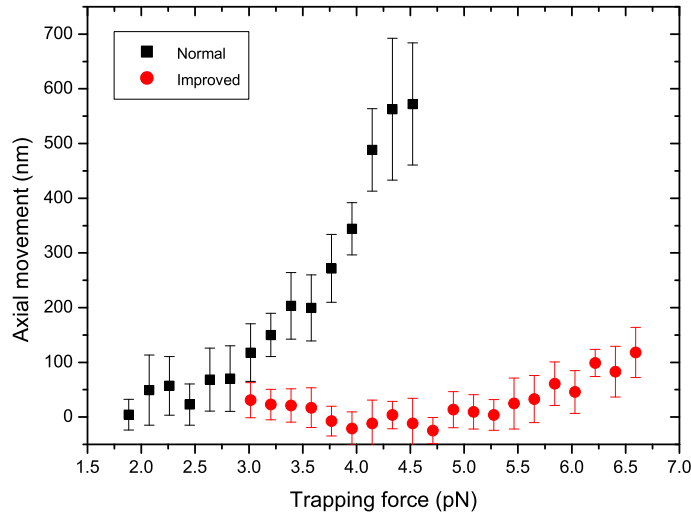


Figure 2.12: The axial displacement of an optically trapped $2.01 \mu\text{m}$ bead is shown as a function of the lateral trapping force. Black squares: *SIM* with significant spherical aberrations at the focus. Red dots: *OIM* where spherical aberrations are eliminated. Each point on the graph represents an average of 10 data points.

considerable improvement with respect to literature, where the furthest lateral distance experimentally explored is $0.6 a$ [16]. Hence, the *OIM* method allowed access to larger lateral regions and enabled the investigation of the lateral trapping potential therein. Data from both positive and negative displacements are shown in order to show the symmetry of the trap. Data from two independent experiments with optical trapping of $2.01 \pm 0.17 \mu\text{m}$ and $2.1 \pm 0.05 \mu\text{m}$ beads using the *OIM*, performed on different days, are shown. Interestingly, the trapping potential is not well described by a single harmonic function. Indeed, the lower part of the potential, until $x \sim 0.55 a$, is well described by a harmonic function. This is in accordance with earlier literature which has only experimentally accessed this region [17, 18, 29]. However, because the bead was forced to extreme lateral positions, with the *OIM*, it was observed that the potential of the trap stiffened.

To quantify the extended optical trapping potential we simply used two harmonic functions to describe the potential:

$$F_{\text{trap}} = \begin{cases} F_{\text{trap1}} = \kappa_1 x & \text{if } |x| < 0.55a \\ F_{\text{trap2}} = \kappa_2 x + \text{constant}, & \text{otherwise} \end{cases} \quad (2.4)$$

Figure 2.13 suggests that the escape force and hence the maximum lateral trapping force is almost the same for the positive and negative sides of the potential. This was supported by a separate set of experiments, briefly mentioned in Section 2.2.3, in which the difference

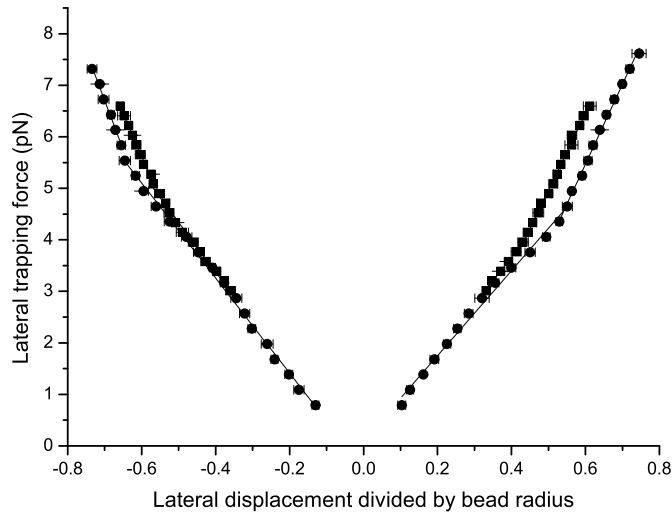


Figure 2.13: Lateral trapping force as a function of lateral displacement for a $2.01 \mu\text{m}$ bead (black squares) and a $2.1 \mu\text{m}$ bead (black dots), in an optical trap. Two independent data sets were taken using the *OIM*, minimising spherical aberrations. Most of the error bars are smaller than the symbols. The full lines are fits to Equations 2.4.

in average escape velocity between the positive and negative displacements was found to differ by no more than 5 percent. By fitting Equations 2.4 to the data shown in Figure 2.13, it was found that $\kappa_1 = 0.0079 \pm 0.0006 \text{ pN/nm}$ and $\kappa_2 = 0.015 \pm 0.002 \text{ pN/nm}$. The values given are averages of the two independent experiments and of the positive and negative sides. The laser power measured at the sample was only 15 mW. This low laser power, and corresponding low spring constant, was chosen because otherwise the trap would be too strong to enable excursions to extreme positions by oscillating the stage at the obtainable velocities.

Calibration of the trap was also performed by observing the *Brownian motion* of the particle [30]. At room temperature, the particle typically only explores the lower part of the potential depicted in Figure 2.13 and hence, this method could only be used to find κ_1 . By employing the equipment described in Section 1.3.1 and the methods described in Section 1.3.2, the value of spring constant determined by PSA was $\kappa_1 = 0.008 \pm 0.0006 \text{ pN/nm}$. This is consistent with the value of κ_1 found by fitting Equation 2.4 to the data obtained from the drag force measurements, within the uncertainty.

The pronounced stiffening of the potential as the bead visited extreme lateral positions had a ratio of $\frac{\kappa_2}{\kappa_1} \simeq 1.8 \pm 0.2$. Many more experiments than those depicted in Figure 2.13 were performed; experiments were repeated over several months and because of occasional modifications to the alignment of the optical trap during this time, it is not so surprising that

the exact values of κ are somewhat different from one experiment to another. However, the appearance of 2 distinct regions that diverge around $0.55a$ both of which are well fitted by a harmonic function showing a stiffening of nearly a factor of 2, consistently prevailed. Experimental conditions were maintained for all experiments and beads from the same batches, with low standard deviation, were used to ensure the repeatability of measurements.

2.4 Size dependency

The significant stiffening observed for the $2.01\ \mu\text{m}$ and $2.1\ \mu\text{m}$ beads is not expected to continue for large bead sizes, where the intensity of the focussed beam is averaged over the bead diameter. Experiments using larger beads have been made but axial equilibrium was broken before the extended lateral positions could be reached [16]. On the other hand, preliminary experiments have shown that there is also a stiffening for $1.65\ \mu\text{m}$ beads but that it is not as pronounced as for the $2\ \mu\text{m}$ beads which were the subject of this investigation. Furthermore, experiments that set out to investigate the same effect using $0.8\ \mu\text{m}$ beads, the most strongly trapped beads for a $1064\ \text{nm}$ laser focussed in water ($\lambda_{\text{water}} = 800\ \text{nm}$), were unsuccessful because the stage could not be moved with high enough velocities to explore the behaviour. The stiffening effect revealed in this work is likely to be of importance for investigations involving beads in the size region $1.5\ \mu\text{m} - 3\ \mu\text{m}$, coinciding with the size regime commonly adopted in experiments with DNA because the beads are large enough to be seen and can be easily combined with suction pipettes.

2.4.1 Role of the side lobes

A possible explanation for the size dependency of the observed stiffening could come from the side lobes of the *Gaussian intensity profile* created upon focussing by the objective. In the case of very low spherical aberrations, the intensity contained in the first side lobe should be small but it may well play a role. The location of the first side lobe is defined as,

$$x = \frac{0.865\lambda}{NA} \quad (2.5)$$

where λ is the wavelength of the trapping laser and NA is the numerical aperture of the objective lens.

Equation 2.5 shows the standard equation for calculating the position of each side lobe. For a laser wavelength of $800\ \text{nm}$ in water and an objective lens with a numerical aperture of 1.32, the first side lobe is located at a position of $524\ \text{nm}$. Figure 2.14 shows how the intensity distribution at the focus should ideally look, taken from reference [31].

The lateral displacements of $780\ \text{nm}$ seen for the $2.1\ \mu\text{m}$ bead would most certainly cause the bead to interact with this side lobe, whether the intensity of the side lobe is large

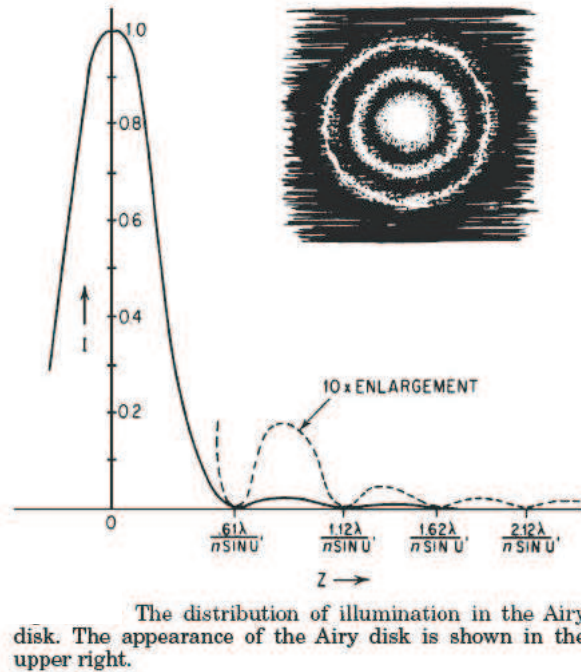


Figure 2.14: A plot of the spatial intensity profile, intensity versus position, is shown with the first side lobe artificially increased by a factor of 10 so that it is more evident.

enough to be solely responsible for the observed stiffening is unclear and is now the subject of a new investigation. However, it would seem reasonable to expect that as the diameter of the bead is reduced, the effect becomes less and less significant before disappearing for beads so small that the side lobe cannot possibly interact with.

One way to investigate this theory may be to position a pinhole just before the back aperture of the objective and repeat the experiments. The pinhole removes some of the intensity from the periphery of the laser spot before it is brought to a focus by the objective lens but without altering the intensity profile. If the observed stiffening reduces as the diameter of the pinhole is reduced then this could be an indication that the side lobes are playing a role. Also if the observed stiffening begins at a larger lateral displacement for smaller beads then this would be an indication that the bead must reach the side lobe before stiffening occurs.

2.5 Summary

Although stiffening of the an optical trap was expected for excursions of the bead to large lateral positions, this had never before been experimentally realised because of a lack of axial stability at extreme lateral positions. By employing a technique for compensation of

spherical aberrations, the extent of the *linear region* of an optical trap was experimentally verified for $2.01\ \mu\text{m}$ and $2.1\ \mu\text{m}$ beads. Furthermore, the force/displacement behaviour out-with this region has been characterised and found to show an additional linear dependency with a stronger spring constant. However, predictions suggested a constantly increasing trap stiffness as a function of lateral displacement, which could be approximated as linear for small displacements (*linear region*, but that should depart sharply from a linear relationship after $0.55a$). In the course of this investigation it was established that the force displacement curve would be better described by two linear functions and that the predictions were neither quantitatively nor qualitatively in agreement with the experimental observations of this study.

In relation to the general goal of investigating cell mechanics within *S.pombe* yeast cells, this finding is probably not as important as it is to studies of DNA because the probe bead for intracellular studies in yeast is of the order of $100\ \text{nm}$ and would probably not be effected by the observed stiffening. The insertion of probes that are suitable for *in vivo* studies of cell division in *S. pombe* is discussed in Chapter 3.

CHAPTER 3

Micro-injection of *S. pombe* yeast cells

The long term goal of investigating the mechanics of cell division *in vivo* is dependent upon the successful insertion of well defined *handles* into the intracellular space of *Schizosaccharomyces pombe* (*S. pombe*), as well as the development of an effective calibration method that can operate within the complex environment of a living cell. The latter is the subject of Chapter 4, while the insertion of nano-probes into *S. pombe* is the topic of discussion in this chapter.

3.1 Background

The role of the cytoskeleton during cell division is both complex and interesting. Positioning of chromosomes, nuclei and mitotic spindle within a cell are mediated by the pushing and pulling forces of polymerising and depolymerising microtubules (MT), along with motor proteins. MT are known to assemble slowly by the addition of individual subunits, whereas their disassembly is much more rapid in the form of 'catastrophe' [32].

Small cells, such as *S. pombe*, are thought to rely predominantly on pushing forces to correctly position the mitotic spindle [33], probably because active positioning in small cells can be achieved without reaching the critical buckling force of a MT [2]. Conversely, larger cells like *C. elegans* may be more reliant on cortical motor proteins to provide pulling forces on the MT organisation centre because of the decreased critical buckling force for long MT [2].

A cell reorganises its contents in preparation for cell division by the complex, cooperative interaction of MT and cytoskeletal motor proteins, the pathways of which are already well understood [34]. However, understanding the mechanism of cell division would be a significant step towards explaining the erratic and uncontrolled cell division that is seen in

cancer cells [35].

Much of the work investigating the properties and behaviour of MT has been carried out *in vitro* because it is much simpler to create the necessary experimental conditions. However, the properties of MT are thought to be significantly different *in vivo*. For example, the persistence length is probably altered substantially by the proteins present in a living cell [35] and the mechanism by which a MT assembles in the presence of MT associated proteins *in vivo* is thought to be far more efficient [2]. Therefore, it is hoped that by investigating the properties of MT *in vivo*, a quantitative value of the relevant intracellular forces can be obtained which would ultimately lead to an improved understanding of the action of a cell under different intracellular conditions.

3.2 Overview

By inserting well defined nano-probes into the intracellular space of *S. pombe*, along with subsequent employment of a calibration method verified in Chapter 4 and, in addition to, the confocal-tweezers system described in Chapter 5, quantitative data on the force exerted by a MT and the dimensions of that microtubule could be simultaneously obtained, *in vivo*. This would facilitate the measurement of properties like the *in vivo* persistence length of a MT, by attaching probes to the fluorescently labelled MT and applying a known force with the optical tweezers.

There are several proven methods to introduce particles into the intracellular environment of cells but, unfortunately, *S. pombe* belongs to a group of cells known as hard wall cells, for which these methods are either ineffective or have very low yields of transfection [36].

P.M. Hansen's Doctorate thesis described a three step method with which to potentially insert gold nano-particles into *S. pombe*, by micro-injection [36]. Steps 1 and 3 of that process, removal of the rigid cell wall and regeneration of the resulting protoplast into a healthy dividing cell, were successfully established [37] and are similarly employed in this investigation which is a continuation of that work. It should also be acknowledged that considerable advancements toward micro-injection of *S. pombe* yeast cells (Step 2) were made prior to this study, in particular the stabilisation of gold colloids so that they were suitable for injection, the production of injection needles of different tip sizes, and optimisation of the injection buffer to maintain stable protoplasts [36].

This chapter briefly summarises the biological system in use and makes an argument for the selection of gold nano-particles as probes. Thereafter, the micro-injection of a membrane impermeable fluorescent dye (Alexa, fluor 488 hydrazide, sodium salt) into protoplasts of *S. pombe* yeast cells is demonstrated in a 'proof of concept' experiment. The micro-injection of gold nano-particles is then discussed as well as a few other methods used to try and insert gold into *S. pombe*. One of which, fusion of gold loaded vesicles, may have particular

advantages over micro-injection in terms of transfection efficiency and throughput but is still in its development infancy.

3.3 Why use *S. pombe*

The fission yeast *Schizosaccharomyces pombe* is the biological system of choice because it is on the same branch of *Eukaryotes* as mammalian cells and has a remarkably similar process of cell division, but with considerably less complexity. For example, the genetic regulatory networks are well described, in comparison to those of human cells, and the sparsity of the cytoskeleton makes it considerably easier to work with. Therefore, it is an excellent choice in terms of a biologically relevant system to compare with human cell function. Furthermore, there are numerous genetically modified strains of *S. pombe* wherein green fluorescent protein (GFP) is incorporated into a wide variety of different organelles, making it an attractive choice for visualisation by confocal microscopy. Some of the GFP expressing strains of *S. pombe* are shown in Figure 3.1.

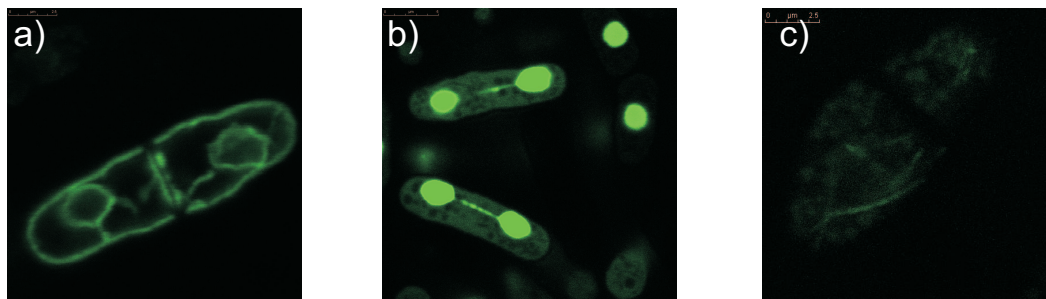


Figure 3.1: A sample of just a few of the GFP expressing strains of *S. pombe* available from our library. The images were acquired using the SP5 confocal system. Images are of *S.pombe* with GFP labelled a) nuclear and plasma membrane, b) nucleus/chromatin region and c) microtubules.

Experiments in which lipid granules were used as naturally occurring probes inside *S. pombe*, to investigate diffusion and viscoelastic properties of the cytoplasm, were previously carried out within the optical tweezers group at The Niels Bohr Institute [38]. The close collaboration established with yeast expert Genevieve Thon during that study is another reason why *S. pombe* is the system in which micro-injection of gold nano-particles is targeted, despite the difficulties caused by *S. pombe*'s size and hard cell wall.

3.4 Micro-injection of *S. pombe*

3.4.1 Preparation of yeast

S. pombe is extremely robust and it is impossible to penetrate by direct micro-injection because of its rigid cell wall [37]. It also lacks any phagocytosis mechanism that would allow natural uptake of a foreign probe. Previous work has ascertained that the best way to attempt micro-injection is to use a three step process of removing the cell wall, micro-injecting and then regenerating the cell wall [36]. The first step involves enzymatic degradation of the cell wall by lyzing enzymes using a previously established protocol, appendix C in reference [36].

Cells were first grown on plates of agarose gel containing glucose, nitrogen, sulphate and aminoacids (without levofloxacin), for approximately 24 hours and at 30 degrees Celsius. Depending on the condition of the cells taken from the previous agar plate, it could take up to 72 hours to see healthy growth on a new plate but in general 24 hours was sufficient. Once a healthy layer of white cells was visible they were transferred to a rich, liquid growth medium (yeast extract 1 per, peptone 2 per, dextrose 2 per, (YPD)) where they could be grown aerobically in a shaking water bath at 30 degrees Celsius. Growth in the YPD liquid medium was phenomenal and care had to be taken to start with roughly the same initial amount of cells so that after 17 hours growth the cells were normally in the most favourable condition.

To start with, the cells divide as quick as possible in liquid media because there is a rich environment of nutrients. Therefore, they are individually quite small and less suitable for micro-injection. If, on the other hand, they were grown to the point where the growth medium only just began to get depleted of nutrients (~17 hours) then they became larger in size and were most suitable point for protoplast creation and subsequent micro-injection, so called log phase [36]. This was the point at which they were harvested. However, if they were grown for too long then the growth medium became overcrowded and the waste products built up such that the yeast cells changed to another phase (stationary phase [36]) in which the lyzing enzymes, used to remove the cell wall, no longer functioned properly and the transformation frequency dropped considerably below 100 percent.

Correctly harvested cells were spun down (5000 rev/min, 5 min), removed from the YPD growth medium and re-suspended in E-buffer containing 50 mM Sodium Citrate, 100 mM Sodium Phosphate (pH = 5.7) and 0.9 M sorbitol to balance the osmolarity. Thereafter, 15-20 mg/ml of the lyzing enzyme (lysozyme, Novozymes) was added and the sample placed on a rotating wheel for 50 minutes at room temperature. This is almost identical to the process described in appendix C of P.M.Hansens thesis [36]. Using this method gives an almost 100 percent protoplast formation efficiency. Protoplasts or spheroplasts are the spherical vesicles that result from the removal of the cell wall from *S. pombe* yeast cells. They contain

all the biological material of the cell and are basically just cells without the cell wall. The time lapsed images of forming protoplasts are shown in Figure 3.2, Figure 4.3 in reference [36].

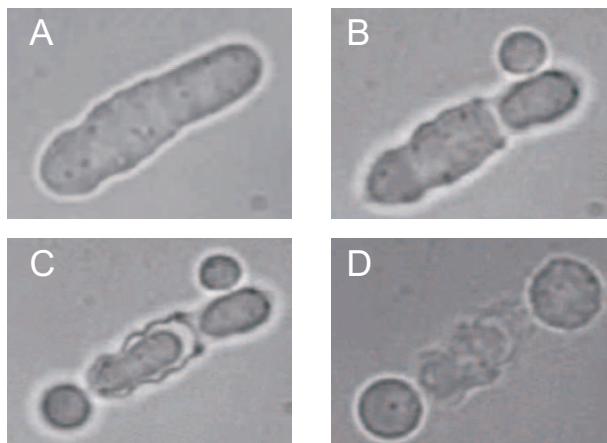


Figure 3.2: Time lapsed images of the enzymatic degradation of the cell wall of *S. pombe* fission yeast. A) No visible effect on the cell after 5 min. B) After ~ 10 min a protoplast forms through a hole in the rigid cell wall, the huge internal pressure is the driving force behind the protoplast formation. C) After ~ 15 min a second protoplast forms because this cell was in the process of dividing before being removed from the growth medium. D) After ~ 20 mins the two protoplasts are fully formed for this particular cell.

The exact time it takes for a protoplast to form varies and was dependent on the condition of the cell before growth was halted as well as the enzyme concentration. The higher the concentration of enzymes, the faster protoplasts formed. Another interesting aspect of protoplast formation was the position at which the cell wall failed and a protoplast popped out. This became part of a small investigation for three first year students whom I supervised but the findings were rather inconclusive. *S. pombe* yeast cells are cylinder like in shape with hemispherical caps; the hypothesis was that protoplasts often emerge at the point of singularity between the two shapes making up the cell wall. However, the result of analysing images of the emergence position of around 100 protoplasts was that almost half of the protoplasts formed at the poles and only a moderate 25 percent lay in a roughly Gaussian distribution around the singularity point. It was hard to make any solid conclusions from such a small data set but a strong emergence at the poles may be explained by the thinness of the cell wall at the poles during growth.

Finally, the resulting protoplasts are gently centrifuged (2000 rev/min, 3 min) and again re-suspended in E-buffer but this time with the addition of 25 mM CaCl_2 to aid membrane sealing after micro-injection [36].

The key difference in this study is that the protoplasts were left in this Calcium rich E-buffer for at least 2 hours before micro-injection was first attempted. Previously, micro-

injection had only been attempted in the first 30 minutes after transferring protoplasts to a calcium enriched E-buffer because after which they were judged to be too unstable[36].

3.4.2 Selection of a probe

Most recently, the discovery that quantum dots can be trapped [39] has provided another possible candidate for an *in vivo* probe but there is still some uncertainty in the regularity of the diameter, sphericity and toxicity of such probes. The latter of which has been somewhat addressed by encapsulation in micelles [40] and should the remaining aspects be remedied, QDs would have the advantage over other probes that they are highly visible and do not bleach over time.

During the course of his Doctorate, Poul Martin Hansen established that gold nanoparticles make for the most favourable choice of probe because they: are chemically inert, can be reliably produced as spheres with low standard deviations in diameter (BBI, international), can be easily functionalised by the use of Thiol end groups which attach strongly to gold, are sufficiently small that they can move around easily through the crowded intracellular environment, and can be optically trapped with forces in the tens of pico Newton range[28, 36].

More conventional probes like polystyrene and silica spheres are unsuitable for such *in vivo* research because their size would cause major disruption to the cytoskeleton network of actin filaments and microtubules. Furthermore, the maximum force applicable to a polystyrene bead reduces as its diameter falls below $0.8 \mu\text{m}$ (for trapping laser light of $\lambda \sim 1.064 \mu\text{m}$ in air). In comparison, gold offers significantly higher forces for a similarly sized particle but the proposed heating, predicted to arise when trapping gold nanoparticles at high laser powers [11], could potentially decrease the attractiveness of using these as probes to investigate the micro-rheology of the cell. However, experience within the group suggests that single beads of size 80 nm are not elevated to temperatures where the surrounding medium significantly changes temperature for those laser powers used in trapping. An experimental investigation to ascertain the physical heating effect is currently underway to compare with the $266 \text{ }^\circ\text{C}/\text{W}$ predicted [11].

Naturally occurring probes, such as lipid granules used to investigate the diffusive properties of the cytoplasm in a previous investigation [38], can also be trapped and have the added benefit that they are native to the cell. However, they vary somewhat in diameter which makes calibration and quantitative force measurement impossible. Gold is thus the best fitting solution for now.

3.4.3 Micro-injection

Production and preparation of micro-injectors and suction pipettes

In order to micro-inject, one needs to produce suitable micro-injectors with appropriate tip sizes and taper lengths. This was done according to the guidelines laid out in appendix D of a previous study [36]. Borosilicate thin walled micropipettes with filament (World Precision Instruments) and a large ratio of inner to outer diameter (ID. 0.78 mm, OD. 1 mm) were used to decrease the probability of aggregation of injection material within the micropipette. The micropipette puller (Flaming/Brown) was used to produce the micro-injectors using the following settings: *pressure* - 300, *heat* - 630, *pull* - 80, *velocity* - 100 and *time* - 200. This repeatedly gave micro-injectors with tip sizes of ~ 300 -400 nm and long gradual tapers down to the tip which better avoids aggregation than a short steep taper.

Before micro-injecting, the tip of the injector was placed into a solution containing a high concentration of BSA (30 mg/ml Bovine serum albumin dissolved in millipore water) so as to coat the tip with the polymer in a bid to prevent aggregation of the injection material at the tip. Prior to this, the BSA solution had been centrifuged at high speed (13,000 rev/min) for 30 minutes and the upper half of the solution removed and kept for the tip coating. This ensured that any large aggregates of BSA would not be present in the coating in or around the tip of the injector.

The injection material was then inserted into the injector from the rear, using the capillary forces to carry the injection material to the tip. Finally the injector was backfilled using a metal syringe containing filtered millipore water before it was connected to the pressure applicator (Eppendorf, CellTram).

Suction pipettes were created using the same micropipette puller used to make micro-injectors but with different production settings and with less stringent requirements on the inner and outer diameters of the micropipettes themselves. Standard micropipettes (ID. 0.5 mm, OD. 1 mm, World Precision Instruments) were sufficient and were pulled with pull settings: *pressure* - 532, *heat* - 675, *pull* - 110, *velocity* - 100, *time* - 250. The suction pipettes produced have long thin tapers so that thereafter, they could be further melted (from the tip back) to accurately obtain the desired tip diameter. Micropipettes with tip diameters of $\sim 5 \mu\text{m}$ were produced because this is approximately half the radius of a protoplast and allows the protoplast to be comfortably held in the suction pipette during the micro-injection process.

The suction pipette was backfilled with millipore water before it was mounted on the sample. Mounting was done in such a way that the flexible end section lay along the sample surface.

Preparation of gold nano-particles

Preparation of gold nano-particles was made in roughly the same manner as the stabilisation procedure reported by P.M. Hansen[36]. 500 μl of gold particle solution (typically 80 nm suspension, British Biocell International) was transferred to an Eppendorf tube and centrifuged for 5 minutes at 5000 rev/min. The gold was then re-suspended in millipore water and sonicated for 15 minutes before filtration (200 nm pore size, Eppendorf). Thereafter, 40 μl of a stock solution of thiolated polyethylene glycol (PEG, 5000 Dalton, Aldrich Sigma, 4 mg/ml) was added to the remaining gold particle solution ($\sim 400 \mu\text{l}$ after filtration) so that the final concentration of PEG was 0.4 mg/ml. Gold nano-particles were thus stable for use in micro-injection experiments where the injection buffer contained moderate levels of mono and divalent salts.

Micro-injection procedure

In the first 30 minutes of being transferred to the E-buffer with 25 mM Calcium Chloride, the protoplasts began adjusting to the new buffer conditions and they were very viscous and did not resist the tip of the micro-injection needle but rather deformed around it. Therefore, it was very difficult to rupture them and they could be termed as more stable. However, it was also incredibly difficult to penetrate them when they were like this because one needed to actively hold them in the suction pipette, so that some of the slack in the membrane was taken up, and then drive the injector into them. Almost always, this technique was unsuccessful. Then after around 30 minutes, the protoplasts became more elastic and were only slightly deformed by the tip of the injector. As was previously reported, they inevitably always burst under the act of micro-injection during this period [36]. This may have been because the membrane failed to seal after rupture by injection, or that the balancing of inside and outside osmolarity could not withstand the introduction of an additional volume during that critical time period. Whatever the reason, if one simply waited a further one and a half hours, or even 2, the protoplasts became a lot more manageable and although still fragile to work with, repeated micro-injection was possible. This is the key difference to the injection procedure suggested previously [36].

The principle of micro-injection is shown schematically in Figure 3.3.

Injection materials included 80 nm gold nano-particles, quantum dots and a membrane impermeable dye (Alexa fluor 488 hydrazide, sodium salt). Micro-injection of gold nano-particles has proven rather difficult because they had a tendency to aggregate even at moderate salt concentrations. This problem was partially alleviated by coating the gold colloids with thiolated polyethylene glycol (PEG, 5000 Dalton, Aldrich Sigma, final concentration 0.4 mg/ml) [36] which prevented them from sticking together. Albeit, they still adhered to glass surfaces such as the micro-injection needle which over time led to blockages of the micro-injector and set a finite time for which each injector could be used before it

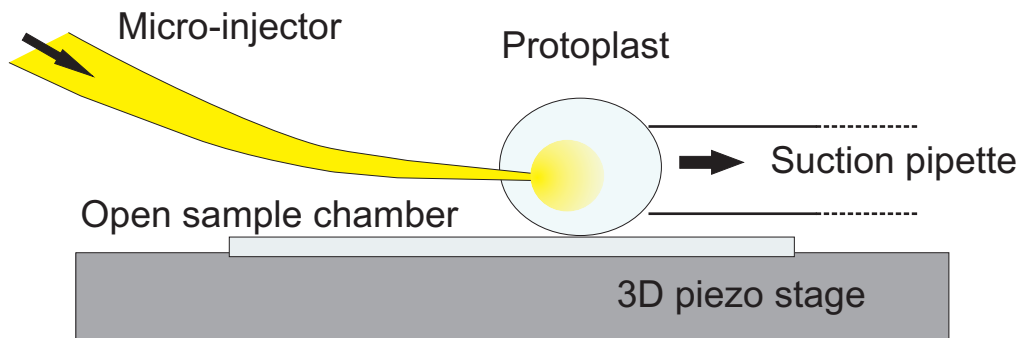


Figure 3.3: A protoplast is firmly held in position by a suction pipette, clamped on or close to the sample surface. The sample is mounted on a piezoelectric stage with accurate positional movement in three dimensions (P-731.20). The micro-injector is lowered to within a few microns of the surface and a small forward pressure is then applied by a pressure applicator (Eppendorf CellTram) so that the injection material begins to flow from the injector tip. The piezoelectric stage is then used to manipulate the protoplast into position and jab the protoplast into the micro-injector.

had to be replaced (~ 20 min).

If the flow of gold was maintained at a steady rate, blockage events occurred much less frequently than if a slow flow was employed. This is, however, counterproductive to micro-injection wherein the injected volume should remain small with respect to the volume of the protoplast, or else the protoplast simply explodes. A suggestion to overcome this problem was made in a previous investigation [36]. By increasing the concentration of gold nano-particles, a smaller injected volume could be delivered while the number of gold nano-particles transferred could be maintained. However, increasing the concentration of gold also increased the regularity of blockage events and resulted in there never being more than a few minutes where a clean well functioning injector was available with which to micro-inject.

Although efforts to micro-inject gold into *S. pombe* yeast cells are still ongoing, the possibility of moving to larger cells should be considered since this would relieve a lot of the current constraints in the experimental procedure. For example, this would allow the size of the injector tip to be increased which would considerably alleviate the problem of aggregation. Furthermore, moving to a larger cell would allow insertion of a larger volume and relax the need to very accurately control the flow.

There is also the problem of visualisation which will remain no matter what size cell one chooses to employ. Gold particles regularly attached themselves to the outer membrane of the protoplast making it difficult to determine immediately whether gold colloids were inside or simply attached at the surface. Only by making a three dimensional confocal scan was it possible to determine if an attempted micro-injection had been successful or not. Given the time constraints already placed on the procedure by the lifetime of the injector,

this became impractical.

Therefore, before investing more time on challenging experiments to inject gold nanoparticles, a simple 'proof of concept' experiment was devised to demonstrate whether protoplasts of *S. pombe* could actually be injected by this procedure. Employing a membrane impermeable dye meant that the only way fluorescent molecules could enter a protoplast was if they were micro-injected. If the membrane impermeable dye molecules were injected, the entire protoplast would light up making for a simple and effective verification of volume transfer. Conversely, if the injection was unsuccessful, the dye molecules would quickly diffuse away from the focal volume because, unlike the gold nano-particles, they do not attach to the outer membrane of the protoplast. This experimental configuration was considerably simpler than injecting gold particles because it avoided problems of aggregation and time consuming confocal visualisation. Over ten separate successful micro-injection events were made using this procedure and a sequence of still images from one of them is shown in Figure 3.4.

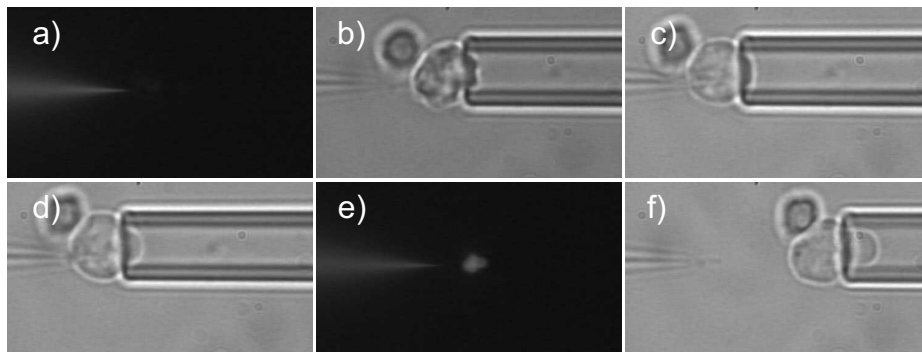


Figure 3.4: The micro-injection of a protoplast with a membrane impermeable dye (Alexa fluor 488 hydrazide, sodium salt) is shown by time lapsed images. a) A fluorescent view of the experimental conditions before micro-injection began, only the micro-injection needle can be seen to fluoresce. b) The same situation as a) but as seen in bright field, notice the undulations in the membrane. c) The first injection event, observe how the additional slack in the membrane from b) has now been taken up due by the newly injected volume. d) A second injection of the same protoplast resulting in a greater tension in the outer membrane and a marked increase in protoplast volume. e) A view of the injected protoplast in fluorescence mode, the dye is clearly contained inside the protoplast which demonstrates that the dye has been injected but also that the membrane has resealed. f) A bright field view of the protoplast after two successful micro-injection events, the membrane is clearly still intact.

The micro-injection of *S. pombe* with simple dye molecules demonstrates that there is merit in this procedure and that, in principle, gold nano-particles could also be inserted into the intracellular medium of *S. pombe*. Although before doing so, one should also verify that the injected protoplast can be returned to a healthy dividing yeast cell with cell wall.

3.4.4 Regeneration

P.M.Hansen showed that *S. pombe* yeast cells stripped of their cell walls could be efficiently transformed back into healthy dividing cells again [36], but those were not cells which had been stored in a buffer containing 25 mM Calcium Chloride for three hours and repeatedly pumped full of dye molecules. One expects that micro-injected protoplasts will regenerate into healthy dividing cells in much the same way that non-injected protoplasts did, but this must be confirmed.

The first step towards verifying this has already been achieved by employing the same regeneration procedure previously reported [36]; protoplasts that had spent 3 hours in the injection buffer were centrifuged (2000 rev/min) and transferred to a regeneration medium (YPD with 1.2 M E-sorbitol). The purpose of the sorbitol was to replicate the osmotic conditions of the injection buffer until the cell wall developed around the protoplast. These protoplasts were found to regenerate with almost 100 percent efficiency after a period of 20 hours. However, no time lapsed images of the regeneration process were made. Protoplasts were simply transferred to an eppendorf tube and left to regenerate in the regeneration medium overnight.

Experiments to regenerate micro-injected protoplasts into dividing cells have not yet been made because there are several technical challenges which must first be overcome. The simplest way to transfer protoplasts from the injection buffer to the regeneration medium is by centrifugation but this involves removing the micro-injected protoplast from the microscope, making it difficult to locate again afterwards because there are typically only 3 or 4 injected protoplasts from a sample of thousands.

Therefore, it is easier if the protoplast remains *in situ* so that regeneration can be followed by time lapsed microscopy. Instead of centrifugation, one must devise some method of exchanging the buffer without losing sight of the injected protoplast. In addition, micro-injection takes place in an open chamber and during the many hours it takes to observe the regeneration of a protoplast into a dividing cell (~17 hours), the sample can often dry out. Thus there should also be a way of closing the chamber after micro-injection. Although, this may also be problematic since protoplasts regenerated in Eppendorf tubes were observed to blow open because of the gaseous waste products which built up.

All things considered, micro-injection is an extremely labour intensive, slow and cumbersome method of attempting to insert gold nano-particles into *S. pombe*. Even if the problems of aggregation are overcome and gold is successfully introduced into the cytosol of *S. pombe* protoplasts, the absolute best one can hope for is to have 5-10 regenerated cells with gold inside after one week's worth of laboratory work. The throughput of useable cells for time invested is simply too inefficient for micro-injection to be a viable option of producing cells containing gold nano-particles. Particularly, when one considers the number of data points required to extract reliable, quantitative information about a biological process

[41].

This led to the exploration of other methods of particle transfer that were compatible with protoplasts of *S. pombe*.

3.5 Alternative methods of probe transfer to *S.pombe*

3.5.1 Simple lipid assisted micro-injection (SLAM)

This was only very briefly tried and in those initial experiments there were problems establishing a channel between the pipette and protoplast. Lack of time and success in other experimental investigations meant that this method was never fully explored and is definitely worth some further investigation. It is another micro-injection based technique which begs the question; what makes this technique any more attractive than the procedure ruled out in the last section?

Simple lipid assisted micro-injection (SLAM) [42] has the advantage that the tip of the micro-injector is physically fused to the target cell, providing a stable pathway between injector and cell. The tip of the injector is coated with lipids that fuse to the membrane within seconds of contact and thereby facilitates a very controlled transfer of volume into the protoplast while also preventing the injection buffer from entering the pipette. It has also been demonstrated that the SLAM micropipettes can be reused a number of times which would allow micro-injection of multiple protoplasts in one experimental attempt [42]. Furthermore, because of the way in which the pipette fuses to a cell, the tip size can be made larger than for standard micro-injection which may reduce the number of aggregation events.

However, by far the most exciting advantage of this technique is that one could potentially remove the need to make suction pipettes or complicated chambers mounting suction pipettes by simply employing the laser to trap protoplasts and press them gently against the micro-injector. One can envisage the situation where the injector could be positioned anywhere in the sample and the laser tweezers bring the protoplast to the injector, contact for around 10 seconds while gold nano-particles are transferred, and then onto trapping the next protoplast. If the whole thing were computer controlled then the throughput of transfected cells were up into hundreds per hour, then investigating the nano-mechanics and micro-rheology of cell division in *S. pombe* would not seem so unrealistic.

3.5.2 Vesicle fusion

Another method with the potential to quickly create a large number of protoplasts with gold nano-particles inside is vesicle fusion. Fusing vesicles loaded with gold nano-particles together with *S. pombe* protoplasts is a more extreme method than SLAM because the entire contents of the vesicle enters the intracellular space and the 'foreign lipids' of the vesicle

may considerably alter the lipid composition of the cell membrane. SLAM only involves the fusion of a small amount of foreign lipids with the membrane which is not thought to be harmful to the cell. Furthermore, the transfer of foreign volume to the cytosol is low for SLAM compared to fusion with a vesicle. Nonetheless, experiments to create giant unilamellar vesicles (GUVs) with a high concentration of gold nano-particles inside were undertaken.

Lipids (DMPC/DPPC, 50:50 molar ratio) were applied to indium tin oxide (ITO) transparent electrodes using Trifluoroethanol (TFE) to help the lipids spread out and create a uniform lipid coating on the surface of the electrodes. The electrodes were then placed in the desiccator to dry out over night. Gold nano-particles were prepared as described in Section 3.4.3 and sealed in a chamber between the two electrodes. Thereafter, vesicles were formed by electroformation in the highly concentrated solution of gold nano-particles. The vesicles produced had a considerable range of diameters, many of which were on the order of 30-40 μm diameter. Considering that the diameter of a typical protoplast is around 10 μm , these vesicles were not ideally suited for fusion with protoplasts but the hope is that a protocol can be found to produce vesicles on the order of 5-10 μm diameter which would be suitable for fusion experiments. Figure 3.5 shows one of the vesicles formed, 20-30 μm in diameter, containing a large number of 80 nm gold nano-particles.

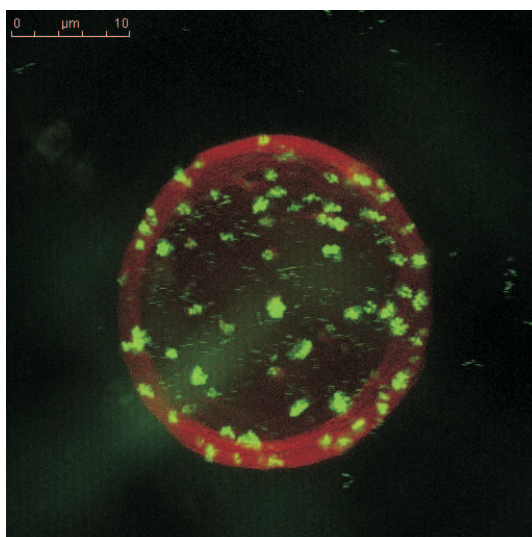


Figure 3.5: The fluorescent dye (DiIC18, invitrogen) incorporated into the membrane of the vesicle is shown in red even though in reality it fluoresced green. Similarly, gold nano-particles appear green despite the fact that they were actually visualised using the reflection of a 633 nm Helium neon laser. Many gold nano-particles were contained within the vesicle which was more obvious from 3D confocal images.

The idea is that if vesicles such as that shown in Figure 3.5 can be made with more

appropriate diameters, they could then be mixed with protoplasts and placed into a fusion chamber. A fusion chamber is basically a special electrically insulated chamber (Eppendorf) with two electrodes on the surface. Applying an alternating current across the electrodes causes the vesicles between the two electrodes to line up. When a high voltage d.c. pulse is subsequently applied, any two vesicles that are in contact and are between the two electrodes fuse together [43]. Of course, potential problems are that there will also be protoplasts which fuse to protoplasts and vesicles which fuse to vesicles but this configuration could potentially facilitate the transfection of many protoplasts using one pulse, a few milliseconds in duration.

3.6 Summary

The micro-injection of *S. pombe* with suitable probes for *in vivo* force measurements or the application of prescribed forces inside the cell was difficult. Micro-injection of these cells was proven possible by means of a membrane impermeable dye but, as of yet, insertion of gold nano-particles has been elusive. Most of the problems arise from the general size and fragility of the *S. pombe* cells and perhaps larger cells should be considered. The alternative is to investigate the possibility of a more robust and controlled method of probe insertion that one way or another makes use of the fusion lipids with these protoplasts.

In the event that gold particles are inserted into *S. pombe* or instead into a larger cell, a valid calibration method would be required in order to make any quantitative force measurements. The calibration of optical tweezers in viscoelastic media is considered in Chapter 4.

CHAPTER 4

Calibration of optical tweezers in complex viscoelastic media

4.1 Overview

The ultimate goal of this research is to make quantitative measurements of cellular processes *in vivo*, such as cell division, so that a better understanding of how a living cell actually functions can be obtained. An immense amount of information about biological processes has already been gathered *in vitro*, using optical tweezers as the tool to investigate the time and velocity dependence of forces exerted by bio-molecules [29, 44, 45]. The interactions of numerous bio-molecules, such as motor proteins, have been thoroughly investigated *in vitro* [1, 46] but in order to understand the complex intracellular processes that occur when these bio-molecules come together in the natural environment of the cytoplasm, their *in vivo* behaviour must first be examined and compared with the behaviour reported *in vitro*. Forces exerted by bio-molecules *in vivo* will inevitably differ slightly from those seen in *in vitro* because the majority of bio-molecules will be carrying out their natural biological function during *in vivo* experiments.

So far, investigating the complex biological functions of molecules within the cytoplasm has been restricted by the absence of a reliable and proven calibration method. In order to realise the full potential of any data obtained from *in vivo* experiments, or to exert prescribed forces *in vivo*, one needs to be able to separate the force contribution of the tweezers from the contribution of the intracellular environment.

Standard calibration techniques like the power spectrum method, Section 1.3.2, rely upon the application of a known force on a trapped particle and the measurement of the resulting particle position to determine the spring constant of the trap, κ , and the position of the particle, x , within the trap. This *passive* method of calibration, in which the *Brownian motion* of the particle is the known driving force used to displace the particle in the trap, is

only accurate when the trapped particle is considered to be moving within a simple viscous fluid.

However, the cytoplasm can be considered, to a first approximation, as a viscoelastic medium. Therefore, calibration by power spectral analysis (PSA) becomes invalid when used in the cytoplasm because it is based on the assumption that a bead is trapped in a purely viscous fluid. The power spectra of beads in an actin gel [47] or of lipid granules in a cell [38] can be seen to deviate qualitatively from the power spectra of beads in water or glycerol [48] and although calibration by power spectral analysis (PSA) can be used to obtain information about e.g. diffusional properties of a particle in a viscoelastic medium [38], it cannot be used to obtain measurements of forces. Furthermore, many properties of the cytoplasm remain unknown or even change with position in the cell which means a new *in situ* calibration method is required if quantitative forces are to be measured *in vivo*.

This chapter deals with the experimental verification of a recently proposed method for *in situ* calibration in viscoelastic media [3], wherein knowledge of the viscoelastic properties of the medium is not a prerequisite. The essential details of the postulated calibration method [3, 49] are briefly discussed before the experimental procedure with which calibration was made is comprehensively presented. Thereafter, the authenticity of this *in situ* calibration procedure is verified both in water and in a network of entangled F-actin by comparing the measured spring constant with the value obtained by PSA, and by comparing the experimentally determined value of shear modulus (obtained by further analysis of the measured data) with that reported in bulk rheology experiments [50], respectively. This work was a collaboration with Mario Fischer, Kirstine Berg Sørensen and S. Nader S. Reihani.

4.2 Brief theoretical introduction

4.2.1 The Fluctuation dissipation theorem (FDT) calibration method

The fluctuation dissipation theorem (FDT) is derived on the assumption that the response of a system in thermodynamic equilibrium to a small external perturbation, is the same as its response to a spontaneous fluctuation. The proposed *in situ* calibration method (FDT method) [3] suggests that both active and passive measurements be made on the system with the assumption that the FDT is valid during the active driving of the sample because any perturbations to the system are suitably small. The original presentation of this method suggested two possible forms of active driving; active stage driving or oscillation of the trap itself by acousto-optic modulation (AOM), laser driving [3]. However, only active stage driving is discussed in this study since this was the active driving method used to experimentally investigate the authenticity of the FDT method as an accurate calibration process.

The following summary of the FDT method is the same as that described in [51] and is a condensed version of the original publication [3].

The standard calibration equation for optical tweezers in purely viscous media is shown in Equation 4.1 and is presented as a convenient formulation of the FDT.

$$P(\omega) := \lim \frac{\langle |\tilde{x}(\omega)|^2 \rangle}{T_{\text{meas}}}, \quad (4.1)$$

where $\tilde{x}(\omega)$ is the Fourier transform of the particle trajectory $x(t)$, observed for time T_{meas} and ω relates to f through $\omega = 2\pi f$.

In viscoelastic media, the power spectrum is given analytically as:

$$P(\omega) = \frac{2k_B T \Re\{\tilde{\gamma}(\omega)\}}{|\kappa + i\omega\tilde{\gamma}(\omega) - \omega^2 m|^2}, \quad (4.2)$$

where m is the mass of the trapped particle, κ is the spring constant of the optical trap and $\tilde{\gamma}(\omega)$ is the *friction retardation spectrum*. The *friction retardation spectrum* describes the interaction of a trapped particle with its surrounding medium, the real part represents dissipative processes and the imaginary part encompasses the elastic processes. For each frequency, ω , Equation 4.2 provides one equation with three unknown parameters, κ , $\tilde{\gamma}(\omega)$ and m . Therefore, the FDT method [3] suggests that the system be actively driven in order to obtain the additional information required to solve for these three unknown parameters, provided the FDT is valid under experimental conditions of active driving. i.e. that the active measurement is no more than a perturbation from the equilibrium condition.

The *response function* describes non-equilibrium systems in linear response theory.

$$\chi''(\omega) = -\frac{\omega}{2k_B T} P(\omega), \quad (4.3)$$

where $\chi''(\omega)$ is the imaginary part of the *response function*, or the inverse effective spring constant if one considers that the *response function* relates external forces, $\tilde{F}_{\text{ext}}(\omega)$, to average positions through:

$$\langle \tilde{x}(\omega) \rangle = \chi(\omega) \tilde{F}_{\text{ext}}(\omega). \quad (4.4)$$

The case of stage driving

The simplest method of perturbing the system is by actively driving the piezoelectric stage upon which the sample is fixed, assuming that the sample is a closed chamber for which the surrounding medium moves in unison with the stage. This permits reformulation of the *response function* as:

$$\chi''(\omega) = -\frac{\omega}{\kappa - \omega^2 m} \Re\{\tilde{R}_{\text{stage}}(\omega)\}, \quad (4.5)$$

and where $\tilde{R}_{\text{stage}}(\omega) = \tilde{\gamma}(\omega)\chi(\omega)$, one can obtain the equivalent of Equation 4.3,

$$(\kappa - \omega^2 m)_\omega = \frac{2k_B T}{P(\omega)} \Re\{\tilde{R}_{\text{stage}}(\omega)\}, \quad (4.6)$$

where $P(\omega)$ represents the power spectrum of the unperturbed system (determined by passive measurements). The active spectrum for stage driving, $\tilde{R}_{\text{stage}}(\omega)$, is the ratio of the Fourier transform of the average trajectory of the trapped particle, $\langle \tilde{x}(\omega) \rangle$, to the Fourier transform of the velocity of the stage. The stage moves with a predetermined trajectory, $x_{\text{stage}}(t)$, that is infinitesimal around $x_{\text{stage}} = 0$ to provide the external perturbation:

$$\tilde{R}_{\text{stage}}(\omega) := \frac{\langle \tilde{x}(\omega) \rangle}{i\omega \tilde{x}_{\text{stage}}(\omega)}. \quad (4.7)$$

Sinusoidal stage driving

The conclusions made from simulations [3] were that the most reliable method of perturbing the system is to use harmonic oscillations. For a sinusoidally driven stage, where $x_{\text{stage}}(t) = A_{\text{stage}} \sin(\omega_{\text{stage}} t + \phi_{\text{stage}})$, the trapped particle responds to sinusoidal motion as $\langle x_{\text{particle}}(t) \rangle = A_{\text{particle}} \sin(\omega_{\text{stage}} t + \phi_{\text{particle}})$. Equation 4.6 then becomes:

$$(\kappa - \omega^2 m)_{\omega_{\text{stage}}} = \frac{2k_B T}{P(\omega_{\text{stage}})} \frac{A_{\text{particle}}}{\omega_{\text{stage}} A_{\text{stage}}} \sin(\Delta\phi), \quad (4.8)$$

where $\Delta\phi$ is the phase lag between stage and particle oscillations ($\Delta\phi = \phi_{\text{stage}} - \phi_{\text{particle}}$). One now has a simple expression with which to determine the trap stiffness, κ , since all the values on the right hand side of Equation 4.8 can be found by experiment.

4.2.2 Selecting the appropriate amplitude and frequency of stage driving

For a reliable calibration result the stage should be driven at a number of different driving frequencies to reduce the statistical error and allow fitting for the mass of the trapped particle (For light particles m can be neglected). However most importantly, systematic errors that are present at certain frequencies can be located by this method. Bio-active processes are thought to render the FDT invalid at specific frequencies [49] which becomes relevant if this technique is to be used as a an *in vivo* calibration method.

The frequency range should be as wide as possible and is restricted only by the limitations of the equipment, in this case the performance of the piezoelectric stage (Physik instrumente, P-517.3CL). The corresponding amplitude for each oscillation frequency requires careful consideration; the validity of the FDT must be maintained, only small perturbations of the equilibrium system are permitted, and the linear region of the trap must not be exceeded. The graph in Figure 4.1 provides a good rule of thumb for finding the

driving amplitude for each oscillation frequency because it shows the stage amplitude necessary to cause a particle to oscillate with an amplitude equal to the half width of the trap, $(k_B T / \kappa)^{1/2}$, thereby insuring that the response of the system is linear.

Estimation of required stage amplitudes for active part of force calibration in actin

$A_S^2 = (1 + \omega_c^2 / \omega^2) * A_B^2$ with A_B being equal to the half width of the trap $(k_B T / \kappa)^{1/2}$; parameters: $R = 0.825 \mu\text{m}$, $\eta = 0.0009, 0.009, 0.09 \text{ Pa}\cdot\text{s}$

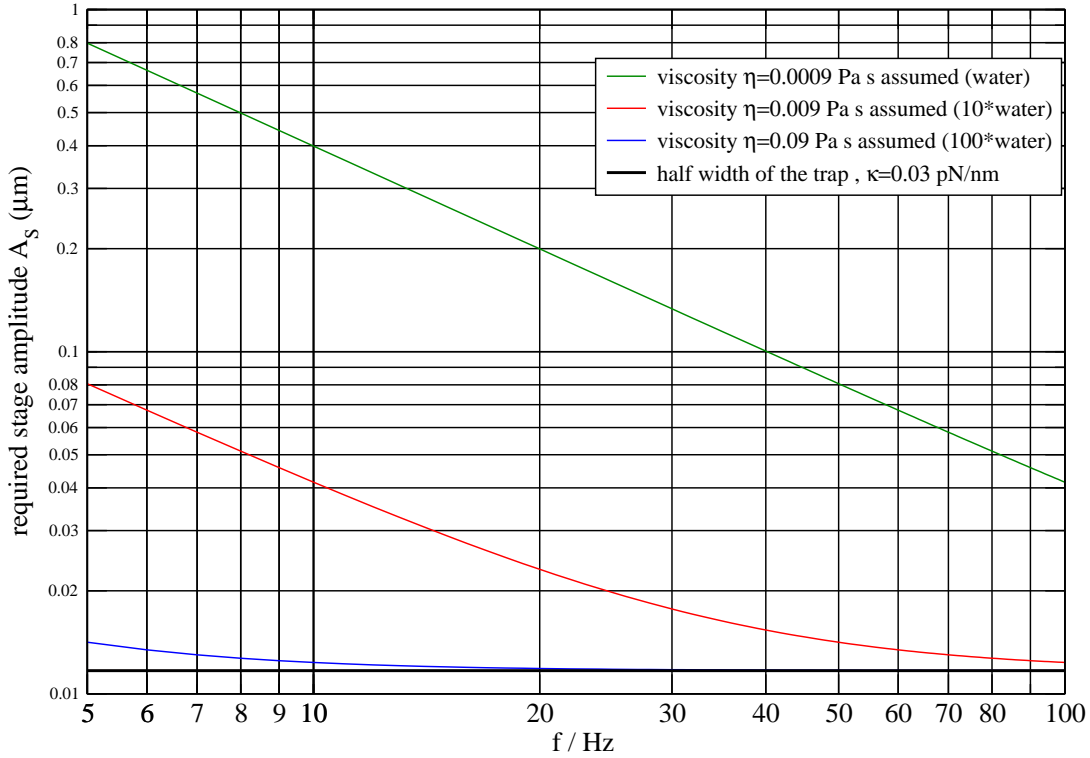


Figure 4.1: The plot shows the stage amplitude necessary to cause a trapped particle to oscillate with an amplitude equal to half the width of the trap vs stage oscillation frequency. The green curve shows the suggested stage amplitudes for experiments made in water while the red and blue curves show the suggested stage amplitudes for media with viscosities of 10 times water and 100 times water, respectively. Figure taken from the PhD dissertation of M. Fischer.

The driving amplitudes selected for calibration in water follow the green curve while the driving amplitudes in entangled F-actin were never lower than 200 nm because of the stage limitations at high driving frequencies.

4.3 Experimental procedure

The experimental procedure for calibrating optical tweezers in viscoelastic media consisted of five separate measurement steps. The first two processes involved active and passive measurements on the system, wherein the data necessary to determine the spring constant, κ , of the trap was gathered. The remaining three steps were necessary to calibrate the

equipment used in the active and passive measurements so that meaningful data could be extracted from the voltage signals measured in the active and passive experiments.

The experimental setup used in this study was identical to that employed to investigate the extremes of the optical trapping potential, see Section 2.2.1. Positional detection of the trapped particle by quadrant photodiode (QPD) was employed during the passive and active parts of the experiments while detection by both QPD (Hamamatsu, S5981) and CCD camera (Sony, XC-Es50, 25 Hz) were used to obtain the conversion factor, β , between QPD voltage signal and particle position as part of the supplementary calibration experiments. Additional expansion of the image prior to CCD detection was implemented identically to that described in Section 2.2.1, as was pixel calibration, Section 2.2.5. Determination of the readout delay between channels of the input/output card has not previously been described and is covered in Section 4.3.5.

Water experiments

The first task was to experimentally verify the validity of the FDT calibration method in water since the described calibration method [3] had never before been experimentally tested. The advantage of beginning with a simple viscous fluid like water was that direct comparison of the calibration result could be made with that obtained by PSA. Experiments in water were made using an output laser power of 110 - 120 mW, focussed at a depth of $5 \mu\text{m}$ in the sample. Sample chambers were made using one microscope slide and one coverslip (type 1) with a single layer of double sided sticky tape as a spacer. The sample composed polystyrene beads of diameter $1.65 \mu\text{m}$ (Spherotech) diluted in filtered millipore water with a final bead concentration of $1/10^6$. Chambers were sealed with silicon vacuum grease as per usual.

Entangled F-actin experiments

The actin network (entangled F-actin without cross linkers) was created according to the procedure described in [52], based on the original protocol of [53], but with a bead size and dilution suitable for these experiments. $450 \mu\text{l}$ of G-buffer was added to 1 mg of freeze dried actin (Sigma, from rabbit muscle) together with $5 \mu\text{l}$ of bead solution and $45 \mu\text{l}$ of F-buffer in order to create an actin network with a final actin concentration of 2 mg/ml. In this case the bead solution consisted of $2.1 \mu\text{m}$ polystyrene beads (Spherotech) diluted in millipore water to give a final concentration of $1/250$ that of the bottle concentration prior to addition with the G buffer. The sample was kept on ice during preparation and, after gentle mixing, was transferred to a sample chamber which was then sealed with vacuum grease and left to rotate in the refrigerator for 1 hour before commencing experiments. Experiments were again made using an output laser power of 110 - 120 mW but the depth at which the trap was focussed in the sample was dependent on where beads happened to be localised in the

entangled F-actin network; data was obtained for beads in the range 5-23 μm .

4.3.1 Passive measurements

Passive measurements used the QPD to record the *Brownian motion* of the bead in exactly the same way power spectral analysis would normally be made. Power spectra were gathered at 10 kHz for 3 seconds over 30 windows using a homemade LABview program (onlinecalibration4.vi). Gathering power spectra in multiple 3 second periods was preferred to that of taking continuous data for 90 seconds because of the effects of mechanical drift and drift in the Poynting stability of the laser.

Some months after making FDT experiments, a novel method of determining the optimal time period for data acquisition using optical tweezers setups was published [54]. This involves fitting power spectra to data gathered over different acquisition times, and evaluating the data using the Allan variance. The Allen variance of position is defined:

$$\sigma_x^2(\tau) = 0.5\langle(x_{n+1} - x_n)^2\rangle \quad (4.9)$$

where x_n is the average position over the sample period n , and τ is the time per sample period (acquisition time).

The Allan variance reveals the time scales over which the system is dominated by Gaussian noise or drift [54]. It can thus be used to find the optimal time window over which data should be acquired; the minimum in the Allen variance signals the optimum time period for which further averaging gives no increase in the reproducibility of the average value. A test of the experimental setup using this novel analysis tool showed that the optimal acquisition time using the QPD was $\sim 3\text{s}$ which means, in retrospect, a suitable measurement acquisition period was chosen. Figure 4.2 shows the performance of the QPD used in the FDT experiments, when a 2.1 μm polystyrene bead was trapped in water with an output laser power of 200 mW, for different acquisition times.

In the experiments described by Figure 4.2 acquisition times of longer than 90s were not investigated, preventing observation of the increased Allen variance due to mechanical drift in the sample which was seen by Gibson *et al.*. The reduction in the Allen variance below the spatial resolution of the QPD in Figure 4.2 is meaningless and thus 3s was a reasonable choice of acquisition time for the passive measurements.

For calibration in water, passive measurements were made at the beginning and at the end of the experiment to ensure that trapping conditions were stable throughout. However, for calibration in entangled F-actin, additional passive measurements were also made between the periods of active stage driving to check whether any changes to the network had occurred.

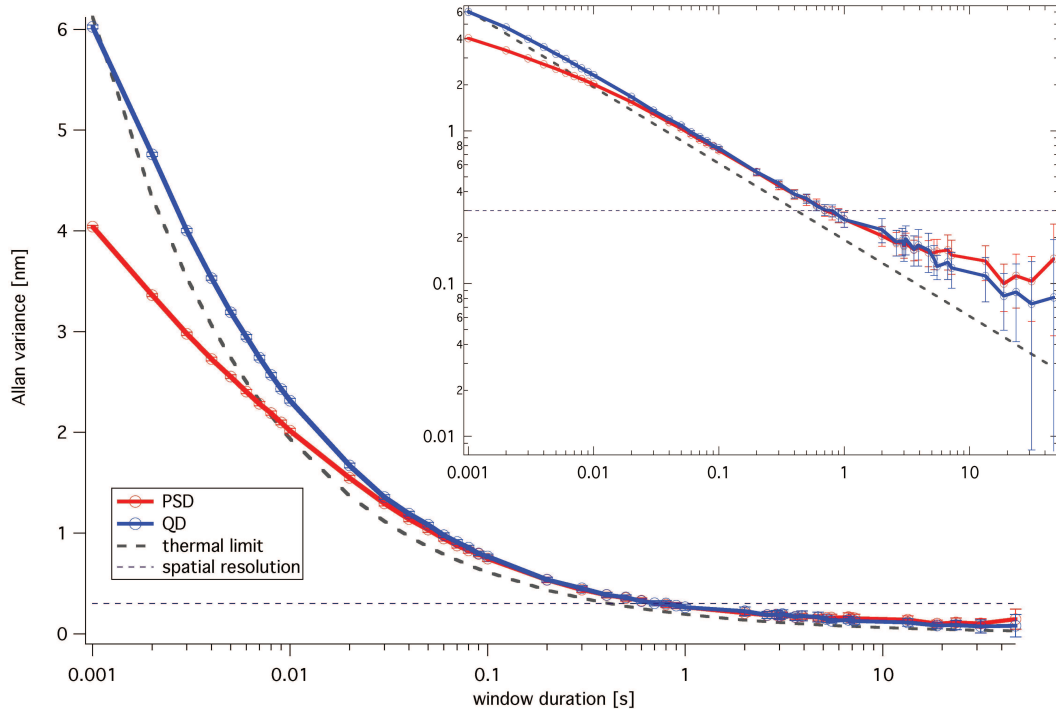


Figure 4.2: The main graph is a semi log plot showing the Allen variance vs. acquisition time for the QPD (blue) used in the FDT experiments, and for a position sensitive diode (red). The thermal limit is represented by a long dashed curve. The plot eludes to the performance of the quadrant photodiode (QPD) over a range of different acquisition time-periods and reveals that the Allen variance reaches a plateau for acquisition times of a few seconds - whereafter further averaging does not lead to a better estimate of the average value. The inset is a log log plot of Allen variance vs. sample period, (τ), showing that at longer acquisition times the variance of the Allen variance increases (larger error bars). Therefore, the optimal acquisition time was ~ 3 s for both the detectors. A short dashed line shows an estimation of the spatial resolution of the QPD, ~ 0.3 nm.

4.3.2 Active measurements

Active measurements were performed by sinusoidally driving the piezoelectric stage (Physik instrumente, P-517.3CL) upon which the sample was mounted. The stage was driven at 10 Hz intervals between 10 Hz and 70 Hz to provide data at 7 separate frequencies of sample perturbation in water. The equivalent experiments in actin were performed with frequency increments of 5 Hz for 19 separate frequencies between 10 Hz and 100 Hz. Corresponding amplitudes for each frequency of stage driving, for the case of calibration in water, can be seen in Figure 4.1. Although driving amplitudes as low as 20 nm were recommended for actin experiments at the higher driving frequencies [49], a driving amplitude of 200 nm was used at all frequencies because of the physical limitations of the stage performance; it is not known whether the stage performs accurately at amplitudes less than 200 nm for

frequencies approaching 100 Hz.

In both the water and actin measurements, data was obtained over 30 s periods with a sampling frequency of 2 kHz using a homemade LABview program (Mario2.vi, written by S. Nader S. Reihani). This program was used to simultaneously record the voltage signal from the QPD and the output voltage signal from the piezo electric stage during active driving of the system as well as enabling control over the active driving itself. Time aligned data showing the position of the bead and the position of the stage were acquired using a fast data acquisition card (National Instruments PCI-MIO-16E-4). The data was then fitted to the known driving parameters and the phase delay, $\Delta\phi$, extracted.

4.3.3 Determining the positional calibration factor or beta value

Direct positional calibration was made independently of passive and active measurements to ascertain the conversion factor, β , that translates the output voltage of the QPD into a real position. The positional calibration factor for each individual bead used in the passive and active experiments was obtained by sinusoidally oscillating the stage using frequency/amplitude combinations of: 2 Hz/200 nm, 2 Hz/500 nm. The stage was driven for 30 seconds with the driving parameters 2 Hz/200 nm, and then immediately afterwards it was again driven with the same driving parameters so that the motion of the bead in the trap could be recorded using both QPD and CCD detection methods. The two detection methods could not be simultaneously employed. Thereafter, the same procedure was followed for the second set of driving parameters.

Detection by QPD offers high temporal (MHz) and spatial (1 nm) resolution but the *linear detection range* is limited to approximately half the radius of the bead in either direction from trap centre, see Figure 2.4 in Chapter 2 for a visual explanation of this. On the other hand, detection by CCD camera remains linear for a much larger range of bead displacements but suffers from a limited temporal resolution because of the frame rate of the camera, 25 Hz. However, even at the maximum frequency of stage driving during direct positional calibration, the temporal resolution was such that there were still at least 5 data points per sinusoid and, therefore, did not restrict fitting of the bead position from CCD images. After expanding the image of the bead so that it filled a little over half the width of the CCD detection area, the CCD pixel size was found to be ~ 11 nm which provided a spatial resolution of around 6 nm.

Recording the motion of a trapped bead using both detection schemes and, thereafter, fitting the recorded data to the known sinusoidal driving parameters allowed comparison of the voltage positional data from the QPD (Figure 4.3a) with the pixel positional data from the CCD (Figure 4.3b). The calibration factor, β , was thereby obtained in volts per pixel. Figure 4.3 shows a trace of the fitted outputs of both detection methods, used to find β .

Obtaining the positional calibration factor in units of V/nm, by this independent posi-

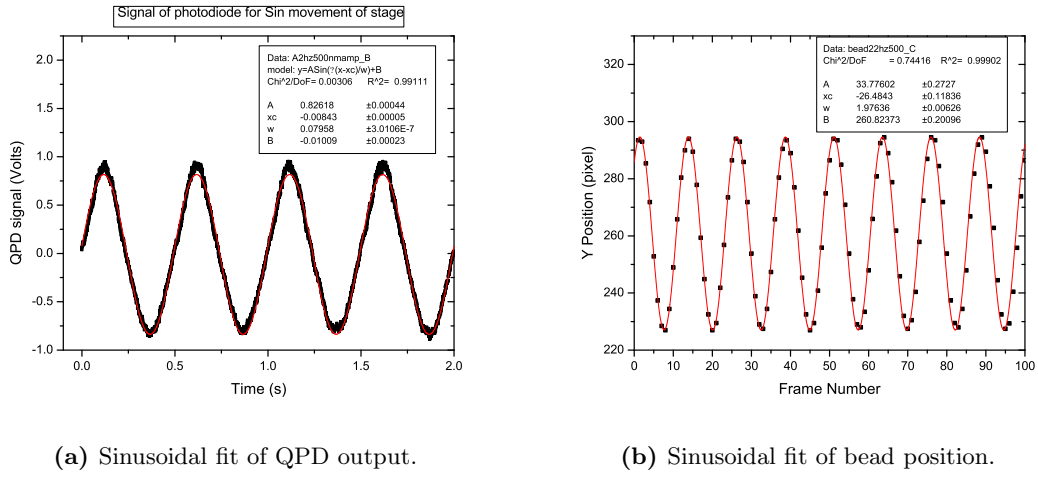


Figure 4.3: Fitted plots of the voltage output from the QPD and the bead position in pixels, found by image analysis, are shown alongside one another.

tional calibration method, required calibration of the pixel size, too.

4.3.4 Pixel calibration

Pixel calibration was made according to the procedure presented in Section 2.2.5. A stuck bead was moved in accurate, predefined steps (100 nm) using the piezoelectric stage and the position of the bead recorded throughout using the CCD camera. Subsequent image analysis provided the number of pixels the bead moved per predefined step and thus the pixel size. The lateral pixel size in the x direction was determined as 11.3 nm. This had to be measured once per experimental day because of regular adjustments to the image expansion but was always found to be a little over 11 nm.

4.3.5 Calibration of the channel delay from the input/output (data acquisition) card

The phase delay between stage and bead oscillations, $\Delta\phi$ in Equation 4.8, was determined from the data acquired during active measurements. However, because there is a finite acquisition time per channel of the data acquisition card, a small time delay enters between reading channels which results in the incorrect calculation of phase delay. Rather than being time aligned, data obtained during active experiments was subject to a systematic error, dependent on the number of channels recorded and the position of each channel in the acquisition sequence.

Stage position was always acquired prior to bead position. Thus, the systematic error always led to an overestimation of the phase delay by the same additional value, $\Delta\phi^{\text{del}}$,

corresponding to the time delay between the respective channels read out. This time delay could be determined by first positioning a stuck bead at the centre of the laser so that the forward scattered light hit the QPD in such a way that there was no voltage difference between each of the 4 quadrants. Thereafter, the stage was oscillated at 2 Hz/200 nm for 1 minute and the position of the bead recorded by QPD. Since the bead is stuck to the coverslip and moves exactly with the movement of the stage, any phase difference seen between sinusoidal fits of the bead movement (QPD trace) and stage position (piezo) can be attributed to the time lag of the data acquisition process. The time delay was found to be 494 μ s and, in principle, need only be measured once but was in fact made three times with the same resulting time delay on each occasion.

4.4 Data analysis

Analysis of CCD images in direct positional calibration and pixel calibration experiments was carried out by Nader Reihani. All subsequent analysis of experimental data was performed by Mario Fischer. A detailed description of the procedures used in data handling and the process for extracting physical properties of the viscoelastic medium from the measured data are not discussed but are adequately described elsewhere [49, 51]. It should, however, be noted that all of the equations presented in Section 4.2 were in frequency space whereas the experimental data recorded was of the positions visited by a trapped bead, $x(t), y(t)$, during a finite measuring time, T_{meas} and with a finite sampling rate, f_{sample} .

4.5 Results and discussion

First of all, the results of the calibration experiments in water are compared for the two calibration methods, power spectral density (PSD) and fluctuation dissipation theorem (FDT), and a discussion of the relevant errors is made. Thereafter, the values of κ determined by the FDT method for a bead in a solution of entangled F-actin are presented for a range of driving frequencies and compared to an equivalently sized bead, trapped at the same depth and laser power, in water. Finally, the local viscoelastic moduli of the actin network surrounding the trapped bead are shown versus the oscillation frequency of active stage driving. The shear modulus $G(f)$ of the viscoelastic medium is found from the friction retardation spectrum $\tilde{\gamma}(f)$ by the generalised Stokes-Einstein relation.

4.5.1 Calibration in Water

Experiments employing the FDT method were first carried out in an experimental environment where the trapped particle was surrounded by a simple fluid with well known viscous properties, water. This permitted a direct comparison of the performance of the

FDT method with the reliable and well established power spectrum method, described in Section 1.3.

The determined value of calibration factor, β , is first compared for the two calibration methods ($\beta^{(\text{PSD})}$ and $\beta^{(\text{FDT})}$) and for the independent method of direct positional calibration ($\beta^{(\text{SIN})}$), presented in Section 4.3.3.

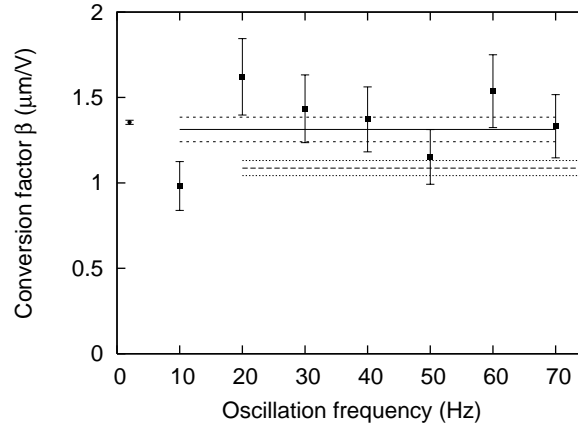


Figure 4.4: The voltage to position conversion factor is shown for the three different methods employed. The average value of the calibration factor found by the power spectral density method, $\beta^{(\text{PSD,av})}$, is denoted by the long dashed line. The dotted lines either side of the long dashed line represent plus and minus one standard deviation, a relative error of 4.1 percent. Frequency dependent values of the calibration factor found by the FDT method, $\beta_K^{(\text{FDT,ex})}$, are shown as filled squares, where K is the frequency of stage oscillation. Error bars show the large relative error of 14 percent. The solid line shows the average of the experimental values determined by the FDT method, $\beta^{(\text{FDT,av})}$, with short dashed lines showing the standard deviation (relative error 5.5 percent). Lastly, the filled circle with error bars represents the conversion factor found by independent positional calibration at 2 Hz, $\beta^{(\text{SIN})}$.

Figure 4.4 shows the values of the position to voltage calibration factor as determined by three separate methods. The calibration factor determined by the FDT method has a large relative error because of statistical errors and the errors arising from temperature uncertainty. However, a value with lower statistical uncertainty was obtained by averaging, solid line in Figure 4.4. The independent method of positional calibration produced a value of β , filled circle, that agrees well with that obtained by the FDT method, $\beta^{(\text{FDT,av})}$, within the error bars. The value of the calibration factor from power spectral analysis ($\beta^{(\text{PSD,av})}$) is, on the other hand, considerably lower.

The value of spring constant for a $1.6 \mu\text{m}$ polystyrene bead trapped in water was found to be $46.1 \pm 1.5 \text{ pN}/\mu\text{m}$ for the PSD method, where $\pm 0.5 \text{ pN}/\mu\text{m}$ arises from statistical error and $\pm 1.0 \text{ pN}/\mu\text{m}$ stems from temperature uncertainty. By way of comparison, the value of spring constant determined for the same experimental conditions but using the FDT

method was 43.6 ± 1.7 pN/ μ m, where ± 1.2 pN/ μ m is due to statistical errors, ± 0.1 pN/ μ m comes from temperature uncertainty and ± 0.4 pN/ μ m arises because of uncertainty in the value of the calibration factor found by independent positional calibration, β^{SIN} .

This information is better represented by Figure 4.5 which shows the trap stiffness measured by the two different calibration methods.

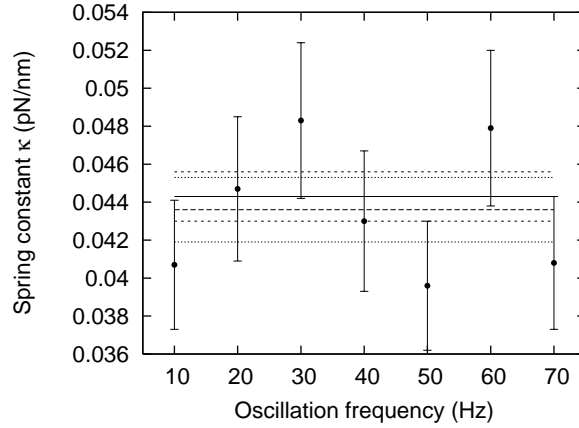


Figure 4.5: The trap stiffness obtained by two different calibration methods. The long dashed line and grey shaded area show the average value of trap stiffness found by PSD method $\kappa^{(\text{PSD},\text{av})}$ and its relative error of 3.3 percent, respectively. In the PSD experiments the power spectra were fitted up to a frequency of 2 kHz. The filled circles show the experimentally measured values of trap stiffness for the 7 different stage oscillation frequencies. Error bars (relative error ~ 8.5 percent) indicate the uncertainty due to statistical errors, uncertainty in the positional calibration and uncertainty in the temperature. The solid line represents the average of these 7 points $\kappa^{(\text{FDT},\text{av})}$. All 7 data points were included in the averaging because the error bars of all 7 points pretty much overlap. Two dotted lines indicate $\kappa^{(\text{FDT},\text{av})} \pm$ a relative error of 4 percent.

The calibration results of the two methods are seen to agree within the given error bars, for a bead trapped in water. Therefore, the FDT method is proven to be a valid calibration method. However, the most interesting aspect of the FDT calibration method is the opportunity it provides to make calibration experiments in media where the properties are largely unknown. For example, the cytoplasm.

4.5.2 Calibration in Entangled F-actin

A less complicated starting point than the crowded environment of the cytoplasm is to verify the validity of the FDT method in a network of entangled F-actin, where there are no ongoing bio-active processes. The presence of molecular motors or large perturbations from other bio-active processes would render the FDT invalid in certain frequency ranges. It is unclear whether this would appear clearly enough in the experimental data so that the effected frequencies could be excluded from the analysis process.

Rotation of the sample in the refrigerator for 1 hour prior to experiments was supposed to give an even distribution of beads and actin filaments throughout. Beads were fairly well distributed amongst the sample but the actin network created was not entirely homogenous. Beads were seen to fluctuate quite freely in some regions, barely hindered by the presence of the actin network, whereas in other sections of the sample they seemed motionless. Therefore, it is reasonable that the results of the calibration experiments show a very reproducible value of trap stiffness but varying viscoelastic properties. Figure 4.6 shows the spring constant of the optical trap and the effective spring constant felt by the bead as a result of the surrounding network ($\frac{1}{|\chi(f_k)|}$), for 19 different stage oscillation frequencies up to 100 Hz.

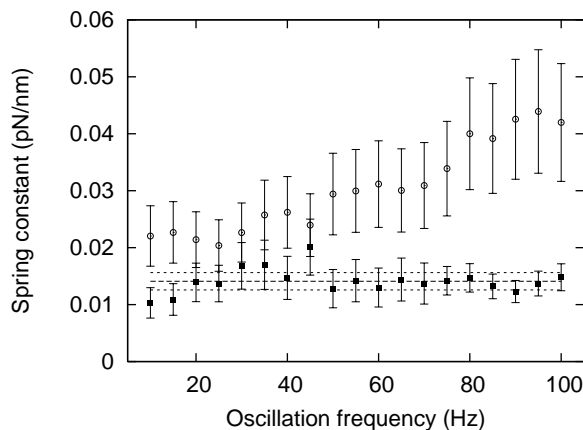


Figure 4.6: A plot of spring constant vs. stage oscillation frequency. Filled squares with error bars represent estimates of the optical trap stiffness for various frequencies of stage oscillation. The long dashed line is the average of these points ($\kappa^{(av)}$) and dotted lines show \pm one standard deviation. The effective spring constant felt by the bead, $\frac{1}{|\chi(f_k)|}$, is shown by open circles with error bars.

The average trap stiffness of the values obtained at different frequencies of stage oscillation was $\kappa^{(av)} = 1.41 \pm 0.15 \times 10^{-2}$ pN/nm. An independent measurement using the same experimental parameters (2.1 μ m polystyrene bead, trapping depth 11 μ m and an output laser power of 110-120 mW) but in water, found the trap stiffness to be in the range 1.4-1.8 $\times 10^{-2}$ pN/nm. Thus, the measured trap stiffness in an actin solution is slightly lower than that measured in water. Since the refractive index of the actin solution is unknown, it is difficult to make a correction for the dissimilarity in refractive index between water and a solution of actin. However, if the refractive index of actin lies somewhere between water ($n = 1.33$) and that of a cell ($n \sim 1.5$) then the spring constant in a solution of actin could be as low as one third of the value in water, when estimated using Eq.3 of reference [55].

The ultimate goal of the FDT calibration procedure is to determine the viscoelastic properties of a cell so that other *in vivo* microrheology experiments can be made. However, as a starting point the viscoelastic properties of a solution of entangled F-actin, determined

by the FDT method, should be compared with previous *in vitro* experiments in actin as a means of verifying the authenticity of the FDT method. Figure 4.7 presents the shear storage G' and shear loss G'' moduli of the actin network, as determined using the FDT method.

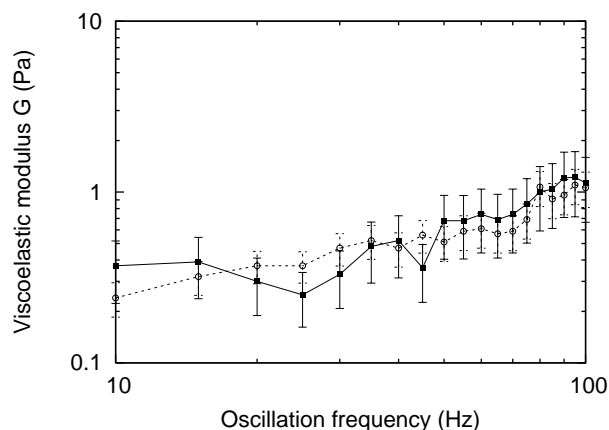


Figure 4.7: Viscoelastic moduli vs. stage oscillation frequency as found using the FDT method. Filled squares with a solid line shows G' and open circles with a dotted line gives G'' .

Two very typical characteristics of an actin solution are that G' is independent of frequency at low frequencies and then scales as $f^{\frac{3}{4}}$ for higher frequencies, page 123 of reference [32]. The data in Figure 4.7 displays a plateau in G' and G'' at low frequencies and then enters a region where $G', G'' \propto k^{\frac{3}{4}}$ for the higher frequencies of stage oscillation k . Hence, the viscoelastic properties of the actin solution as measured by FDT calibration are in support of previous studies [56]. Furthermore, values of viscoelastic moduli determined by FDT calibration agree well with published values [50], where a similar actin concentration was used. Figure 4.8 shows the viscoelastic modulus in units of Dynes/cm² as determined by Mason *et al.*. Comparison of Figures 4.7 and 4.8 can be made by knowing that 1 Pa = 10 Dynes/cm².

4.6 Summary

The proposed FDT calibration method [3] was implemented experimentally and shown to operate satisfactorily in water. When calibration results of the FDT method were compared to those of PSD analysis, for the same experimental conditions, they were found to agree within the error bars.

Making no assumption of the friction felt by the trapped bead in a and having no prior knowledge of the viscoelastic properties of the medium, calibration was made in a solution of entangled F-actin and the resulting spring constant was found to be slightly lower than

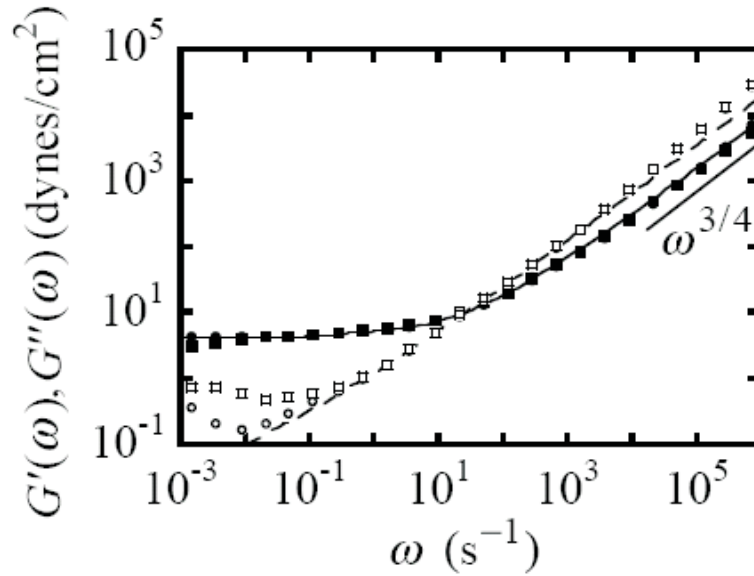


Figure 4.8: Viscoelastic moduli vs. frequency. The figure is taken directly from the publication of Mason *et al.* and compares well with the values of viscoelastic moduli found by the FDT method.

that of an independent, equivalent experiment in water. This is not surprising since the refractive index of an actin solution is higher than that of water which reduces the refractive index difference between the bead and its surrounding. Viscoelastic parameters such as the shear storage modulus G' and shear loss modulus G'' were extracted by analysis of the data obtained through FDT calibration and showed a good resemblance to the results of previous *in vitro* investigations; the same frequency dependent trends in viscoelastic moduli were observed and the determined value of G for an actin concentration of 2 mg/ml was similar.

Having proven the validity of the FDT method it was important to develop have an experimental system capable of employing this calibration method in combination with confocal microscopy so that micro-rheology experiments, such as measuring the *in vivo* persistence length of a microtubule, could be made. Chapter 5 discusses the process of integrating optical tweezers with confocal microscopy to provide a powerful resource for investigating the mechanics of cell division.

CHAPTER 5

Confocal-tweezers

There are many wonderful tools in the biophysicist's toolkit; each tool offers something different, or may even offer the same thing but with detection on a different timescale. Two complimentary techniques available from such a toolkit are optical tweezers and confocal microscopy. In this chapter, the integration of the two techniques into one system is presented and tested for the case of two dimensional scanning. The three dimensional case is discussed and suggestions for how three dimensional confocal-tweezers could be implemented as a future work is considered along with the potential applications.

5.1 Overview

Although there was no immediate need for an integrated system of confocal-tweezers, since the insertion of gold colloids into *S. pombe* had not yet been completed, it would certainly be useful if one could simultaneously visualise a sample while using force-scope optical tweezers to investigate it. Optical tweezers have an advantage over other methods of manipulation or force measurement in that they are able to reach inside a living cell without damaging the cellular environment under investigation [38]. Furthermore, with a quadrant photodiode situated at the back focal plane (Section 1.3.2), positional detection with a spatial resolution of a few nanometres and a temporal resolution of microseconds is achievable along with force measurements in the pico Newton regime. One can, therefore, imagine how such a system could be used to investigate the actions of organelles and macromolecules *in vivo*, since bio relevant forces are largely of this order of magnitude and confocal microscopy reveals detailed information about the landscape of a cell as a whole.

Simultaneously measuring bio relevant forces while visualising participating parts of the cell opens up new possibilities for research that are intrinsically linked to the overall goal of this project. For example, to investigate the polymerisation and depolymerisation of microtubules *in vivo* and to measure the forces upon them under cell division.

5.2 Confocal microscopy

Confocal microscopy is used by biophysicists for a variety of purposes that range from observing the effects of drugs on the evolution of intracellular processes, to simply following the movement and positioning of a specific protein under cell division. Strains of cells that have been genetically modified so that green fluorescent protein (GFP) is expressed in one or more of their organelles, a technique that resulted in the three founders receiving the Nobel prize for chemistry in 2008, are used to build up three dimensional pictures of cells by making high quality confocal images over multiple focal planes in what is known as a three dimensional stack of images.

Confocal microscopy was first demonstrated in the late 1980's but had been patented in 1957. The basic concept is that light originating from planes other than the intended focal plane can be filtered out by the use of a correctly positioned pinhole aperture or spatial filter. The pinhole improves the quality of the detected image by removing unwanted noise originating from other planes outside the confocal volume so that only fluorophores excited within the confocal volume (200 nm^3) are detected. The advantage of this is that unwanted bleaching of other sections of the sample outwith the illuminated confocal volume is avoided and only fluorophores from a specific thin section of the sample contribute to the final confocal image because of the filtering effect of the pinhole aperture. Figure 5.1 shows a schematic of how this works.

Standard confocal microscopes operate by scanning either the sample stage through the focus of the objective, or the focus of the objective through the specimen, in order to build up a confocal image of the sample. A three dimensional image of the sample is obtained by stepping the sample or the objective in small axial increments, shifting the confocal plane in the axial direction, and repeating the scan of the lateral plane at each of the axial positions. The time it takes to capture a three dimensional image (temporal resolution) is governed by the scanning speed, which cannot be increased indefinitely since there is a trade off between scanning speed and the spatial resolution of the final image. Confocal microscopy provides images with high spatial resolution that span over large fields of view but is limited as a method of observing fast dynamics. Instead, fluorescence microscopy and single particle tracking are preferred since they allow molecules tagged with quantum dots or labelled with some sort of fluorescent protein to be followed with reasonable positional accuracy and high temporal resolution. However, combining confocal microscopy and optical tweezers together provides the opportunity to study interactions that occur on extremely short timescales (MHz) and apply forces to manipulate the cell, while still maintaining a picture of that entire cell. This is useful in the case where the area of the cell effected by the application of a force by the tweezers is unknown. An image of a yeast cell taken using Leica's SP5 confocal microscope is shown in Figure 5.2.

Optical tweezers have been extensively discussed during the course of this thesis (Chapter1)

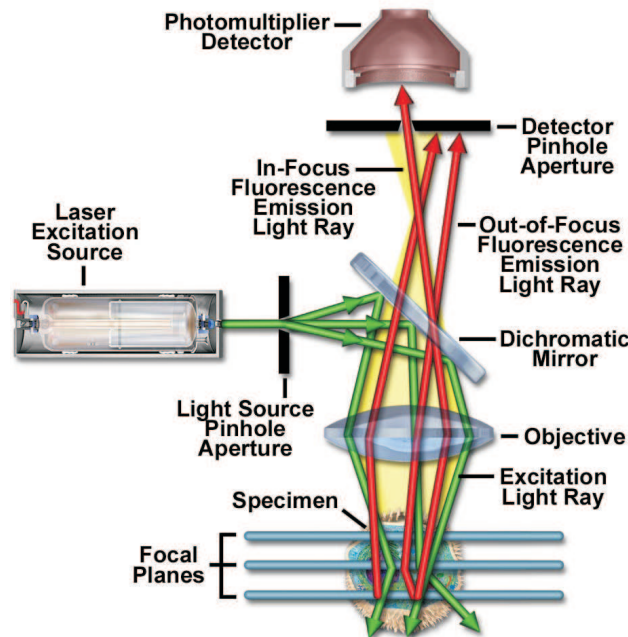


Figure 5.1: A standard confocal setup showing the excitation of specific focal planes and the filtering of out of plane light by the pinhole aperture. Schematic is downloaded from: <http://www.olympusfluoview.com/theory/LSCMIntro.pdf>

and are not further described in this chapter. The purpose of this work was to combine two of the best and most frequently used techniques into one powerful tool, offering the benefits of both techniques in one integrated system.

5.3 Previous research in confocal tweezing

Optical tweezers have been combined with confocal microscopy on several occasions [57, 58, 59]. Some take the extreme measure of completely decoupling trapping from confocal imaging by making use of two microscope objectives [58]. Of course, this simplifies things slightly because no compensation is required for the movement of the lower objective when a three dimensional stack is made. However, it is more expensive to employ two objectives and sets a limitation on the sample thickness because of the limited working distance. Furthermore, it means position detection at the back focal plane would be impossible and thus complex positional detection using backscattered light would be the only option available [60].

Optical tweezers have also been combined with confocal microscopy using only one objective lens [57, 59]. The conflict between three dimensional imaging and trapping has been known for many years, but the first demonstration of a practical solution to overcome this conflict was made by Hoffmann *et al.* in 2000. Employing fast scanning correctional



Figure 5.2: The confocal image is of a type D817, *S. pombe* yeast cell with green fluorescent protein in the nuclear and plasma membranes.

optics to change the divergence of the trapping laser at the back aperture of the objective, the shift in trap position caused by the movement of the objective lens could be compensated for [59]. They used an external lens that was mounted on a translational stage and positioned in front of the laser output to control the divergence of the trapping laser as it entered the back aperture of the objective. The movement of the translational stage was then synchronised with the movement of the objective lens according to a calibration curve made for each individual objective lens. i.e. the translational stage position and the relative axial position of the objective were plotted together to make a calibration curve. They demonstrated an impressive range of axial movement of the objective for which the translational lens would allow compensation, between 20 and 50 microns depending on the objective characteristics.

When making a three dimensional confocal image over a considerable field of view it can take a few seconds to scan the entire specimen, during which time the specimen may move and result in a blurring of the image. Hoffmann *et al.* showed that chloroplasts of *Elodea densa* could be successfully imaged using the trap to hold the sample in position and thereby avoid any blurring of the scanned images. However, if one wishes to make quantitative force measurements then this method has the disadvantage that the laser power at the focus decreases as the translational stage, holding the convex lens, is moved away from the trapping laser. In other words, the compensation technique used to keep the position of the trap constant in the sample gives rise to a changing trap stiffness. Furthermore, the correctional optics are part of a feedback loop and there is a small time delay, 20-100 ms, between reading the position of the objective and the translational stage actually reaching the correct position. However, Hoffmann *et al.* found that the lag time had no visible effect on the resultant images because it was smaller than the time between two optical sections of a 3D stack.

Later, Goksör *et al.* used a similar method of compensation to trap and hold a yeast

cell in position while a three dimensional scan of the cell was made [57]. However, they simplified the calibration procedure by keeping the objective lens at a fixed position and instead chose to move the piezoelectric stage that holds the sample, thus avoiding the complex algorithm connecting the objective lens position and the position of the external lens. They also suggest that the decrease in trapping efficiency with movement of the external lens can be compensated for by increasing the output power of the laser but this is extremely difficult in practice.

Perhaps because of these problems, no attempt to combine confocal microscopy with accurate positional detection, to create force-scope optical tweezers within a confocal system, has ever been reported. Although accurate positional detection by AFM has been successfully combined with confocal microscopy [61], optical tweezers offer something entirely different in terms of the force detection range they operate at, a few pico Newtons as opposed to hundreds of pico Newtons or nano Newtons by AFM, and their unique unparalleled ability to manipulate non invasively inside a cell.

The complexity of the compensation optics required for three dimensional confocal images and optical trapping when utilising Leica's SP5 confocal system, in comparison to that used by Hoffman *et al.* or Goksör *et al.*, is considerably less. This is because of the unique way in which two dimensional scanning of the sample takes place, discussed in Section 5.4.1.

5.4 Integration of the tweezers

5.4.1 2D scanning

The key to integrating optical tweezers with confocal microscopy lies with the revolutionary way in which the Leica SP5 confocal system scans a sample. Unlike the standard confocal microscopy scanning techniques described in Section 5.2, the SP5 system does not require movement of the stage or the objective in order to create a two dimensional confocal image. Scanning is facilitated by the use of two galvanic mirrors, positioned in the optical path and well below the objective lens, that precisely control the angle at which the excitation laser light is directed through the objective. Moving independently of one another but still working together, the galvanic mirrors or MEMS (micro electromechanical systems) can project the excitation light to any point in the xy plane. Instead of moving the sample, or the objective, the SP5 employs this novel scanning method to scan the sample in x and y by the movement of the two galvanic mirrors alone. The mirrors are precision controlled by computer because the change in angle that they induce is extremely small. The pair of mirrors is called a tandem scanner and can be seen in the schematic diagram of Figure 5.3.

The absolute scannable area in the two dimensional lateral plane is restricted by the off axis aberrations of the objective. The furthest lateral scanning position obtainable with the SP5 system is defined by Leica. The propagation path of the excitation laser should

never be outwith the central part of the objective lens and is automatically imposed by the system. However, this limitation on the lateral reach of the tandem scanner is not overly prohibitive. The largest area visible for the slowest scanning speed and a modest pixel resolution is a reasonable, with a 100 times oil objective, is $150\mu\text{m}$ by $150\mu\text{m}$. Faster scanning does, of course, result in a reduction in the permitted scanning area which is, again, automatically imposed by the SP5 system. One can always move the sample stage to the point where the interesting region of the specimen becomes accessible to the tandem scanner, if the imageable area was insufficient.

Performing a scan in three dimensions requires either movement of the objective, or movement of the sample stage to a new axial position since the tandem scanner only operates in the lateral plane. Such movement would also result in a shift in the axial position of the optical trap and would require some kind of feedback compensation routine, details of which are discussed in Section 5.7.1.

5.4.2 Coupling the trapping laser into the optical path of the SP5 confocal system

A dichroic mirror (Laser Components, 575399) that is almost perfectly reflective at 1064 nm, 45 degrees incidence, and completely transmissive throughout the visible region (400-700 nm), also at 45 degrees incidence, was inserted into the optical path of the microscope and had two important roles. Firstly, it facilitated the coupling of trapping laser light (1064 nm) into the optical path, thereafter focussed by the objective lens to create optical tweezers. Secondly, it also ensured that the visible light could pass freely, either to the sample in the form of excitation laser light, or back toward the photomultiplier tubes and subsequent detection. The dichroic mirror and the tandem scanner described in Section 5.4.1 are both shown in Figure 5.3.

The excitation lasers are situated in an external housing separate from the microscope. An acousto-optic tuneable filter (AOTF) permits the user to select the individual laser line or multiple laser lines that can enter the system, depending on the excitation requirements of the dyes incorporated into the specimen. Thereafter, an acousto-optic beam splitter (AOBS) deflects the laser line or laser lines that were transmitted by the AOTF into the optical path of the microscope and therein connects the excitation lasers to the scanning optics. Furthermore, this allows light emitted from the fluorophores in the specimen to pass straight through un-deflected towards the photomultiplier tubes.

The scanning optics are located beneath the dichroic responsible for introducing the trapping laser. Therefore, the stability of the trap could not be and was not effected by the motion of the galvanic mirrors of the tandem scanner. The novel scanning method of the SP5 confocal system and the stability of the trap while scanning is the reason why force-scope optical tweezers could be so simply combined with confocal microscopy.

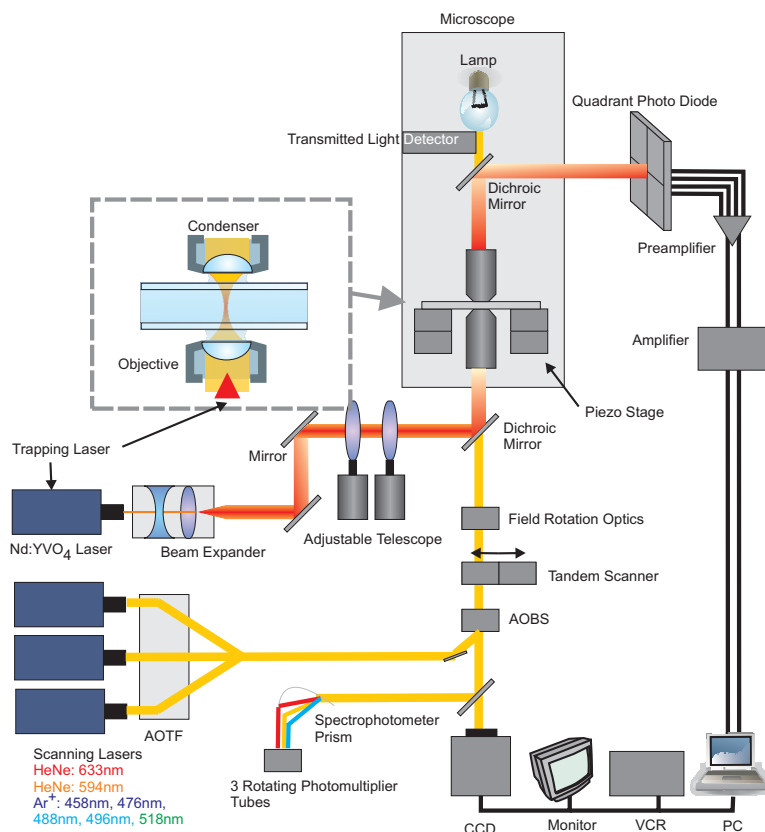


Figure 5.3: A schematic of the integrated confocal-tweezers system showing how the trapping laser is coupled into the SP5 confocal system.

On the other hand, inserting a dichroic mirror into the optical path above the scanning optics meant that excitation light and emitted light would both pass through an additional optical component, which could potentially reduce the quality of the scanning i.e. introduce some positional shift and/or time delay because of the increase in optical path length caused by the finite thickness of the dichroic. However, the dichroic was purposefully purchased at the thinnest available thickness (1.5 mm) and was found to have no detectable effect on the synchronisation of the scanning process or the resultant images.

Position detection was achieved using a quadrant photodiode and calibration was carried out using power spectral analysis, as previously described in Section 1.3.2.

5.5 Experimental method

The particle under investigation was trapped by the tweezers and a series of power spectra were made while the confocal microscope made a series of two dimensional images. Measurements on the gold colloids were made at a depth of 1 μm inside the sample, more than five times the particle radius, to avoid Faxen's corrections to Stoke's law for proximity ef-

fects of the surface. Measurements on the $1\ \mu\text{m}$ polystyrene bead were made at a depth of $4\ \mu\text{m}$ from the same reason.

The final spring constants presented in Section 5.6 represent an average of 3 measurements per bead for 3 separate beads of each bead type. Spring constants obtained for the gold colloids are compared with findings from experiments which took place at depths between $2\ \mu\text{m}$ and $6\ \mu\text{m}$ [28], while data for the 1 micron bead is compared to recently reported values of spring constant [26] for the same size bead but with a slightly different laser power. This was overcome by measuring the power at the back aperture of the objective and making an estimate of the power at the focal plane [62]. Thereafter, the data taken using the confocal-tweezers setup could be normalised with respect to laser power and compared to the previously obtained values which were of a different laser power [26].

5.6 Result and discussion

The confocal microscope was used to capture two dimensional confocal images while simultaneously obtaining a power spectrum of the trapped particle. This was done for 80 nm and 150 nm gold colloids as well as $1\ \mu\text{m}$ polystyrene beads, where the stated value is the particles diameter. The values of the determined spring constants obtained under scanning were found to agree well with those found when the galvanic mirrors were stationary and also with values previously reported in the literature [26, 28]. An image of the 80 nm gold colloid and its corresponding power spectrum are shown in Figure 5.4, the power spectrum shown is of data recorded while simultaneously acquiring the presented image.

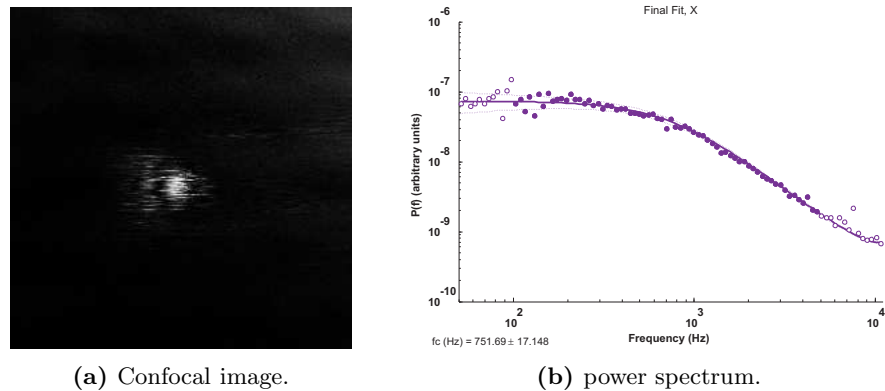


Figure 5.4: The confocal image shows a 2D image of an 80 nm bead in an optical trap, taken in reflection mode. The power spectrum shown is a fit of the data collected for the same 80 nm bead while the scan took place.

Brownian motion of an 80 nm gold colloid is considerable which causes the bead to appear a little stretched out or blurred in Figure 5.4 because the colloid moves faster than the scanning system can acquire an image. In addition, the colloids are sufficiently smaller

Table 5.1: Table showing the measured spring constants in x and y obtained for the three beads we investigated compared to values in the literature, Hansen *et al.* and Rohrbach. All values of κ are given in pN/ $\mu\text{m}/\text{W}$ and the diameters in column D are given in nanometres. Those values not available in the literature are denoted by a NA.

D	Material	κ_x	κ_y	κ_x Literature	κ_y Literature
80	Gold	7	7.2	6	NA
150	Gold	14.8	23.2	15	NA
1000	Polystyrene	1055	1014	2820	2520

than the 633 nm laser light used to image them so that in actual fact one sees the point spread function of the colloid which makes it appear larger than it really is.

Figure 5.4 also shows that the power spectra taken while scanning are as good as any others taken in a stationary environment. This should be the case since, as far as the trapping laser and quadrant photodiode detection system are concerned, the environment is stationary. The Lorentzian fitting for all data sets (one example is shown in Figure 5.4) suggest that scanning the sample has no effect on the measured power spectra or therein the calibration process. However, some high frequency noise can be seen in the power spectra of the 80 nm gold colloids but was disregarded from the Lorentzian fit. This was present over a large number of the 80 nm gold data sets, including power spectra taken while not scanning the sample, the source of which is still not clear but is not thought to be in any way linked to the scanning.

Power spectra from the 150 nm gold colloids and the 1 micron polystyrene beads, as well as the corresponding confocal images taken in reflection mode, are not presented here. However, they can be found in the SPIE proceeding [62] along with further experimental details but Table 5.1 showing the determined spring constants under scanning for comparison with other investigations [26, 28] is included.

Looking at Table 5.1, the measured values of spring constants for the gold colloids compare well with literature [28]. The influence of spherical aberrations on the trap stiffness can be quite considerable as one moves in depth [63, 64], when using an oil immersion objective, and because the depth is not explicitly stated in the literature with which the data is compared then it is hard to make any conclusions about how efficient the confocal-tweezers are at trapping. However, the main goal of making a reliable calibration of the trap for the purpose of force measurements while simultaneously compiling a two dimensional confocal image has been achieved. The value of the spring constant for the 1 micron bead is also in a region comparable to that previously obtained.

5.7 Future work

It is clear that for this system to be of real advantage then one should extend the capabilities of confocal-tweezers to three dimensional scanning. Only then can the potential of the experiments discussed in Chapter 3 be realised. For example, to measure the pushing and pulling forces generated by the polymerisation and depolymerisation of microtubules in *S. pombe*, *in vivo* which will hopefully lead to a better understanding of the role that the cytoskeleton plays in cell division.

5.7.1 3D scanning

There have been other attempts to compensate for the movement of the objective lens and its effect on the position of the optical trap, while constructing a three dimensional confocal image [57]. The only difference is that the system must now contend with the additional complexity of quantitative force measurement as well as the movement of the stage. Therefore, the suggestions for future work on the development of three dimensional force-scope confocal-tweezers are based on this.

Using a moveable lens, positioned in front of the laser and accurately driven by LABview software, the divergence of the laser beam and thereby the position of the trap focus within the sample can be precisely controlled. If the movement of the external lens is coupled to the movement of the stage, with the appropriate calibration between the two made in advance, then any movement of the stage can be compensated by the subsequent movement of the external lens with feedback control. Since the movement of the stage is also controlled by LABview software, the details of which are not yet available from Leica, then it should be relatively straight forward to combine the two systems together so that their movements are synchronised during the scanning process. The flexibility of focussing the trap anywhere in the sample regardless of the image plane of the confocal should be maintained though, so that the coupling of the two systems can be switched on and off by the user. However, due to time constraints and restrictions on access to software controlling the objective lens, no part of the described idea has yet been attempted.

It is unclear whether the change in trap stiffness observed by Hoffmann *et al.*, said to be caused by the change in divergence of the trapping laser, can be solely attributed to this or whether spherical aberrations again play a role because only oil immersion objective lenses were investigated. Perhaps the change in trapping efficiency over five microns axial distance, the typical thickness of a z stack required to image *S. pombe*, would be negligible if the appropriate immersion medium were selected; axial trap stiffness only varies by 5 percent with an increase in depth of 5 microns and the corresponding changes in lateral stiffness are much less [14]. One could also repeat the experiments with a water immersion objective to observe the effect of solely changing divergence. Depending on the severity of the affect of divergence on trapping efficiency, there may be some merit in increasing the

laser power as a means of compensating, as suggested by Goksör *et al.* but this would be complicated.

5.8 Summary

Quantitative force measurement and simultaneous two dimensional confocal imaging was demonstrated for two sizes of metallic nano particles and also for a one micron polystyrene bead. This small piece of work was a proof of concept and the really interesting experiments are dependent on the implementation of fast compensating optics to allow simultaneous force measurement and three dimensional confocal imaging. This will be of substantial importance when making *in vivo* experiments to investigate the role of the cytoskeleton and its control mechanisms in positioning the nucleus of an *S. pombe* yeast cell during cell division; in particular the pushing and pulling forces applied by growing and shrinking microtubules.

CHAPTER 6

Three dimensional optical control of individual quantum dots

6.1 Overview

The use of fluorophores for visualisation of molecules and for SPT experiments has been very successful. Single particle tracking offers positional localisation of the particle well below the diffraction limit, typically to within a few nanometres, with corresponding temporal resolutions of milliseconds or a few tens of microseconds [65]. However, quantum dots (QDs) have been limited to single quantum dot tracking (SQDT) experiments that observed the lateral diffusion of receptors in the membrane of neurons [66] and have never been used to manipulate molecules or cell organelles inside a cell because as it was hypothesised that a substantial optical power (20 W) would be required to trap a single QD using a continuous wave laser [67]. If one could use optical tweezers to non invasively manipulate quantum dots inside a cell, with a relatively low optical intensity, and also employ SPT software to follow the movement of the QD after manipulation then a whole variety of experiments within the confines of one cell could be made. For instance, one could manipulate a QD (attached to a specific molecule) into different regions of the intracellular environment and thereafter, observe the resultant diffusion back to the target area by SPT.

In addition, one could further employ optical tweezers to investigate the forces involved in the binding of a molecule upon arrival at its target, by trapping the QD and observing its motion. The advantage of this is that it could all take place in one experimental investigation, making it a powerful tool for studies of intracellular dynamics. Investigating the mechanics of cell division in *S. pombe* yeast cells would definitely benefit from the development of such a technique and so the work detailed in this chapter is relevant to the global project goal of this thesis. Experiments demonstrating the full potential of such a technique were not realised in this study, i.e. combining optical trapping and manipulation

of QDs with SPT in a biological system of interest. Although, verifying that single QDs are trapped and that quantitative information on the trapping force is obtained, provides a solid base from which to go on and develop such a system and realise the potential.

In this chapter, the trapping of individual colloidal quantum dots is verified by two separate methods and the typical trapping forces involved revealed. An additional suggestion for further work is made that may allow questions relating to the exact properties of colloidal QDs to be answered.

6.2 What are quantum dots?

Quantum dots have, amongst other things, revolutionised the field of biology by providing a stable alternative to organic dyes. Their emission wavelength is dependent on both; the bandgap energy of the semiconductor material they are produced from and the QDs physical size. QDs can be made by traditional semiconductor growth techniques such as molecular beam epitaxy. Normally when growing semiconductors, one selects a suitable lattice-matched substrate upon which to grow new layers of a different material. This essentially means that the layer of atoms upon which the new material is to be grown (the substrate, typically silicon) should have the same sized spacing as that of the new material in order to obtain a perfect match. However, when this is not the case, unwanted effects such as strain within the crystal layer can eventually lead to defects or fractures in the material. QDs are created when there is a mismatch of the substrate lattice to the new material, the only way to release the strain in the plane is to form a small 'island' in the third dimension. This was first explained to me using the analogy of laying a carpet that is too large for the room, no matter what happens there will always be a region where the carpet bulges upwards.

Quantum dots have come a long way since then with the development of colloidal QDs, making fabrication a somewhat simpler and less expensive process. The fine details of creating QDs by colloidal synthesis are not discussed in this thesis but these nano-crystals can be accurately grown in solution by controlling various critical parameters such as temperature and monomer concentration. A QD is exactly that, a semiconductor nano-crystal; sharing properties of semiconductors and molecules. The QDs used in this investigation are, indeed, colloidal QDs. They generally consist of only a few thousand atoms and are no more than 10-15 nm in total diameter, including the shell and stabilising polymer coating. Figure 6.1 is a representation of a colloidal quantum dot with the relevant scale indicated.

Returning to the biological relevance of QDs, as probes, they offer extreme flexibility in emission wavelength (tunability is achieved by manipulating core size) and functionality. The latter is achieved by replacing the outer polymer coating with a new coating that facilitates specific binding to a target molecule or organelle within the cell, providing the user with reasonable control of the QDs interaction with its surrounding environment.

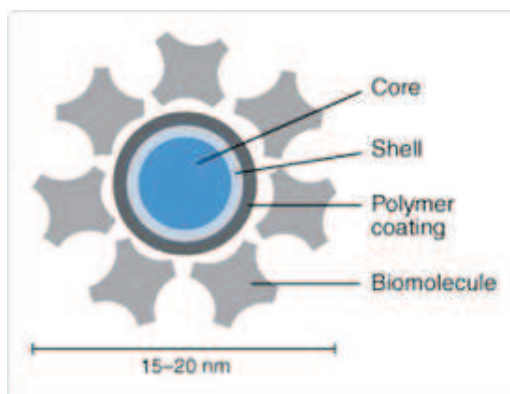


Figure 6.1: The various components and overall dimensions of a typical quantum dot are shown roughly to scale. This figure is downloaded from Invitrogen's web page, <http://www.invitrogen.com/site/us/en/home/brands/Molecular-Probes/Key-Molecular-Probes-Products/Qdot/Technology-Overview.html-structure>

QDs are ideal for intracellular studies because they are extremely bright (high quantum efficiency) and do not suffer from photo-bleaching like their fluorescent counterparts. In addition, they are sufficiently small (5-15 nm) that they can, like fluorescent dye molecules (1-4 nm), move around freely in the crowded intracellular environment. They are also reportedly nontoxic *in vivo* provided that the cellular environment is not illuminated by ultraviolet (UV) light. This can cause a breakdown of the surrounding shell which would allow toxic ions such as cadmium to leak out [68].

QDs have been used in single molecule experiments to provide information about the function of single molecules as well as the diffusion dynamics of cellular organisation [66]. They are also frequently used to track the *in vivo* delivery of drugs over extended time periods because of their resilient optical stability. For example, the tracking of QDs conjugated with tumour targeting anti-bodies to visualise cancerous tumours in living mice [69]. Single molecule studies offer additional information to the averaged ensemble behavior of molecules and are responsible for the huge growth in biophysics groups worldwide.

One less desirable property of QDs is the intermittency of their emission [70]. Blinking is effected by various physical parameters such as the excitation wavelength and the presence of reducing agents [71, 72] and need not necessarily be seen as a disadvantage. Blinking has been shown to allow the positional resolution of two closely spaced QDs by utilising the off period of one QD to obtain the point spread function, and hence the exact position, of the other [73].

6.3 Early experiments

6.3.1 Trapping quantum dots

The first attempts to trap QDs, within the optical tweezers group of The Niels Bohr Institute, were made back in 2006 and with mixed success. Samples were prepared by diluting colloidal CdSe-core QDs (Invitrogen, 655 nm emission wavelength) in filtered milli-pore water, giving final concentrations of $1/10^5$ and $1/10^6$ that of the bottle concentration. A perfusion chamber was made using one thick microscope objective slide and one thin cover slip. The sample was added to the perfusion chamber with the aid of the capillary forces and then sealed using silicon vacuum grease. The optical tweezers setup consisted of an inverted optical microscope (Leica, DMI6000, SP5 confocal) with mercury lamp for QD excitation, similar to that previously described in Section 1.3.1, but with additional confocal and fluorescence capabilities. The laser (Nd:YVO₄, Spectra Physics millennia, 5 W, 1064 nm) was expanded to overfill the back aperture of the objective, as was previously found to be an efficient method of trapping metallic nano-particles of a similar size [28]. Position detection was achieved using a quadrant photodiode (Hamamatsu, S5981), details of which can be found in Section 1.3.2.

Optical trapping is most efficient when the focus of the trap is close to the lower surface of the sample chamber because of the spherical aberrations present when an oil immersion objective lens is focussed into an aqueous solution. Therefore, there are two possible methods of approaching the problem of trapping an individual QD: one can use an oil objective lens (HCX, PL, APO, 100 \times , NA=1.4 oil CS) and a high concentration of QDs ($1/10^5$) so that the reduced probability of drawing a QD upwards into the trap, because of the traps proximity to the lower surface, is compensated for by the larger number of QDs in solution; or one can simply employ a water immersion objective, just as efficient when focussed deep into the sample chamber as it is when focussed near the lower surface, together with a smaller concentration of QDs ($1/10^6$). The disadvantage of using the oil objective lens is that it involves waiting a considerable time, up to ten minutes, for a QD to randomly diffuse into the trap but the advantage is that once in the trap, it takes a long time before an additional QD enters. A water objective, on the other hand, allows a QD to be quickly and easily drawn into the trap but then the problem is that so, too, are additional quantum dots from below the focus of the trap. Both methods were tried but *fishing* for QDs using the oil immersion objective became the preferred method because the oil immersion objective has a higher magnification and hence improved the likelihood that a trapped QD could be imaged. The importance of additionally expanding the trapping laser using a set of lenses to form a telescope before the trapping beam enters the microscope, as was reported to be important in the trapping of nano-sized gold colloids [28], is not clear here since it was also possible to trap QDs with a water objective lens without this expansion.

QDs were trapped with an output laser power of 525 mW, of which about 20 percent is estimated as reaching the focus. Experiments were made at a depth of $3\ \mu\text{m}$ from the lower surface, avoiding the need to consider Faxen's corrections for surface effects. Power spectra were then gathered for what were believed to be single quantum dots in the optical trap. Visualising QDs in the trap, however, proved extremely difficult because of their considerable *Brownian motion*. There is no doubt that QDs were trapped during these experiments, this was particularly evident when an aggregate of probably a few tens of QDs was seen to diffuse into the trap. A bright clump of fluorescence appeared on the CCD and the voltage signal from the quadrant photodiode increased drastically. However on the majority of occasions, although there was nothing visible in the trap, the power spectrum showed the presence of something that was nicely mapped by a Lorentzian function in the fitting software. Experiments where no QDs were present in the sample chamber did not show similar power spectra to those where QDs had been added, and when they did it was because there was some piece of dirt or something visibly present in the trap. The problem was that there was no way of knowing whether the observed power spectra belonged to individual QDs, or to aggregates of two or three quantum dots which would be equally invisible to detection.

6.3.2 Visualising quantum dots

In order to assess whether either of the two detection methods available (Confocal detection or detection by CCD and Fluorescence excitation) were capable of resolving a single QD in the trap, experiments were made to first visualise QDs that were stuck to the lower surface of the sample.

A dilution of quantum dots was prepared, as previously described, except that 25 mM Calcium Chloride was added before the mixture was perfused into the sample chamber. This caused a screening of the repulsive forces which normally exist at the glass surface and the quantum dots were abundantly attached to the surface, making visualisation considerably easier. A simple way of identifying an individual QD is to observe its emission frequency; if a QD is seen to blink then it is almost certainly a single QD because the ratio of the off state to the on state is extremely small. One can thus deduce that the probability of observing a dark state for an aggregate of two QDs is negligible since this would necessitate that both quantum dots were in their extremely improbable off states at the same time. The probability of observing an aggregate in a state of darkness is the probability of observing a single QD in an off state, to the power of the number of QDs in the aggregate. With this in mind, one can safely conclude that blinking is an excellent indication of an individual QD.

When the mercury lamp, a CCD camera and the appropriate filter cube were used, blinking was observed for almost all of the QDs attached to the surface. However, using

Leica's SP5 confocal system, QDs stuck to the glass surface were barely seen to blink. Images from fluorescence microscopy imaged by CCD were considerably better than those obtained using the confocal system. Figure 6.2 shows the view by CCD detection of blinking of quantum dots immobilised on the glass surface at different magnifications of zoom.

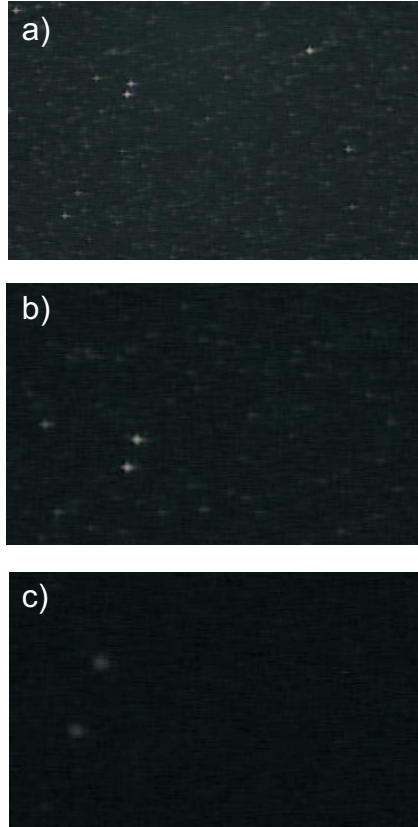


Figure 6.2: Blinking as observed using a standard CCD camera: a) fully zoomed out, b) at half zoom, and c) fully zoomed in. The two bright areas are aggregates but hopefully one can at least see the individual QDs as less intense areas in a). However, in b) it is more difficult to see the individual QDs and in c) one can only see the two aggregates. The original images are much better than how they appear in this figure and as such even the two aggregates in c) are difficult to see.

Immobilised QDs are visible when the optical zoom (Leica, $1.6\times$) is employed to focus in on an individual QD, right up until the last turn on the zoom. The intensity of a blinking QD becomes less and less as the zoom is increased because the amount of light collected in the reduced area after zooming is insufficient to image a single quantum dot. Confocal imaging of a blinking quantum dot is extremely restrictive. Figure 6.3 shows a series of images of a blinking QD, after employing the digital zoom in the confocal software, but even with optimised settings there is still a very poor signal to noise ratio (SNR).

Diverging slightly, a quick experiment was made to see if any of the blinking QDs could be forcedly removed from the surface and into the trap. Unsurprisingly, the QD was more

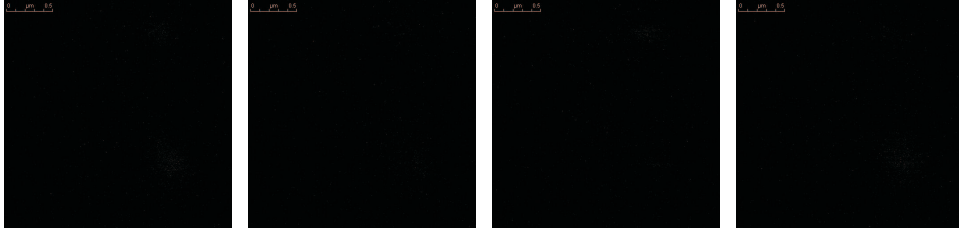


Figure 6.3: The QD is a regular accumulation of intensity in the upper right hand corner of the image. It is difficult to decipher from the background noise.

tightly bound to the glass surface than the maximum force which could be applied by optical tweezers, even at considerable laser power ($\gg 1W$). This could, unfortunately, only be attempted while imaging with the confocal microscope because at that time the trapping laser was coupled to the microscope by a mirror positioned in the bright field position.

The same experiment using CCD detection and fluorescence could only have been facilitated if the optical trap entered the microscope via the fluorescent port, which would have meant considerable realignment. Major modifications to the experimental setup were not practical at that time and any attempts to image a QD in the optical trap were restricted to confocal imaging. The SNR of an immobilised single QD viewed with the confocal microscope was so bad that the likelihood of observing a quantum dot undergoing significant *Brownian motion* in the optical trap can be only be summarised as zero. Locating and imaging a QD stuck to the surface was difficult enough with the confocal microscope, without contending with more difficult experimental conditions, but supposing high quality imaging and optical trapping could be combined, would the observed intensity fluctuations of a blinking QD in an optical trap be distinguishable from the mere axial diffusion of a QD in and out of the focal volume?

The investigation was abandoned until the coexistence of fluorescence microscopy and optical trapping could be achieved. The optical techniques required to perform such an experiment are a fast scanning confocal microscope or an electron-multiplying charge coupled device (EMCCD).

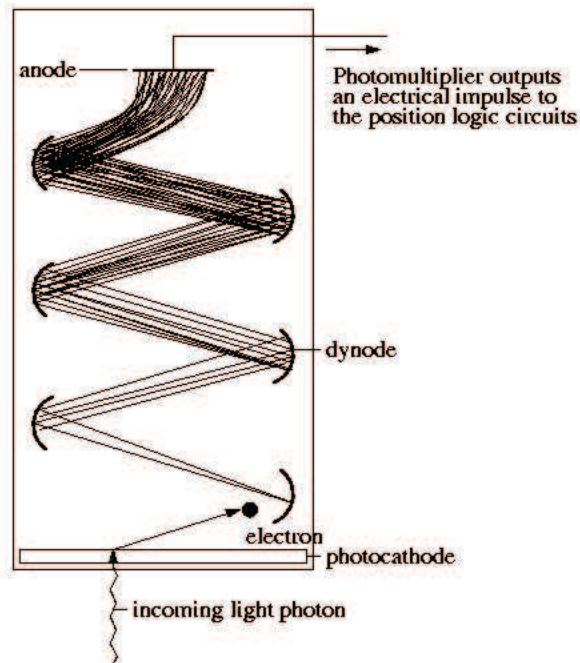
6.4 Improvements to the experimental setup and procedure

6.4.1 The EMCCD alternative

An electron multiplying charge coupled device (Ixon, Andor Technology) offers additional sensitivity (SNR) over a standard charge coupled device (CCD) by diverting electrons through a series of pre-detection gain sections. It operates rather like an avalanche photodiode (APD); an electron is passed through a region of high voltage (gain section) in which a single electron can induce several additional electrons by impact ionisation. The additional

electrons created can then go on to induce further collisions in the many gain sections of the device, creating an avalanche of electrons from that first single electron. The innovative thing about this multiplication process is that, by making the probability of gain in each region very low but employing a large number of gain elements, the overall gain of the device for an electron which entered the system at the first gain region is high. Any noise arising during or after electron multiplication will consist of a significantly lower number of electrons and thus the readout noise is negligible.

Cooling the chip of the EMCCD camera to -80°C is necessary when the electron-multiplying gain function is employed because additional noise from thermal electrons are also multiplied and substantially degrade the device performance.



A Photomultiplier Tube

Figure 6.4: The figure shows the multiplication process of an avalanche photodiode which operates in a similar fashion to an EMCCD. Figure downloaded at <http://www.zmb.uzh.ch/resources/download/CLSM.pdf>.

Figure 6.4 shows the multiplication process inside an avalanche photodiode capable of detecting single photons. This is very similar to the operation of an EMCCD where there are multiple gain regions each providing moderate gain.

6.4.2 Buffer optimisation

Upon re-starting experiments to trap quantum dots, L. Jauffred decided to dilute the QDs in a buffer recommended by Chris Lagerholm's group who actively work with the same QDs as used in this investigation. The buffer (1 M sodium Borate with 1 percent Bovine Serum Albumin (BSA), pH 8.2) enhances the contrast of the QDs in solution [74]. Instead of diluting QDs in filtered millipore water, all subsequent dilutions were made in this buffer thus making the quantum dots more distinguishable.

6.4.3 Reducing the axial movement of the quantum dot by compensating for spherical aberrations

In order to maximise the probability of seeing a quantum dot performing *Brownian motion* within the trap, I wanted to employ a novel method of compensating for spherical aberrations [14], already familiar from a previous investigation within the group (Chapter 2). This method increases the axial trap stiffness and results in a greater confinement of the trapped particle in the axial direction, thus decreasing the time period where a quantum dot would be out of the focal region of the detection system.

6.5 Experimental procedure

With the improvements described in Section 6.4 in place, further experimental attempts could be made to trap and visualise individual QDs. However first of all, QDs that were stuck to the lower surface of the sample were investigated using only the EMCCD and the more optimal buffer conditions. These changes were found to be positive and the stationary quantum dots were highly visible using the EMCCD and optical zoom (Leica, $1.6\times$). On the contrary, experiments to visualise quantum dots in the optical trap were hampered by the substitution of a standard immersion oil for an immersion medium that reduces spherical aberrations ($n = 1.54$). The immersion medium was found to be highly auto-fluorescent and any improvement offered by an increased axial confinement of the quantum dot was dwarfed by the extreme degradation in visibility caused by the background fluorescence from the oil. Experiments were, thereafter, conducted using a standard immersion oil (Leica, $n = 1.518$) and oil immersion objective lens (Leica, $100\times$, $NA = 1.4$).

6.5.1 Pressing a trapped quantum dot onto the lower glass surface of the sample, under high salt concentrations

To begin with, optical trapping was still only available while operating the microscope in bright field mode. Therefore, an image of the glass surface was made before the start of the experiment using fluorescent microscopy and the EMCCD, as a control method to show that there were no QDs attached to the surface. The microscope was then moved into

bright field mode and the optical tweezers focussed $3\ \mu\text{m}$ from the sample surface using the same experimental procedure described in Section 6.3.1. That ensured that spherical aberrations were kept to a minimum and the best possible conditions for trapping a single QD were in place, for this experimental configuration. Once the quadrant photodiode suggested that a QD was in the trap, power spectra were gathered. Later, the focus of the trap was slowly lowered so that the QD would touch the lower surface of the sample chamber. The microscope was then returned to the fluorescence setting and another image acquired. The intention was that in performing this experiment at a whole host of different salt concentrations, the quantum dot would eventually stick and a blinking quantum dot would be left on the lower surface of the sample.

Unfortunately, this proved rather unsuccessful for a multiple number of reasons. Firstly, the experimental setup was not suited to this experiment; it would have been much easier if the experiment had been carried out entirely under fluorescence conditions. Pressing the quantum dot down onto the surface in real time would mean that any sudden flash of fluorescence was a good indication that the quantum dot had escaped the trap back into solution because of the approaching surface. Furthermore, one could not be sure exactly where the surface was since the only indication that the surface had been reached was the disappearance of the voltage signal from the quadrant photodiode. Lastly, increasing the salt concentration was time consuming and rather 'bistable'; quantum dots were either all in solution or all stuck to the surface. Finding the perfect salt concentration, where a QD could be attached to the surface only by pressing it down on the surface, proved to be an experiment in itself. It could also be that the BSA in the optimised buffer helps to screen the non-specific attachment of the QDs to the surface.

However, these experiments did serve as an excellent method of gathering quantitative information on trapped quantum dots. The numerous number of power spectra taken of quantum dots in the trap could later be used to build a statistical argument that individual quantum dots had been trapped.

On the grounds of the problems encountered with the experiments detailed in this section, and in the interest of another project requiring simultaneous fluorescence microscopy and optical tweezers, optical tweezers were incorporated into the microscope via the fluorescence port. This was carried out by L. Jauffred, with some help and advice from myself, and created the opportunity to possibly see a QD within the optical trap. During the course of re-integrating optical tweezers into the confocal microscope, L. Jauffred had the idea of simplifying the attachment of a QD to the surface by employing the specific binding of Biotin and Streptavidin.

6.5.2 Using Streptavidin coated quantum dots for specific binding to a biotin coated glass surface

Quantum dots that were identical in composition and size to those used in the previous experiments, now with a Streptavidin coating instead of a stabilising polymer coating like polyethylene glycol (PEG), were used in the optical trapping experiments. The lower glass cover slip was prepared with a thin surface coating of Biotin by incubating overnight with BSA-Biotin (Sigma) in 20 mM Na₂ HPO₄, 150 mM NaCl (pH 7). A schematic of the experimental process is shown in Figure 6.5.

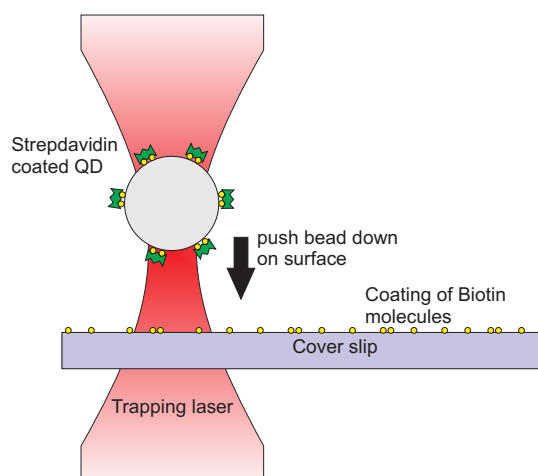


Figure 6.5: The specific attachment of a streptavidin coated QD to a biotinylated cover slip is shown schematically with the lock and key principle of specific binding. The schematic drawing is not to scale.

Biotin and streptavidin are frequently used in biophysics experiments because they produce an extremely strong bond when brought together. It is also a specific binding event and is not effected by the presence of other molecules. Trapping a streptavidin coated QD from within the perfusion chamber and pushing it down against the biotinylated coverslip, as shown in Figure 6.5, provides a robust and reproducible method of immobilising the trapped QD or QDs held in the optical trap. Examination of the surface of the coverslip afterwards was used to determine whether a single QD had actually been trapped.

6.6 Results

6.6.1 Trapping of individual quantum dots; a statistical argument

The trapping laser light that is scattered in the forward direction, by a QD diffusing in the trap, is gathered by a quadrant photodiode (QPD) positioned at the back focal plane. The raw signal of the QPD is shown in Figure 6.6, for an increasing number of QDs in the trap.

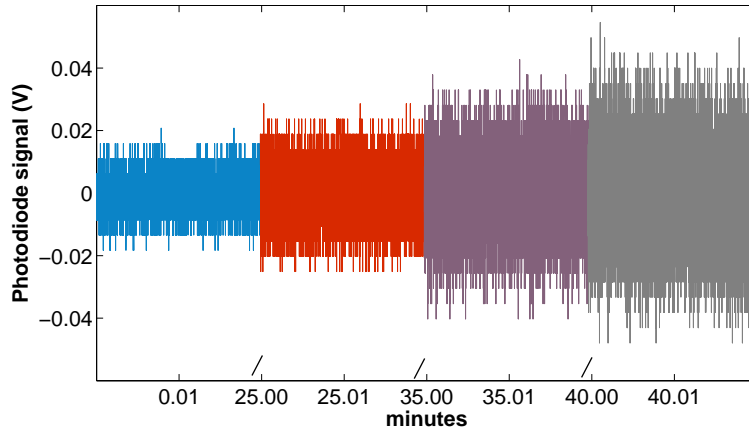


Figure 6.6: A time series of the photodiode signal shows the broadening that occurs as additional QDs are pulled into the trap. With one QD in the trap (Blue), the photodiode signal is directly correlated to the position of the QD. However, once a second QD enters the trap (red), the signal from the photodiode no longer translates to particle position. Approximately every 10 mins, another QD enters the trap which is evident by the further broadening of the signal in the purple and grey traces.

Broadening of the time series in an investigation to trap gold colloids was shown to correlate well with the entry of additional particles into the optical trap [28]. Broadening of the QPD signal in Figure 6.6 is thus assumed to be the signature of additional QDs entering the trap. Figure 6.7 shows the corresponding histograms of the QPD signals shown in Figure 6.6. As the number of QDs in the trap increases, so too does the width of the distribution.

The significance of these two figures is that they prove single QDs were trapped for at least 10 minutes, during which time the distribution of the QPD signal is narrow and translates directly to positions visited by the lonely QDs. Therefore, a calibration of the optical spring constant which quantifies the range of optical forces that can be applied to these semiconductor nano-crystals, could be facilitated for the first time (Section 6.6.3).

6.6.2 Trapping of individual quantum dots; visual verification by blinking

A second method to confirm that a single QD had been trapped was to press a trapped Streptavidin coated bead down onto a biotinulated surface so that the QD could be specifically bound, allowing observation of the characteristic blinking that only single QDs display. The sample surface, in the region beneath the focus of the optical trap, is shown before (Figure 6.8(a)) and after (Figure 6.8(b)) the trapped QD is lowered onto the surface. Another QD was present on the surface before the experiment began but lay far enough away from the trapping position that it was not problematic.

Figure 6.8 clearly shows that an additional QD is attached to the surface after the focus

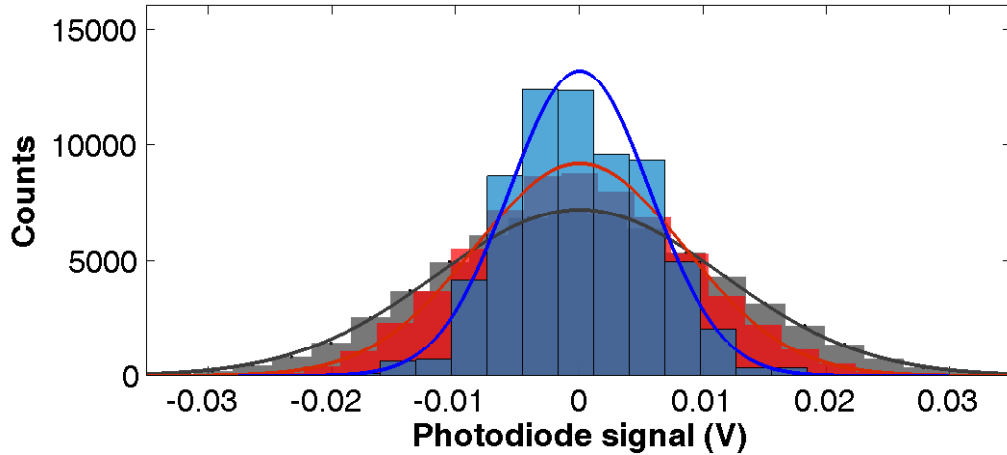


Figure 6.7: Histograms for three of the four QPD signals seen in Figure 6.6 are shown. The first histogram (Blue) indicates the distribution in positions visited by a single QD within the trap. Solid lines represent *Gaussian* fits of the distributions. Once more than one QD is trapped, the distribution will no longer translate to particle position. The red and grey histograms show the broadening that occurred when two and four QDs were trapped, respectively.

of the trap is lowered to the surface, over and above that which was already attached to the surface some distance away from the trapping position.

Film sequences of the newly deposited QD were analysed as previously reported [73] but instead using a homemade MatLab program (L. Jauffred). The goal of this analysis was to verify that a solitary QD had, indeed, been attached. The temporal evolution in intensity of the attached QD (Figure 6.9(a)) and a histogram of the intensity distribution (Figure 6.9(b)) were produced in the hope that two distinct states, *on* and *off*, would be observed.

The two peaks seen in the histogram of Figure 6.9(b), confirm the individuality of the attached QD because the two state characteristics of a blinking QD are revealed; the attached QD is either in an emitting state, or in a non-emitting state. This provides a separate and independent verification of the conclusion made in Section 6.6.1, that a single QD is trapped by a continuous wave laser with an estimated power at the focus of a little over 100 mW.

6.6.3 Optical trap stiffness, κ , of a trapped QD

Optical tweezers are generally assumed to exert a harmonic restoring force on particles displaced from trap centre, provided that the displacement is caused by *Brownian motion*

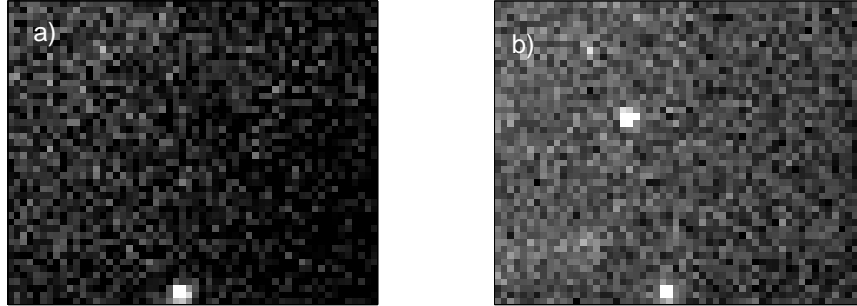


Figure 6.8: Images of the biotinylated surface under the optical trap: (a) the surface prior to trapping a Streptavidin coated QD; (b) the same region after a trapped Streptavidin coated QD is pressed against the surface and attached. The images encompass several *on* states of the QDs by integrating the intensity over a 1.8 s exposure time.

of the particle (Chapter 2 discusses the merits of this in more detail). In the case of a trapped QD, the assumption is valid and the optical restoring force is characterised by the spring constant or trap stiffness, κ . The equation of motion of a particle undergoing *Brownian motion* in an optical trap is defined by the Langevin equation which, after Fourier transformation, gives a positional power spectrum that is well described by a Lorentzian function. The spring constant can be determined using the result of this fit. (See Section 1.3 for a thorough discussion).

Fitting the power spectrum requires certain input parameters such as the radius of the trapped particle. The elliptical shape and dimensions of the colloidal QDs used in this study were accurately depicted in Figure 6.1. However, in order to simplify calibration, the QDs were assumed to be spheres with effective radii of 15 nm, approximating somewhat the true dimensions of the QDs. One of the 30 data sets analysed is shown in Figure 6.10, where the solid line represents the best fit by a Lorentzian function assuming a QD radius of 15 nm. The fitting also considers effects like filtering of the QPD [75] and aliasing [76].

The corner frequency found from the Lorentzian fit was 180 Hz and the average spring constants (30 data sets) in the two lateral directions were $(2.2 \pm 0.7) \times 10^{-7}$ N/m and $(2.6 \pm 0.6) \times 10^{-7}$ N/m for κ_x and κ_y , respectively. These findings are in agreement with the trapping of metallic nano-particles such as gold and silver, where similar spring constants

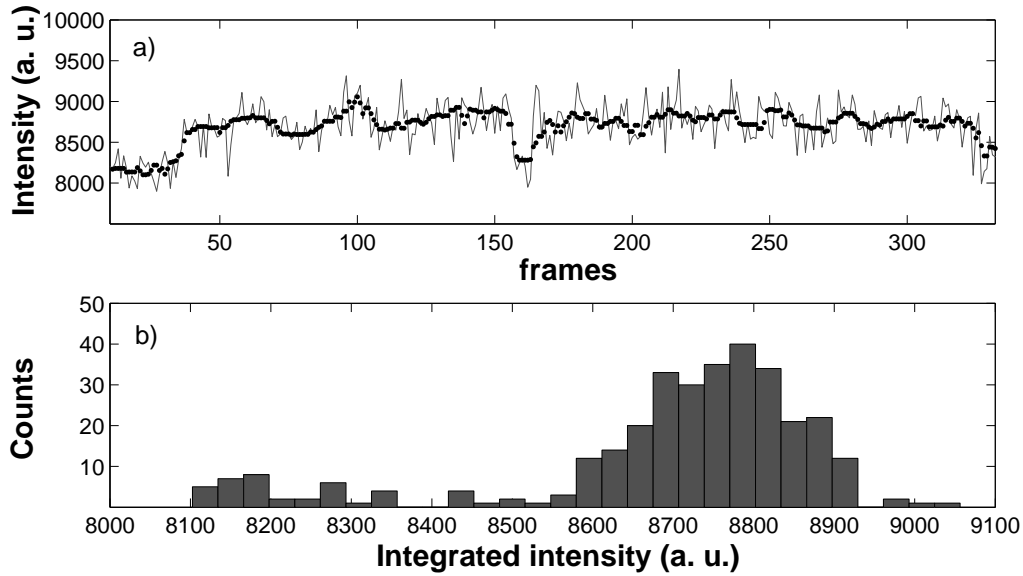


Figure 6.9: (a) The intensity fluctuations of the attached QD from Figure 6.8(b), are shown in a plot of intensity vs. time, where the dots represent the average of a sliding window of 10 data points and the continuous line is the raw data. (b) The corresponding intensity distribution histogram shows bistable emission, trademark of a single blinking QD.

were reported [28, 77]. For example, a gold nano-particle of radius 15 nm was trapped with a lateral spring constant of 5×10^{-4} pN/nm for the same laser output power (525 mW)[28]. This is double the spring constant of an equivalently sized QD (2.4×10^{-4} pN/nm). However, if one also considers that the comparison is made with data from a study [28] where type 1 cover slips were mistakenly used with an oil immersion objective designed for type 1.5 cover slips, then the comparison is slightly flawed since during this study of trapping QDs the correct type 1.5 cover slips were used. With this in mind, perhaps a more realistic comparison would be to say that the equivalent sized gold nano-particle is trapped with a spring constant of approximately 5-10 times that of a QD.

Interestingly, this suggests that the induced dipole of a QD is considerably smaller than an equivalently sized metallic nano-particle. One possible reason for this could be that, unlike the metallic nano-particles, 1064 nm light is moderately absorbed by a QD. This is the basis of a current investigation within the group in which two photon excitation of the QDs can be readily seen when they are trapped using 1064 nm light i.e. the assumption that the absorption coefficient of a QD is negligible for infra-red light is flawed.

6.6.4 The inferred properties of a quantum dot

Having quantitatively measured the lateral spring constant of a trapped QD, it was possible to approximate the polarsibility by making a few assumptions as was done in the published

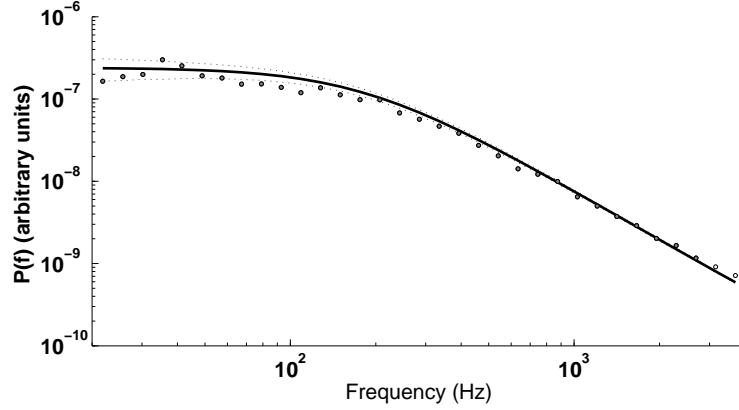


Figure 6.10: The power spectrum of positions visited by an optically trapped QD in an orthogonal direction to the trapping laser beam. The full line is a Lorentzian fit to the data and the dashed lines represent the error bars. The corner frequency of the Lorentzian fit was 180 Hz.

version of this work [39]. Firstly, the intensity profile of the laser beam is considered Gaussian in both the lateral directions and is described as follows:

$$I = I_0 e^{-(x^2+y^2)/2\sigma^2}. \quad (6.1)$$

where σ is the standard deviation of the intensity distribution.

The total optical power, \mathcal{P} , delivered to sample equals the integrated intensity:

$$\mathcal{P} = \int_{-\infty}^{\infty} I dx dy = I_0 2\pi\sigma^2. \quad (6.2)$$

In one dimension the gradient force is [78]

$$\vec{F}_{grad} = \frac{\alpha}{2} \nabla(\vec{E}^2), \quad (6.3)$$

where α is the polarisability.

Only the real part of the polarisability was used in Equation 6.3. The imaginary part of α , the absorption, is assumed considerably smaller than the real part. This was before the considerable two photon absorption of QDs was discovered [79] and in any case, it would not be straightforward to include this term and may well overly complicate this first estimation of α .

The electric field, \vec{E} , is related to the intensity by:

$$|E|^2 = 2I/c\epsilon, \quad (6.4)$$

where c is the speed of light in a vacuum and ε is the electric permittivity of the medium. The permittivity of water at a wavelength of 1064 nm is $\varepsilon = 1.32^2 \times \varepsilon_0$ [80], where $\varepsilon_0 = 8.854 \times 10^{-12} \text{ C}^2/\text{Vm}$.

For such a small particle trapped with a wavelength of 1064 nm, far above the emission wavelength of the QD (655 nm), the contributions of \vec{F}_{scat} and \vec{F}_{abs} are very small in comparison to the contribution of \vec{F}_{grad} [78]. The trapping force is thus approximated as $\vec{F} = -\kappa \vec{x} = \vec{F}_{grad}$.

Knowing the optical power used in the experiments, \mathcal{P} , and the average value of κ determined by calibration, the above equations are used to give a rough calculation of the polarisability, α , by combining equations 6.1, 6.2, 6.3, and 6.4 and Taylor expanding for small x while comparing equation 6.3 to $\vec{F}_{grad} = -\kappa \vec{x}$ resulting in:

$$\alpha = \frac{2\pi c \kappa \varepsilon}{P} \times \sigma^4 = (6.4 \times 10^{-8}) \frac{\text{C}}{\text{Vm}^2} \times \sigma^4 = (2.5 \times 10^{-34}) \frac{\text{C}}{\text{V}} \text{m}^2. \quad (6.5)$$

In this case, the radius of the focussed laser beam at the trap centre, σ , is approximated as [78], $\sigma \sim 250 \text{ nm}$. Upon normalisation with the free space permittivity, ε_0 , the polarisability $\frac{\alpha}{\varepsilon_0}$ is $2.8 \times 10^7 \text{ \AA}^3$.

As one can see from Equation 6.5, α is strongly dependent on the value of σ and because σ is only a rough estimation, the resulting value for the polarisability may well be an order of magnitude out. This can be more readily seen from the predictions of Figure 6.11, wherein the value of $\frac{\alpha}{\varepsilon_0}$ for different choices of σ is mapped.

The polarisability of a dielectric sphere is more commonly estimated using the Clausius-Mossotti relation. This necessitates the assumption that the CdSe core of the QD is approximately spherical, contrary to the fact that the core is specified as being elliptical by Invitrogen. However, transmission electron microscopy (TEM) images of several different types of QDs show that the overall shape including shell is mainly spherical but with a few ellipses and other oddly shaped structures. Figure 6.12 shows typical images of a few different QD assays.

For the purpose of the Clausius-Mossotti calculation of polarisability, a sphere of radius, $r_{core} = 5 \text{ nm}$ is assumed:

$$\frac{\alpha}{\varepsilon_0} = 3V \frac{\epsilon_{qd} - \epsilon}{\epsilon_{qd} + 2\epsilon} = 9.6 \times 10^5 \text{ \AA}^3. \quad (6.6)$$

Where $\epsilon = \frac{\varepsilon}{\varepsilon_0}$ is the square of the refractive index, $\epsilon_{qd}=10$ for CdSe and $\epsilon = 1.74$ [80] for water at 1064 nm.

This value is two orders of magnitude smaller than the polarisability deduced on the basis of the experimentally obtained values of κ . Therefore, the approximation of a QD with an elliptical core of $6 \text{ nm} \times 12 \text{ nm}$ as a simple dielectric sphere of CdSe with a radius of 5 nm appears to be inappropriate. The polarisability given by Clausius-Mossotti would be larger if the surrounding shell and polymers were also considered since there is a cubic

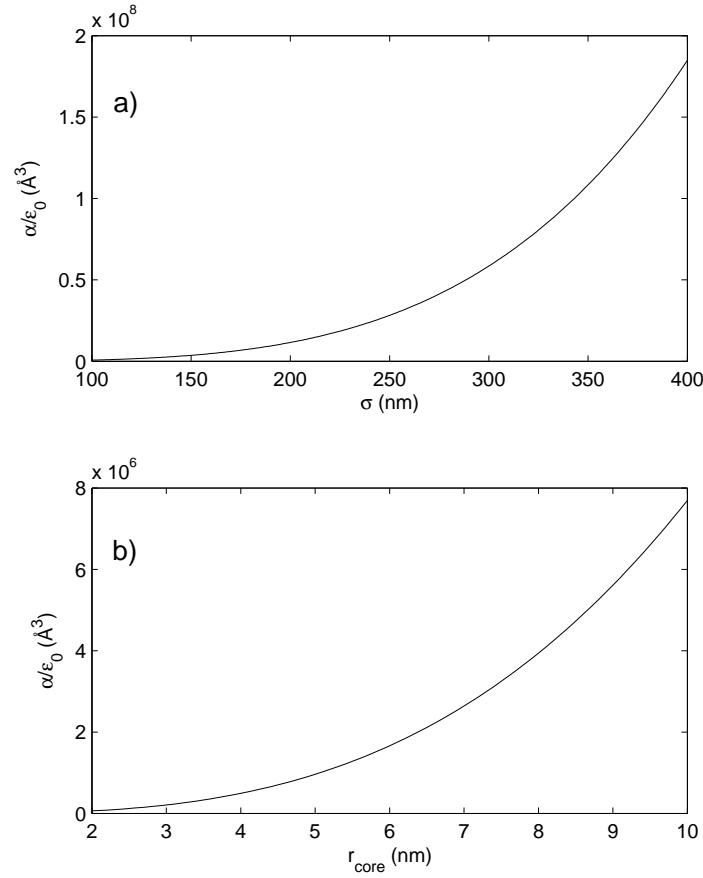


Figure 6.11: The effect of estimating the radius of the trapping beam, σ , and the diameter of the QD core, included in V , upon the polarisability, $\frac{\alpha}{\epsilon_0}$, can be seen in a) and b), respectively. In a) the value of $\frac{\alpha}{\epsilon_0}$ is based on the measured value of k from experiments and in b) the value of $\frac{\alpha}{\epsilon_0}$ is calculated using the Clausius-Mossotti relation.

dependence of the polarisability on the sphere radius. Furthermore, experience of trapping other asymmetric particles such as gold nano-rods [81] would suggest that the QD probably aligns with its major axis lying orthogonal to the propagation direction of the laser. Therefore, the dipole volume would be better approximated by assuming a radius closer to the dimension of the larger of the two axes, 12 nm, which would actually bring the two estimated values of polarisability closer together. Figure 6.11 also shows how an increase in the assumed core radius effects the resulting calculation of polarisability, $\frac{\alpha}{\epsilon_0}$.

It is hard to make any solid conclusions from these two calculations but it would seem that the polarisability found using the experimentally determined value of κ agrees roughly with that found theoretically using the Clausius-Mossotti relationship. There are, however, considerable uncertainties in the determined values of both calculations because of the

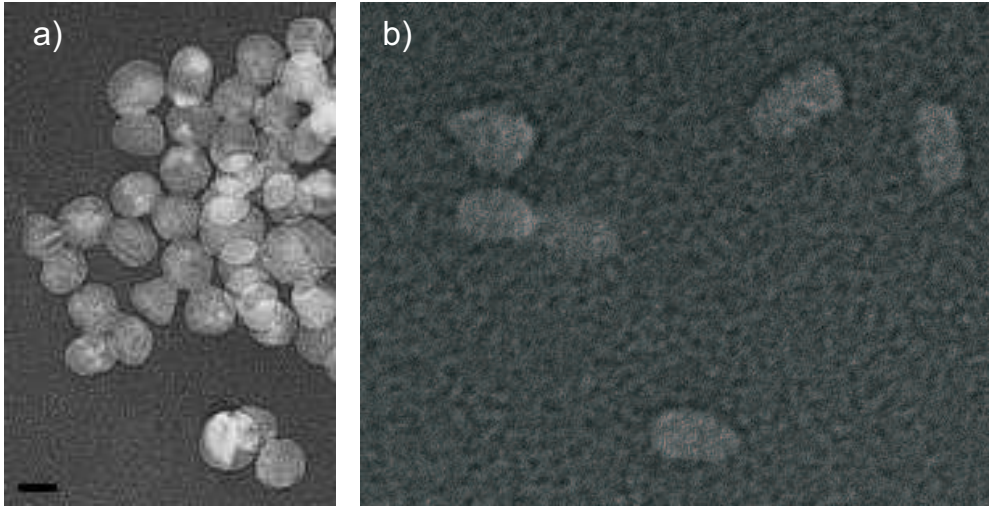


Figure 6.12: TEM images of the two types of QDs used in this investigation are shown, a) 605 nm, and b) 655 nm emission wavelength, where the scale bar in a) represents a distance of 10 nm. The 605 nm and 655 nm QDs are reported by Invitrogen to have elliptical core diameters of 4×9.4 and 6×12 , respectively, while maintaining an overall shape that is approximately spherical. TEM images reveal that the combined shape of the core/shell is approximately spherical for the 605 nm QDs (a), but that the QDs with an emission wavelength of 655 nm (b), have an overall shape that is extremely ellipsoidal. Pictures courtesy of the group's laboratory technician, Inger Jensen.

power 4 dependency and the cubic dependency of the assumed beam radius at trap centre, σ in Equation 6.5, and the assumed 5 nm spherical core radius of pure CdSe, within V of Equation 6.6, respectively.

6.7 Future experiments

The optical confinement of a single quantum dot was demonstrated by two separate methods in this study, but visualisation of a quantum dot in the trap is still elusive. Achieving this feat would permit many of the loitering questions about the physical properties of quantum dots to be answered. For example, the polarisability, polarisation dependency or possibly even the refractive index.

The recent procurement of an immersion medium with no autofluorescence and a refractive index ($n = 1.538$) similar to that proven to cancel spherical aberrations [14] ($n = 1.54$), may allow such experiments to be undertaken. This is the subject of a current investigation within the group.

6.8 Summary

The trapping of individual quantum dots has been proven by two independent methods and the relevant trap stiffness for both directions orthogonal to laser propagation determined. Based on this calibration, estimated forces of up to a 20 pN could be exerted on a QD and which would possibly allow manipulation or observation of organelles within a cell undergoing cell division. For example, genetically modified strains of *S. pombe* that express green fluorescent protein (GFP) in specific organelles of the cell could be used in conjunction with micro-injected, anti-GFP coated, quantum dots to investigate the microrheology of the intracellular space during cell division.

However, QDs were found to have smaller dipoles than similarly sized silver or gold particles which make them less favourable for *in vivo* experiments to measure the forces involved in cell division. QDs are also often elliptical and their properties are far less established than gold. On the other hand, they do have the considerable advantage that they are extremely visible and, when bound to an organelle, it would be simple to verify their individuality by their blinking.

Conclusions & outlook

This PhD dissertation had the overall goal of investigating the *in vivo* cell mechanics of *S. pombe* fission yeast. Progress was made along several lines of research, and thereby a sound basis from which to go on and investigate *in vivo* cell mechanics has been established: an *in situ* calibration method was experimentally proven to operate well in a viscoelastic medium, confocal-tweezers combining quantitative force measurement and 2D confocal scanning were created, a popular *in vivo* probe (QD) was optically trapped and shown to be manipulable at bio-relevant forces, the force-displacement relationships of optically trapped polystyrene beads of a size similar to that used in DNA stretching experiments were quantified at extreme positions, and finally the micro-injection of our cellular system of choice with a membrane impermeable dye was made in a proof of concept experiment.

There are many ways in which this research could be continued in the future; inserting gold nano-particles into *S. pombe* protoplasts and regenerating the selfsame protoplasts back into healthy cells would be one such avenue, so too would be to test the FDT calibration method in the cytosol of a living cell, or to establish a system of 3D confocal-tweezers. The first of these could already be achieved if the cellular system of choice, *S. pombe*, were replaced by a larger plant cell. Having first established a protocol for how one should go about investigating intracellular processes/ cell division by testing the performance of the calibration method in an environment where one can easily insert gold nano-probes, it would then be easier to attempt the same experiments in a smaller, more complex cell type.

Bibliography

- [1] C. Asbury, A. Fehr, and S. Block, “Kinesin moves by an asymmetric hand-over-hand mechanism,” *Science* **302**, pp. 2130–2134, 2003.
- [2] M. Dogterom, J. Kressmakers, G. Romet-Lemonne, and M. Janson, “Force generation by dynamic microtubules,” *Current Opinion in Cell Biology* **17**, pp. 67–74, 2005.
- [3] M. Fischer and K. Berg-Sørensen, “Calibration of trapping force and response function of optical tweezers in viscoelastic media,” *Journal of Optics A: Pure and Applied Optics* **9**, pp. S239–S250, 2007.
- [4] A. Ashkin, “Acceleration and trapping of particles by radiation pressure,” *Physical Review Letters* **24**, pp. 156–159, 1970.
- [5] A. Ashkin, J. Dziedzic, J. Björkholm, and S. Chu, “Observation of a single-beam gradient force optical trap for dielectric particles,” *Optics Letters* **11**, pp. 288–290, 1986.
- [6] A. Ashkin and J. Dziedzic, “Optical levitation by radiation pressure,” *Applied Physics Letters* **19**, pp. 283–285, 1971.
- [7] A. Ashkin, “Forces of a single-beam gradient laser trap on a dielectric sphere in the ray optics regime,” *Biophysical Journal* **61**, pp. 569–582, 1992.
- [8] P. Prentice, M. MacDonald, T. Frank, A. Cuschieri, G. Spalding, W. Sibbett, P. Campbell, and K. Dholakia, “Manipulation and filtration of low index particles with holographic Laguerre-Gaussian optical trap arrays,” *Optics Express* **12**, pp. 593–600, 2004.
- [9] K. König, H. Liang, M. Berns, and B. Tromberg, “Cell damage in near-infrared multi-mode optical traps as a result of multiphoton absorption,” *Optics Letters* **21**, pp. 1090–1092, 1996.
- [10] P. Celliers and C. J., “Measurement of localized heating in the focus of an optical trap,” *Applied Optics* **39**, pp. 3396–3405, 2000.

BIBLIOGRAPHY

- [11] Y. Seol, A. Carpenter, and T. Perkins, “Gold nanoparticles: enhanced optical trapping and sensitivity coupled with significant heating,” *Optics Letters* **31**, pp. 2429–2431, 2006.
- [12] R. Gussgard, T. Lindmo, and I. Brevik, “Calculation of the trapping force in a strongly focused laser beam,” *Journal of the Optical Society of America B: Optical Physics* **9**, pp. 1922–1930, 1989.
- [13] K. Berg-Sørensen and H. Flyvbjerg, “Power spectrum analysis for optical tweezers,” *Review of Scientific Instruments* **75**, pp. 594–612, 2004.
- [14] S. Reihani and L. Oddershede, “Optimizing immersion media refractive index improves optical trapping by compensating spherical aberrations,” *Optics Letters* **32**, pp. 1998–2000, 2007.
- [15] I. Vladescu, M. McCauley, M. Nuñez, I. Rouzina, and M. Williams, “Quantifying force-dependent and zero-force DNA intercalation by single-molecule stretching,” *Nature* **4**, pp. 517–522, 2007.
- [16] F. Marena, G. Boer, J. Rohner, G. Delacretaz, and R. Salathe, “Escape trajectories of single-beam optically trapped micro-particles in a transverse fluid flow,” *Optics Express* **14**, pp. 1685–1699, 2006.
- [17] Z. Gong, Z. Wang, Y. Li, L. Lou, and S. Xu, “Axial deviation of an optically trapped particle in trapping force calibration using the drag force method,” *Optics Communications* **273**, pp. 37–42, 2007.
- [18] S. Kuo and M. Sheetz, “Force of single kinesin molecules measured with optical tweezers,” *Science* **260**, pp. 232–234, 1993.
- [19] S. Sato, M. Ishigure, and H. Inaba, “Optical trapping and rotational manipulation of microscopic particles and biological cells using higher-order mode Nd-YAG laser-beams,” *Electron Letters* **27**, pp. 1831–1832, 1991.
- [20] E. Fällman and O. Axner, “Influence of a glass-water interface on the on-axis trapping of micrometer-sized spherical objects by optical tweezers,” *Applied Optics* **42**, pp. 3915–3926, 2003.
- [21] A. Rohrbach and E. Stelzer, “Trapping forces, force constants, and potential depths for dielectric spheres in the presence of spherical aberrations,” *Applied Optics* **41**, pp. 2492–2507, 2002.
- [22] K. Neuman and S. Block, “Optical trapping,” *Review of Scientific Instruments* **75**, pp. 2787–2809, 2004.

-
- [23] M. Wang, H. Yin, R. Landick, J. Gelles, and S. Block, “Stretching DNA with optical tweezers,” *Biophysical Journal* **72**, pp. 1335–1346, 1997.
- [24] D. Ganic, X. Gan, and M. Gu, “Exact radiation trapping force calculation based on vectorial diffraction theory,” *Optics Express* **12**, pp. 2670–2675, 2004.
- [25] D. Appleyard, K. Vandermeulen, H. Lee, and M. Lang, “Optical trapping for undergraduates,” *American Journal of physics* **75**, pp. 5–14, 2007.
- [26] A. Rohrbach, “Stiffness of optical traps: Quantitative agreement between experiment and electromagnetic theory,” *Physical Review Letters* **95**, pp. 168102–1 – 168102–4, 2005.
- [27] M. Speidel, A. Jonáš, and E. Florin, “Three-dimensional tracking of fluorescent nanoparticles with subnanometer precision by use of off-focus imaging,” *Optics Letters* **28**, pp. 69–71, 2003.
- [28] P. Hansen, V. Bhatia, N. Harrit, and L. Oddershede, “Expanding the optical trapping range of gold nanoparticles,” *Nano Letters* **5**, pp. 1937–1942, 2005.
- [29] K. Svoboda, C. Schmidt, B. Schnapp, and S. Block, “Direct observation of kinesin stepping by optical trapping interferometry,” *Nature* **365**, pp. 721–727, 1993.
- [30] F. Gittes and C. Schmidt, “Signals and noise in micromechanical measurements,” *Methods in Cell Biology* **55**, pp. 129–156, 1998.
- [31] W. Smith, *Modern Optical Engineering - the design of optical systems*, McGraw-Hill, New York, 3rd ed., 2000.
- [32] D. Boal, *Mechanics of the cell*, Cambridge University Press, New York, 4th ed., 2006.
- [33] I. Tolić-Nørrelykke, L. Sacconi, G. Thon, and F. Pavone, “Positioning and elongation of the fission yeast spindle by microtubule-based pushing,” *Current Biology* **14**, pp. 1181–1186, 2004.
- [34] J. Scholey, I. Brust-Mascher, and A. Mogilner, “Cell division,” *Nature* **422**, pp. 746–752, 2003.
- [35] L. B. Oddershede, 2006. Private communication, funding application.
- [36] P. M. Hansen, *Cellular mechanics studied by novel nano-tools and reconstituted model systems*. PhD thesis, Niels Bohr Institute, Copenhagen University, Copenhagen, Denmark., December 2006.

BIBLIOGRAPHY

- [37] P. Hansen and L. Oddershede, "Optical trapping inside living organisms," in *Optical Trapping and Optical Micromanipulation II*, K. Dholakia and G. C. Spalding, eds., *Proc. SPIE* **5930**, pp. 593003–(1–9), 2005.
- [38] I. Tolic-Nørrelykke, E.-L. Munteanu, G. Thon, L. Oddershede, and K. Berg-Sørensen, "Anomalous diffusion in living yeast cells," *Physical Review Letters* **93**, pp. 078102–(1–4), 2004.
- [39] L. Jauffred, A. Richardson, and L. Oddershede, "Three-dimensional optical control of individual quantum dots," *Nano Letters* **8**, pp. 3376–3380, 2008.
- [40] B. Dubertret, P. Skourides, D. Norris, V. Noireaux, A. Brivanlou, and A. Libchaber, "In vivo imaging of quantum dots encapsulated in phospholipid micelles," *Science* **98**, pp. 1759–1762, 2002.
- [41] C. Jarzynski, "Nonequilibrium equality for free energy differences," *Physical Review Letters* **78**, pp. 2690–2693, 1997.
- [42] I. Laffafian and M. Hallett, "Lipid-assisted microinjection: Introducing material into the cytosol and membranes of small cells," *Biophysical Journal* **75**, pp. 2558–2563, 1998.
- [43] K. Riske, N. Bezlyepkina, R. Lipowsky, and R. Dimova, "Electofusion of model lipid membranes viewed with high temporal resolution," *Biophysical Reviews and Letters* **1**, pp. 387–400, 2006.
- [44] M. Wang, M. Schnitzer, H. Yin, and R. Landick, "Force and velocity measured for single molecules of RNA polymerase," *Science* **282**, pp. 902–907, 1998.
- [45] M. Dogterom and B. Yurke, "Measurement of the force-velocity relation for growing microtubules," *Science* **278**, pp. 856–860, 1997.
- [46] M. Schnitzer and S. Block, "Kinesin hydrolyses one ATP per 8nm step," *Nature* **388**, pp. 386–390, 1997.
- [47] F. Gittes, B. Schnurr, P. Olmsted, F. MacKintosh, and C. Schmidt, "Microscopic viscoelasticity: Shear moduli of soft materials determined from thermal fluctuations," *Physical Review Letters* **79**, pp. 3286–3289, 1997.
- [48] M. Fischer, A. Richardson, S. Reihani, L. Oddershede, and K. Berg-Sørensen, "Validation of FDT calibration method in complex media," in *Optical Trapping and Optical Micromanipulation V*, K. Dholakia and G. C. Spalding, eds., *Proc. SPIE* **7038**, pp. 703822–(1–12), 2008.

- [49] M. Fischer, *Optical tweezers in viscoelastic media*. PhD thesis, Niels Bohr Institute, Copenhagen University, Copenhagen, Denmark., October 2007.
- [50] T. Mason, T. Gisler, K. Kroy, E. Frey, and D. Weitz, “Rheology of F-actin solutions determined from thermally driven tracer motion,” *Journal of Rheology* **44**, pp. 917–928, 2000.
- [51] A. Richardson, M. Fischer, S. Reihani, K. Berg-Sørensen, and L. Oddershede, “How to calibrate optical tweezers in viscoelastic media.” Submitted, 2008.
- [52] A. L. Olsen, “Opløsning af aktinnetværk,” Master’s thesis, Niels Bohr Institute, Copenhagen University, Copenhagen, Denmark., 2006.
- [53] J. Spudich and S. Watt, “The regulation of rabbit skeletal muscle contraction,” *Journal of Biological Chemistry* **246**, pp. 4866–4871, 1971.
- [54] G. Gibson, J. Leach, S. Keen, A. Wright, and M. Padgett, “Measuring the accuracy of particle position and force in optical tweezers using high-speed video microscopy,” *Optics Express* **16**, pp. 14561–14570, 2008.
- [55] R. Brau, J. Ferrer, H. Lee, C. Castro, B. Tam, P. Tarsa, P. Matsudaira, M. Boyce, R. Kamm, and M. Lang, “Passive and active microrheology with optical tweezers,” *Journal of Optics A: Pure and Applied Optics* **9**, pp. S103–S112, 2007.
- [56] A. Palmer, T. Mason, J. Xu, S. Kuo, and D. Wirtz, “Diffusing wave spectroscopy microrheology of actin filament networks,” *Biophysical Journal* **76**, pp. 1063–1071, 1999.
- [57] M. Goksör, J. Enger, and D. Hanstorp, “Optical manipulation in combination with multiphoton microscopy for single-cell studies,” *Applied Optics* **43**, pp. 4831–4837, 2004.
- [58] D. Vossen, A. van der Horst, M. Dogterom, and A. van Blaaderen, “Optical tweezers and confocal microscopy for simultaneous three-dimensional manipulation and imaging in concentrated colloidal dispersions,” *Review of Scientific Instruments* **75**, pp. 2960–2970, 2004.
- [59] A. Hoffmann, G. M. zu Hörste, G. Pilarczyk, S. Monajembashi, V. Uhl, and K. Greulich, “Optical tweezers for confocal microscopy,” *Applied Physics B* **73**, pp. 747–753, 2000.
- [60] M. Friese, H. Rubinsztein-Dunlop, N. Hackenberg, and E. Dearden, “Determination of the force constant of a single beam gradient trap by measurement of backscattered light,” *Applied Optics* **35**, pp. 7112–7116, 1996.

BIBLIOGRAPHY

- [61] C. Gradinaru, P. Martinsson, T. Aartsma, and T. Schmidt, “Simultaneous atomic-force and two-photon fluorescence imaging of biological specimens *in vivo*,” *Ultramicroscopy* **99**, pp. 235–245, 2004.
- [62] A. Richardson, S. Reihani, and L. Oddershede, “Combining confocal microscopy with precise force-scope optical tweezers,” in *Optical Trapping and Optical Micromanipulation III*, K. Dholakia and G. C. Spalding, eds., *Proc. SPIE* **6326**, pp. 632628–(1–10), 2006.
- [63] S. Reihani, M. Charsooghi, H. Khalesifard, and R. Golestanian, “Efficient in-depth trapping with an oil-immersion objective lens,” *Optics Letters* **31**, pp. 766–768, 2006.
- [64] S. Reihani, H. Khalesifard, and R. Golestanian, “Measuring lateral efficiency of optical traps: The effect of tube length,” *Optics Communications* **259**, pp. 204–211, 2006.
- [65] A. Baker, A. Saulière, F. Dumas, C. Millot, S. Mazères, A. Lopez, and L. Salomé, “Functional membrane diffusion of G-protein coupled receptors,” *Euro Biophysics J* **36**, pp. 849–860, 2007.
- [66] M. Dahan, S. Levi, C. Luccardini, P. Rostaing, B. Riveau, and A. Triller, “Diffusion dynamics of glycine receptors revealed by single-quantum dot tracking,” *Science* **302**, pp. 442–445, 2003.
- [67] L. Pan, A. Ishikawa, and N. Tamai, “Detection of optical trapping of CdTe quantum dots by two-photon induced luminescence,” *Physical Review B* **75**, pp. 161305–(1–4), 2007.
- [68] Wikipedia, 2008. <http://en.wikipedia.org/wiki/Quantum-dot>.
- [69] H. Tada, H. Higuchi, T. Wanatabe, and N. Ohuchi, “*In vivo* real-time tracking of single quantum dots conjugated with monoclonal anti-HER2 antibody in tumors of mice,” *Cancer Research* **67**, pp. 1138–1144, 2007.
- [70] M. Nirmal, B. Dabbousi, M. Bawendi, J. Macklin, J. Trautman, T. Harris, and L. Brus, “Fluorescence intermittency in single Cadmium Selenide nanocrystals,” *Nature* **383**, pp. 802–804, 1996.
- [71] S. Hohng and T. Ha, “Near-complete suppression of quantum dot blinking in ambient conditions,” *Journal of the American Chemical Society* **126**, pp. 1324–1325, 2004.
- [72] J. Jaiswal and S. Simon, “Potentials and pitfalls of fluorescent quantum dots for biological imaging,” *Trends in Cell Biology* **14**, pp. 497–504, 2004.

- [73] B. Lagerholm, L. Averett, G. Weinreb, K. Jacobson, and N. Thompson, “Analysis method for measuring submicroscopic distances with blinking quantum dots,” *Biophysical Journal* **91**, pp. 3050–3060, 2006.
- [74] E. A. Christensen, 2007. Private communication.
- [75] K. Berg-Sørensen, L. Oddershede, E.-L. Florin, and H. Flyvbjerg, “Unintended filtering in a typical photodiode detection system for optical tweezers,” *Journal of applied physics* **93**, pp. 3167–3176, 2003.
- [76] P. Hansen, I. Tolic-Nørrelykke, H. Flyvbjerg, and K. Berg-Sørensen, “Tweezercalib 2.0: Faster version of a MatLab package for precision calibration of optical tweezers,” *Computer Physics Communications*. **174**, pp. 518–520, 2006.
- [77] L. Bosanac, T. Aabo, P. Bendix, and L. Oddershede, “Efficient optical trapping and visualization of silver nanoparticles,” *Nano Letters* **8**, pp. 1486–1491, 2008.
- [78] K. Svoboda and S. Block, “Optical trapping of metallic Rayleigh particles,” *Optics Letters* **19**, pp. 930–932, 1994.
- [79] L. Jauffred and L. B. Oddershede, “Two photon excitation optical trapping strength dependence of quantum dot size.” pre publication, 2008.
- [80] D. Segelstein, “The complex refractive index of water,” Master’s thesis, University of Missouri, Kansas city, MO., 1981.
- [81] C. Selhuber-Unkel, I. Zins, O. Schubert, C. Sönnichsen, and L. Oddershede, “Quantitative optical trapping of single gold nanorods,” *Nano Letters* **8**, pp. 2998–3003, 2008.